Resonant core spectroscopies of model molecular solar cells

Andrew James Gibson BSc PGCE QTS MSc

Thesis submitted to The University of Nottingham for the degree of Doctor of Philosophy

Autumn 2016

List of publications

Charge transfer from an adsorbed ruthenium-based photosensitizer through an ultra-thin aluminium oxide layer and into a metallic substrate

A.J. Gibson, R.H. Temperton, K. Handrup, M. Weston, L.C. Mayor, and J.N. O'Shea, J. Chem. Phys. J. Chem. Phys. **140**, 234708 (2014).

Resonant core spectroscopies of the charge transfer interactions between C60 and the surfaces of Au(111), Ag(111), Cu(111) and Pt(111)

A.J. Gibson, R.H. Temperton, K. Handrup, J.N. O'Shea, Surf. Sci. 657, 69-78 (2017).

Growth of and charge transfer through Alumina on Titania

A.J. Gibson, R.H. Temperton, K. Handrup, J.N. O'Shea, (in progress).

Acknowledgements

First and foremost I would like to thank my parents, who helped me enormously throughout my long time at university and in (hopefully) obtaining my third and highest degree, when at one point it looked as if I would not even get one. I would like to acknowledge the past and present members of the Nanoscience Group in Nottingham, who have made the School of Physics and Astronomy such an enjoyable place to work. I would also like to thank the staff at Max-Lab for being so accommodating and helpful, especially thanks to beamline managers Alexei Preobrajenski and Karina Schulte. Huge thanks must go to Robert Temperton and Karston Handrup for the experimental work that they conducted, as well as and most importantly, their continued and much valued friendships. Massive thanks also go to Professor James O'Shea for his invaluable support and friendship as well as for his excellence as my supervisor. Finally to my wife Stephanie, you have been my rock and you are the love of my life and my life continues to get better, all the time, because of you.

"Education is not the answer to the question. Education is the means to the answer to all questions."
William Allin

Contents

List of publications **iii**

Acknowledgements **iv**

1 Introduction **1**
1.1 Global electricity supply 1980-2013 1
1.2 Operating principles of the DSC 5
1.3 Topics researched in this thesis 8

2 Experimental methods and analysis **10**
2.1 Experimental setup 10
2.1.1 Introduction to Synchrotron Radiation 10
2.1.2 Insertion devices 13
2.1.3 The beamline 15
2.1.4 The end station 16
2.1.5 Ultra High Vacuum (UHV) pumps 18
2.1.6 Deposition techniques 20
2.1.7 Hemispherical electron energy analyser 22
2.2 Experimental techniques 24
2.2.1 Photon-electron interaction cross-section 25
2.2.2 X-ray Absorption Spectroscopy (XAS) 27
2.2.3 X-ray Photoemission Spectroscopy (XPS) 30
2.2.4 Spin-orbit coupling 36
2.2.5 Resonant Photoemission Spectroscopy (RPES) 37
2.2.6 Core-hole clock analysis 41
2.2.7 Surface coverage 43

3 N3 on $Al_{10}O_{13}$ **45**
3.1 Introduction 45
3.2 Experiment 48
3.3 Results and Discussion 49
3.3.1 Adsorption bonding 49

3.3.2 Electronic coupling . . . 53
3.3.3 Charge transfer dynamics . . . 56
3.4 Conclusion . . . 61

4 Growth of and charge transfer through alumina on titania. 63
4.1 Introduction . . . 63
4.1.1 Background on ALD growth and conditions . . . 66
4.2 Experiment . . . 67
4.3 Results and Discussion . . . 68
4.3.1 Aluminium oxide growth rate . . . 68
4.3.2 XPS of Aluminium oxide growth . . . 71
4.3.3 Bi-isonicotinic acid on alumina on titania. . . . 75
4.3.4 Charge transfer dynamics and core hole clock . . . 79
4.4 Conclusion . . . 83

5 Charge transfer interaction between C_{60} and metal surfaces 85
5.1 Introduction . . . 86
5.2 Experiment . . . 89
5.3 Results . . . 92
5.3.1 C_{60} multilayer . . . 92
5.3.2 C_{60}/Au(111) monolayer . . . 93
5.3.3 C_{60}/Ag(111) monolayer . . . 98
5.3.4 C_{60}/Cu(111) monolayer . . . 101
5.3.5 C_{60}/Pt(111) monolayer . . . 103
5.4 Discussion . . . 103
5.5 Conclusion . . . 111

6 Summary and Conclusions 113

List of Figures 116

Bibliography 125

Chapter 1

Introduction

This section contains: An overview of global electricity production 1980-2013 to show the justification for further investment in renewable technology especially solar. The graphs in this section were produced from data publicly available from the U.S. Energy Information Administration.[1] Later in this section I present an introduction to and overview of dye sensitised solar cells and a summary of the subsequent chapters in this thesis.

1.1 Global electricity supply 1980-2013

Since the year before my birth 1980 and 2013 the worlds total net electricity generation has increased by 175% to 22 trillion kWh per year even outpacing population growth, Fig.1.1. CO_2 emissions have also increased by 75% from 18.4 to 32.2 Billion metric tons per year.[1] Clearly for the long term benefit of mankind we must be able to utilise our resources to supply our ever increasing demand for electricity.

Since fossil fuels are causing devastating climate change, these finite resources cannot be part of any long term energy solution. Renewables are the only viable option, but sustainable sources have a long way to go to catch up with fossil fuels. The amount of energy from fossil fuels has increased by 180%, Fig.1.2 and they currently produce more than triple the amount of energy that renewable sources provide. The relative growth in fossil fuels is also outpacing renewables, largely due to increased coal use in China.

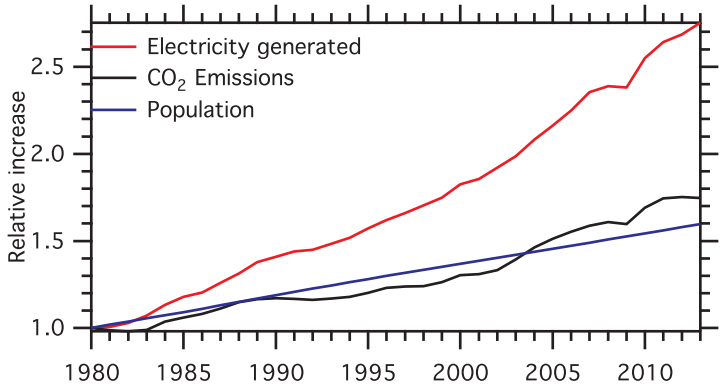

Figure 1.1: Relative increase in global net electricity generation, CO_2 emissions and population from 1980 to 2013.[1, 2]

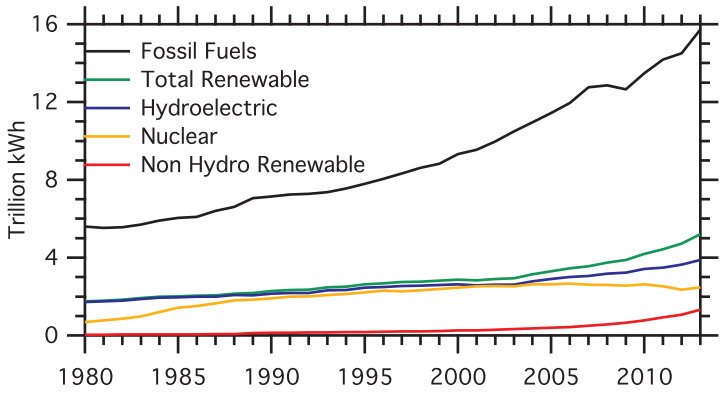

Figure 1.2: Break down of world electricity production by fuel type from 1980-2013.[1, 2]

Within renewable energy sources hydroelectric power produces far more energy than all other renewable sources combined. However, due to the limited number of locations available to hydroelectric power it probably cannot be upscaled at a high enough rate to supply our increasing demand. Biomass and waste have also been making steady progress for the last thirty years and in 2013 it made up 10.2% of Global fuel usage.[2] Wind has been making significant increases, especially in this millennium, while there is some vocal opposition to wind turbines because of their appearance it seems the majority of the public are in favour of them.[3] Solar is producing relatively little electricity, only 0.45% of all electricity produced worldwide in 2012.[1] One of the

main reasons for the shortfall in solar power is the high cost of the materials. However, in recent years costs have been reducing and solar generation has approximately tripled every two years,[1] and is currently the fastest growing renewable technology.[4].

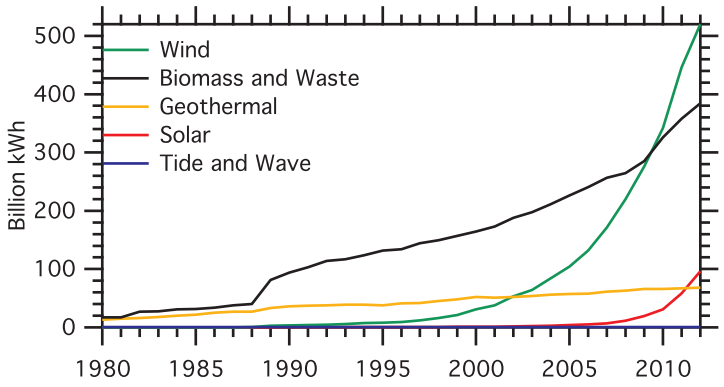

Figure 1.3: Breakdown of global non-hydroelectric renewable energy production from 1980-2012.[1, 2]

In 2012 the world consumed 5.24×10^{20}J of energy.[5] We can calculate how long it would take to receive this energy from the sun, since the solar constant is $1.4\,\mathrm{kWm}^{-2}$[6] and incoming solar radiation on the earth's surface is 25% of this value, hence the earth's yearly requirement for energy is received from the sun in approximately 50 mins. So the potential for solar energy to provide a significant proportion of the worlds energy supply is obvious. Photovoltaic energy also does not require any large scale equipment or infrastructure to maintain, so it is accessible to the general public as well as the under-developed regions of the globe. However, one key issue remains that photovoltaic devices must become economically viable through increased efficiencies and cheaper fabrication before they can become more widespread.

Most commercial solar cells use polycrystalline silicon as the core material. This material is expensive[7] but incorporating it into commercial solar cells provides reasonable efficiencies of around 18%, enough to make it economically viable, with a thin margin. The majority of costs associated with the silicon solar cell come from the purification of the raw silicon and machining steps which require very high temperatures over extended periods of time. The high

demand for polycrystalline silicon cells reduces costs to some degree through bulk production. However, we may not see significant improvements in efficiency or cost that can keep up with the ever increasing demand, so a diverse range of solar technologies and research is essential. In order for photovoltaic industry to make improvements various avenues of research must be explored.

Instead of using semi-conductors to absorb photons a dye sensitised solar cell (DSC) uses mostly organometallic, light-absorbing dye molecules. DSCs offer alternative materials and, since they do not use high temperatures or vacuum processes, they offer a cheaper manufacturing process. DSCs are tuneable aesthetically through the colour of the dye and electrolyte, this allows the installation of coloured building facades made of solar arrays such as Fig.1.4. They can also be engineered into flexible sheets making them easier to transport and install, but could also give an opportunity for wearable photovoltaic devices. While DSCs are currently less efficient than other thin film devices[8] the lower cost gives much shorter energy payback times and low environmental impact,[9] which makes them a very competitive alternative in some situations.

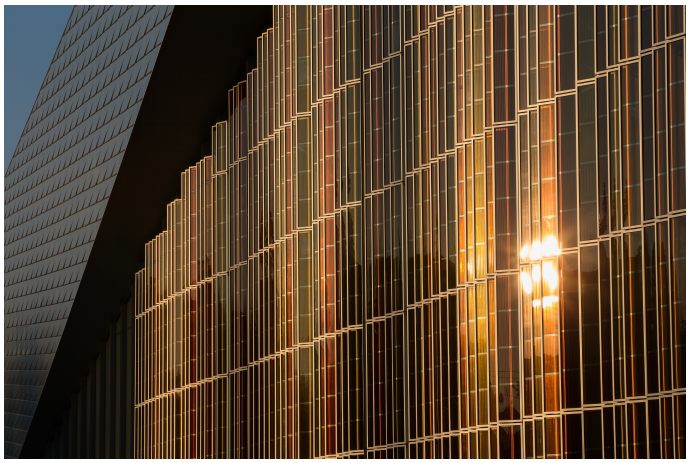

Figure 1.4: The coloured transparent dye sensitized solar cells on the west face of the SwissTech Convention Center, opened in 2014 (image labeled for reuse).

The initial DSC breakthrough led to efficiencies of between 7-8% in 1991,[10] which is far below the standard efficiency of commercial silicon based cells around 14-20%.[11] A significant step forward for DSCs was the synthesis of the dye molecule N3, (cis-bis(isothiocyanato)bis(2,2-bipyridyl-4,4'-

dicarboxylato)-ruthenium(II), see Fig.1.5 which had a photovoltaic performance that was unmatched for 8 years and as such has become the bench mark for heterogeneous charge transfer in DSCs. When guanidium thiocyanate is added to the electrolyte, a large reduction in dark current was achieved which improved the cell voltage, this was due to guandium cations controlling the self assembly of N3 at the TiO_2 surface, as such this cell produced new record efficiencies of 11%[12]. If rapid charge injection can take place out of the molecule then chemical transformations cannot occur, leading to a highly stable soar cell arrangement which can operate for approximately 20 years without noticeable loss in performance[12]. Hence N3 is viable for use in highly efficient and long lasting DSCs. Only in 2011 was N3 clearly surpassed by zinc porphyrin dye, which achieved 12.3% [13] and in 2014 13% power conversion efficiency was achieved by another porphyrin based dye.[14] However, for the zinc porphyrin after only 220 hours of full sunlight at 30 °C there was a 10 to 15% decrease in the overall efficiency.[13] While SM325 has shown stability only over 500 hours, it had an initial decrease of 10-20% in efficiency, so it remains to be seen how durable these porphyrin dyes are in the long term. The increase in lab efficiency of a DSC is now close to the efficiency of commercially available silicon solar cells but with the DSC at considerably lower cost.

1.2 Operating principles of the DSC

The basic principle behind any solar cell is to inject a photo-excited electron into a circuit to do work. The typical DSC layout is shown in Fig.1.5 the red circles in the centre depict a mesoporous, semiconducting, oxide layer composed of TiO_2 nanoparticles. TiO_2 is used since it is relatively cheap and has a large band gap. The nanoparticles are then sintered together to create a conductive pathway with large surface area, which is then deposited onto the conducting transparent support, usually plastic or glass substrate to form the anode of the cell. Adsorbed onto the TiO_2 is a monolayer of sensitising dye, shown as N3 in the large red circle at the top of the diagram. The dye must have a molecular orbital band-gap designed to absorb specific frequencies of light from the solar spectrum and form a chemical bond to the TiO_2 to improve

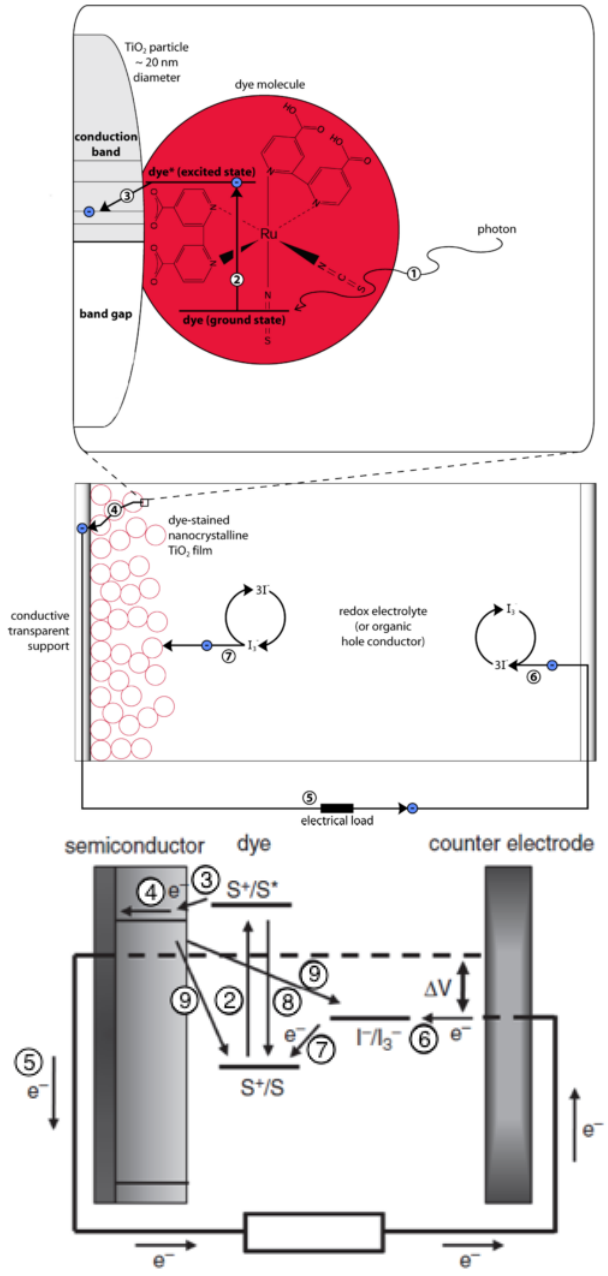

Figure 1.5: The typical DSC layout is shown in centre, the enlargement at the top shows the active region with the dye molecule, while below show a schematic for the energy transfers involved, incoming light (1), followed by electron excitation (2), transfer to substrate (3), to conductive glass (4), work in the circuit (5), recombination with electrolyte (6), from electrolyte to dye (7), exciton recombination (8) and recombination between the semiconductor and the dye cation (9).

durability.

As well as achieving a high induced photon to current efficiency, the dye must produce a reasonable voltage. Theoretically the maximum voltage ΔV is the difference between the Fermi level of the mesoporous TiO_2 and the redox potential of the electrolyte, a pseudo voltage level diagram of the cell is shown in the lower third of Fig.1.5. When optimising the design of a DSC for large potential difference and therefore maximum work, the energy levels of each component should be tuned so that the forward reaction of the cell is favourable.

The charge transfer processes in a DSC numbered in Fig.1.5 are described as follows: Visible light passes through the transparent conductive glass (1) and is absorbed by the dye chemisorbed to a thin film of TiO_2. This promotes an electron from the ground state to the excited state (2). If the excited state of the electron overlaps with the conduction band on the semiconductor it can transfer into the TiO_2 substrate (3), leaving positive charge on the surface-adsorbed dye molecule. Once the electron has been transferred to the semiconductor it diffuses through the TiO_2 particles until it reaches the surface of the conductive transparent glass (4). The potential difference between here and the counter electrode and the electric charge extracted from the photo anode as a current can be utilised to do work (5).

Finally in order to close the circuit, efficient charge collection requires charge recombination between injected electrons at the counter electrode and the oxidised dye molecule (7), which is achieved via a liquid electrolyte (6), typically $I_3^-/3I^-$. The electrolyte is reduced via equation.1.1. Since the I_3^- and $3I^-$ anions are mobile in the electrolyte the diffusion from the counter electrode to the dye allows the dye cation D^+ to be reduced via Equation.1.2.

$$I_3^- + 2e^- \rightarrow 3I^- \tag{1.1}$$

$$2D^+ + 3I^- \rightarrow 2S + I_3^- \tag{1.2}$$

All these process (2-7) are favourable, However, there are several competing recombination processes that are unfavourable. After the initial excitation (2) if the electron does not tunnel away (3) in sufficient time the exciton can

recombine via process (8). Efficient electron transfer to the dye cation requires the redox electrolyte re-reduction by the dye cation (7) to be faster than recombination between injected electrons and photo-generated dye cations (8). The charge transfer time from the dye into the substate is one of the key elements that this thesis will focus on. Even after the excited electron tunnels into the semiconductor it can still recombine with either the dye cation or the electrolyte, process (9). Adding a thin aluminium oxide coating to the TiO_2 nano particles can help reduce these recombination effects. Since these process bypass doing work in the external circuit they reduce the efficiency of the cell. Hence further understanding charge transfer processes between a dye molecule and TiO_2 (process 2) with an oxide recombination barrier could lead to more efficient DSCs.

An alternative thin film organic solar cell architecture use a bulk heterojunction, which consists of separate electron donor and acceptor. Donors are usually conjugated pigments, oligomers or polymers such as P3HT (poly-3-hexyl thiophene-2,5-diyl), while the most common acceptors are organic fullerene based molecules such as PCBM (Phenyl-C61-butyric acid methyl ester).[9, 15] Several models predict power conversion efficiencies of 10-15% for these devices.[9] C_{60} was introduced into a DSC between porphyrin molecules and TiO_2, which resulted in improved energy conversion and a higher photocurrent per molecule.[16] Hence C_{60} is interesting as a potential building block in future solar cell devices.

1.3 Topics researched in this thesis

This work is intended to give insights into the fundamental architecture and charge processes in a DSC by creating experimental models of parts of the device. The following chapter will give an overview of synchrotron radiation and how it is used in our experiments, as well as the key apparatus, methods and analysis that form the foundation of the thesis.

The first experimental chapter investigates the charge transfer from N3 through an ultra thin aluminium oxide layer and into the underlying metallic substrate. The second experimental chapter takes this model closer to a real

DSC by a growing thin alumina layer on TiO_2 and investigating the charge transfer from the N3 ligand bi-isonicotinic acid through different thicknesses of alumina and into the titania substrate.

Previous work in our research group[17] on the dye ligand bi-isonicotinic acid revealed a new feature which was described as *superspectator* decay, which was thought to occur as a result of charge transfer to the molecule in the ground state. A set of three features were seen for a monolayer of C_{60} on Au(111).[18] In order to further understand this charge transfer mechanism and its possible links to DSC electron transfer the final experimental chapter of this thesis presents the study of C_{60} on four further metallic surfaces. Finally there is a summary and conclusion to the thesis.

Chapter 2

Experimental methods and analysis

An overview of the key features of a synchrotron and principal experimental components. A summary of the interactions between X-rays and matter and the main X-ray techniques used in this work: X-ray photoelectron spectroscopy (XPS) and X-ray absorption spectroscopy (XAS) and Resonant Photoemission spectroscopy (RPES) and the analysis used for these techniques including the core-hole-clock.

2.1 Experimental setup

2.1.1 Introduction to Synchrotron Radiation

One key to understanding electronic and chemical properties of a DSCs is to look carefully at the interaction between the dye and the surface and how the system responds to light. By exciting the system with photons we can measure the effect on the electrons, we can measure the decay process of the excited species and probe the chemistry of the system. But to do this effectively we need an intense source of photons, which we can tune to specific frequencies, hence the need for a synchrotron such as the MAX II ring at MAX-Lab in Lund, Sweden which was used for all the experiments in this thesis.

A synchrotron such as MAX II is made of various parts which accelerate

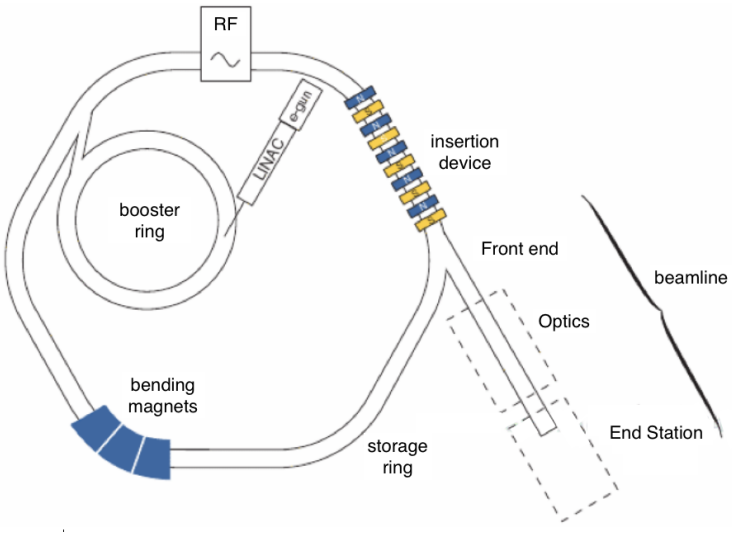

Figure 2.1: Schematic of the most important parts of a modern synchrotron, diagram edited from.[19]

electrons up to relativistic speed, with a kinetic energy of 1.5 GeV and then quickly change their direction to generate photons with a range of energies. Fig.2.1 shows the basic schematic of a synchrotron which consists of: a source of electrons, normally from thermionic emission from a hot filament e-gun as on the diagram; a linear accelerator (LINAC) which accelerates the electrons to approximately 100 MeV; and a booster ring that provides further acceleration before the electrons are periodically injected into the storage ring at relativistic velocity. In the storage ring, electrons are kept in a closed path due to an array of magnets; dipole or bending magnets change the electrons path, quadrupole magnets focus the electron beam and compensate for Coulomb repulsion between electrons and sextuples correct for chromatic aberrations which arise due the quadrupole focusing.[19] The bending magnets and insertion devices then accelerate the relativistic electrons to produce photons and send them into a beamline. Optics are then used to filter the radiation to a specified frequency and direct it to the end station for the experiment.

Since the electrons are losing energy to generate photons this would cause them to spiral into the walls of the synchrotron if that energy is not replaced. This replacement is achieved by a radio frequency (RF) cavities. Despite the storage ring being at UHV pressure there are always electrons being lost in

the machine due to collisions with residual gas. This leads the ring current to decrease exponentially over time, so a regular replacement of electrons is required. At MAX II the electron beam is deliberately dumped or crashed in the storage ring and a new set of electrons injected as previously described. This means the beam current and therefore photon flux is a variable during the experiment, to compensate for this measurements are typically normalised to the beam current in the storage ring.

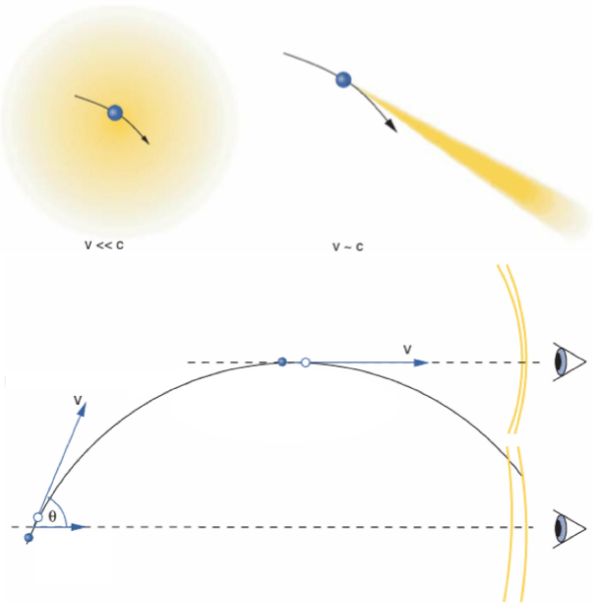

Figure 2.2: Above indicates how radiation propagates radially from an electron travelling at non relativistic velocities, compared to the highly intense, tangentially propagated narrow beam of radiation which is emitted from an electrons travelling at relativistic velocities. Below for the perspective of an observer an electron travelling towards them emits highly blue shifted radiation, while the off axis observer see a far less pronounced doppler shift, diagram edited from.[19].

If an electron is travelling at low speed then it emits radiation isotropically Fig.2.2(above), however once electrons reach relativistic velocities as in the synchrotron they emit highly intense radiation along the tangent to their path. An observer looking at an electron that is turning into their line of sight will observe a very large doppler shift to the radiation and hence hugely compressed wavelength of light due to the relativistic speed, hence X-ray photons

are emitted. Since the relativistic compression of the waves falls off quickly the observer sees far more intense radiation here when compared to other points on the orbit. A bending magnet is used to provide a Lorentz force which acts on the particle in a direction perpendicular to both the magnetic and velocity of the electron. Thus the magnet causes the electron to undergo centripetal acceleration and thus generates X-rays. If the ring current is increased and therefore greater number of electrons per second then this increase the number of photons emitted. This system led to first generation beam lines that piggybacked on accelerator experiments. Later second generation sources still used bending magnets but rather than parasitic experiments these accelerators were specifically designed to produce synchrotron radiation.

Third generation sources such as MAX II use insertion devices to generate the most intense/highest brilliance of radiation. Brilliance of radiation essentially states how the flux is distributed in space and angular range, therefore it determines the smallest possible spot which the X-ray beam can be focused onto, it is measured as:

$$Brilliance = \frac{photons/second}{(mrad)^2(mm^2 sourcearea)(0.1\%bandwidth)} \tag{2.1}$$

Brilliance is therefore the flux per unit source area and unit solid angle, the high the brilliance in general the higher the quality of data than can be extracted from the beamline.

2.1.2 Insertion devices

Insertion devices are placed in the straight sections between bending magnets, through the use of multiple magnets they force electrons to execute an oscillatory path. An example of an undulator can be seen in Fig.2.3, this device is approximately 3 m in length and the multiple magnets would be aligned above and below the electron beam. During operation the distance between the magnets is typically reduced to between 17 and 35 mm depending on the mode of operation. Since the electrons are being accelerated multiple times this leads to higher intensity and brilliance of radiation being produced.

There are two types of insertion device and they are separated by the de-

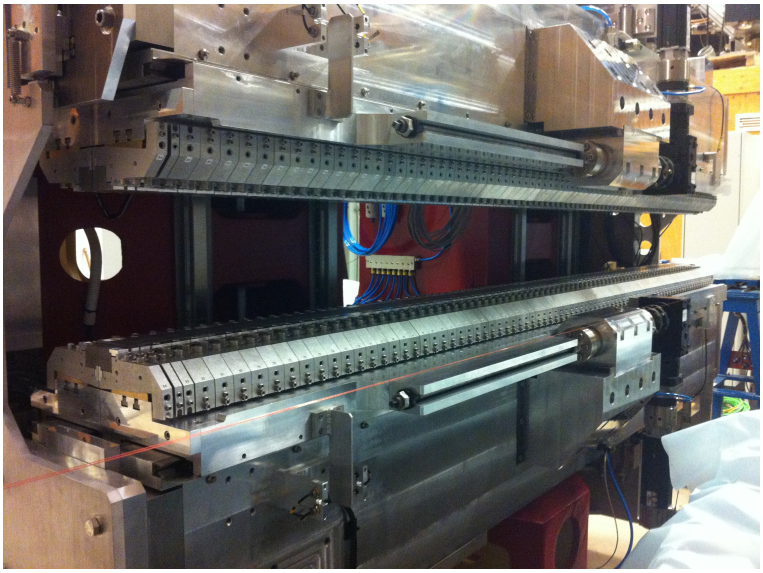

Figure 2.3: An undulator seen prior to its installation at the MAX-IV laboratory.

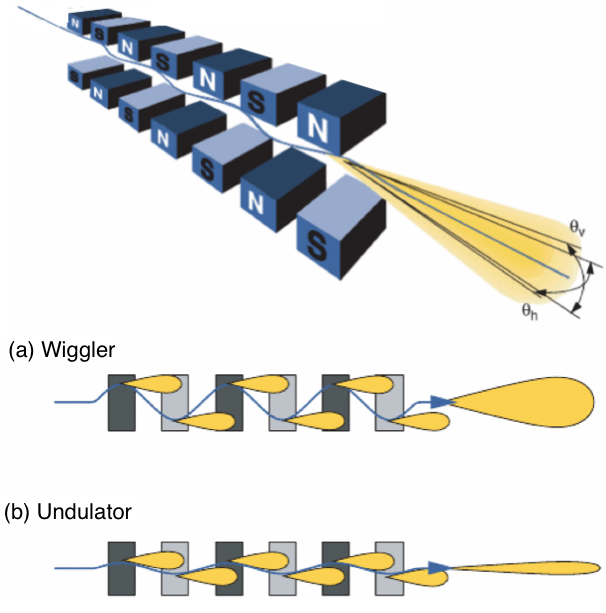

Figure 2.4: Schematic of and undulator/wiggler(above), how the radiation cones from each wiggle do not overlap and therefore intensity is added in a wiggler, while for an undulator has gentler excursion and the radiation cones do overlap, diagram edited from.[19]

gree to which they make the beam bend as it passes through. For openings larger than λ^{-1} the radiation cones from each wiggle do not overlap, every electron in the bunch radiates independently, hence and the intensities are added, the resultant radiation is a broad bandwidth, the resulting intensity of the radiation in a wiggler is proportional to the number of magnetic poles. Gentler excursion less than λ^{-1} occur in an undulator, for example for photons at 340 eV the excursion is 3.7 nm. Here the radiation cones overlap and interfere constructively with each other, producing a narrower bandwidth, but higher intensity of radiation. The intensity of radiation in an undulator scales as the square of the number of poles in the magnetic array, since the field amplitudes including phase differences are added.

Only certain wavelengths interfere constructively therefore the undulator spectrum contains a fundamental frequency and a series of higher harmonics. Hence the user can adjust the gap between the magnets to vary the frequency of the most intense radiation or generate the highest brilliance radiation at a required frequency. A taper reduces the intensity variation of the radiation as the photon energy was scanned, which is useful for absorption measurements such as Resonant photoemission spectroscopy (RPES) or X-ray absorption spectroscopy (XAS), where you want a smooth background as a function of photon energy.[20]

2.1.3 The beamline

A synchrotron with insertion devices can provide radiation from the far infrared to the hard X-ray regime. For experiments it is necessary to narrow the region of photon energies down to a small bandwidth and to focus these photons on a sample surface. Beam lines, such as I311 at MAX II in Fig.2.5, run linearly from an insertion device, the other beamline D1011 at MAX II used in this thesis is at a tangent to a bending magnets. The front end of the beamline isolates the beam vacuum from the storage ring vacuum and measures the position of the photon beam. In order to collimate the beam from the real source at S (Fig.2.5) and absorb the lower energy photons that are away from the central axis of the beam an aperture is used. These outer parts of the

beam are more strongly absorbed by matter hence the aperture also suppresses the number of lower energy photons which are incident on other parts of the beam line, therefore extending the lifetime of the beamline. The beam is then focused onto the sample using a series of curved mirrors. M1 is a horizontally focusing pre-mirror, M2 a rotatable plane mirror which directs light to G, an in plane grating, which in turn passes photons to M3, a spherical focusing mirror. In this set up M2, G and M3 comprises the monochromator which uses a moveable diffraction grating and exit slit so that specific wavelengths of light can be selected from the diffraction pattern. The I311 beam line enables photons in the energy range from 30-1500 eV with a resolution of 4 meV-1.4 eV respectively. Another aperture is used to clean up the beam, before it is finally incident on the sample in the end station.

2.1.4 The end station

The end station comprises two UHV chambers; one preparation and one analysis chamber (see Fig.2.6). A manipulator allows controlled movement of the sample between chambers, and in x, y, z and θ to allow sample positioning in front of the light in the analysis chamber and the molecule sources in the prep chamber. The prep chamber can be isolated from the analysis chamber to allow high pressure preparation techniques. It is also fitted with a sputter gun, which accelerates Ar^+ ions at the sample, removing a few atomic layers from the surface to expose the clean underlying surface. The manipulator also allows electrical contact to be made with metal samples to allow direct heating by passing a current through the sample. For non-conducting samples an e-beam heater is used, this supplies energy to the sample by applying a negative bias to a filament, grounding the sample, thus imparting electrons onto the back of the sample across a potential of several hundred volts. These heating mechanisms both desorb molecules and allow the sample to find a lower energy state, repairing any faults caused by the sputtering process. Dosing of gases, evaporation and electrospray deposition[21–23] of molecules is also all conducted in the preparation chamber, to modify the surface grow oxide layers and deposit dye molecule or other molecules related to DSCs in order

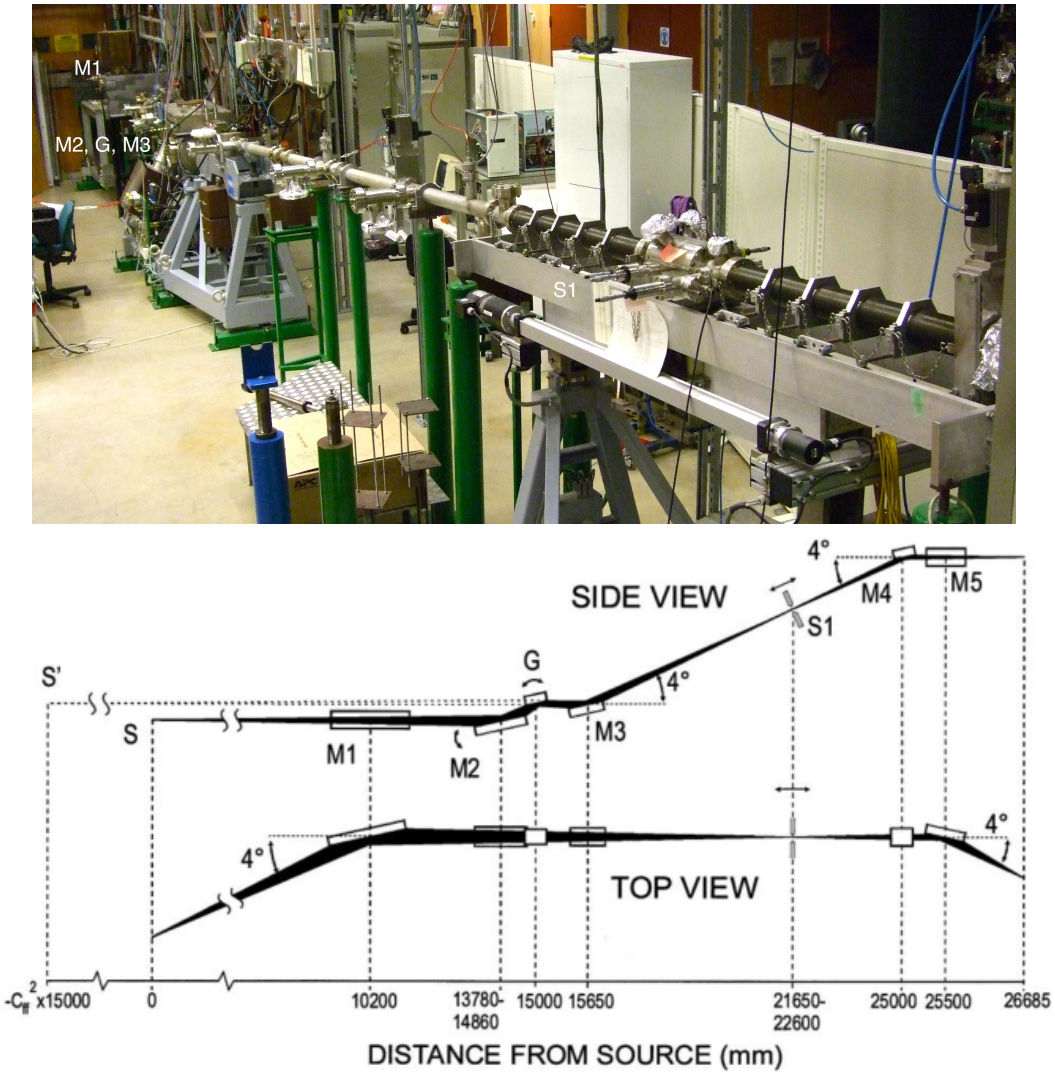

Figure 2.5: Above, photograph of the I311 beam line, end station is omitted. Below schematic for the same beam line at max-lab, focusing pre-mirror (M1), rotatable plane mirror (M2), an in plane grating (G), a spherical focusing mirror (M3), aperture or slit (S1) beofre mirror that focus onto sample (M4 &5).

to create model DSC surfaces. The analysis chamber is kept separate from the prep chamber to reduce contamination during sample preparation. After preparation, the sample is lowered into the analysis chamber and into the path of the X-rays.

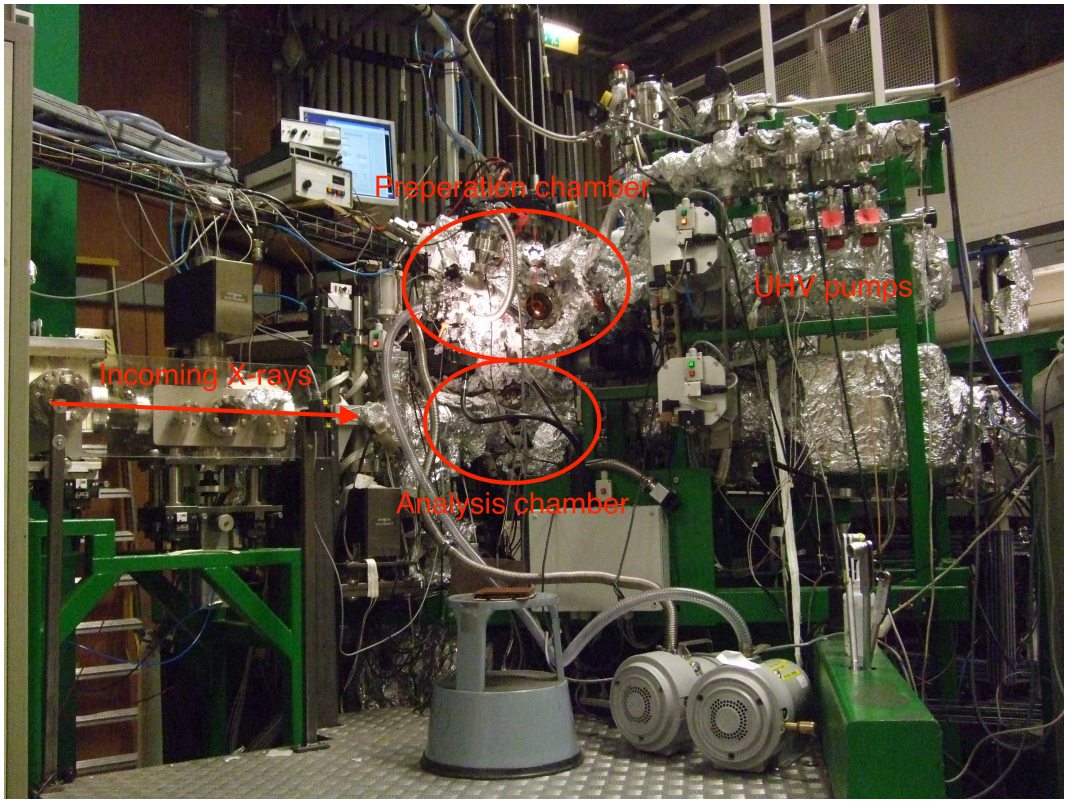

Figure 2.6: Photograph of the I311 end station, large area in the centre covered in foil is the prep chamber on top and analysis chamber below. The beam line can be seen entering from the left, which directs the beam into the analysis chamber. The righthand side shows the UHV pumps and gas line.

2.1.5 Ultra High Vacuum (UHV) pumps

It is also important that we operate our experiments in an ultra high vacuum(UHV) environment in order to keep the surface sufficiently clean such that we only measure desired properties without interference from contaminants and remove excess particles in the system after deposition. In many cases sample transfer into vacuum was not possible and the system had to be

vented so the sample could be mounted to the manipulator, hence to restore UHV the system must be pumped and baked. The system is initially baked to 450K to thermally evaporate molecules such as water from the chamber surfaces. This was achieved by wrapping heating tapes around the chamber and insulating it with foil. The pressure is then reduced during the bakeout and maintained in UHV after the bake by a series of vacuum pumps.

To reduce the system pressure from atmospheric pressure down to a suitable pressure where more advanced pumping methods may be used a rotary or sorption pumps are required to bring the pressure from atmospheric pressure (1000 mbar) down to 10^{-2} - 10^{-3} mbar. A rotatory pump increases a volume on the vacuum side, it then closes off this volume from the vacuum and compresses it through an exhaust to atmosphere, thus removing high volumes of gas but are not sophisticated enough to achieve lower pressures. These pumps are see on the floor in Fig.2.6.

A turbo molecular pumps can be used to further reduce the pressure to the $10^{-6} - 10^{-9}$ mbar range, they use spinning blades which are angled to the degree of rotation such that molecules are more likely to travel from UHV rather than towards it. Molecules travel through a series of these blades and will preferentially hit the lower side of the rotary blade and be pushed out of the system. Stator blades are places after each rotor blade to ensure that only molecules traveling in the correct direction reach the next stage and subsequently onto the backing pump.

An ion pump will further reduce the pressure to the $10^{-9} - 10^{-11}$mbar range. They use a high magnetic field to give charged particles a long helical path through the pump. A high voltage causes ions to form and these ions are accelerated toward a Ti cathode. At the cathode they can be chemically absorbed or captured. At high energies they can also cause the sputtering of material from the cathode, the sputtered material can also trap gas particles.

To measure the vacuum pressure an Ion gauge is used, electrons are emitted from a heated cathode and are attracted to a heating element anode with DC potential around 150 V. The majority of electrons pass through the grid and a few collide with the residual gas forming gas ions. The gas ions are accelerated towards the central ion collector wire by the negative voltage on the collector

typically −30 V. The ion current is amplified and measured to give the pressure reading.

With UHV achieved and measured, X-ray radiation from the synchrotron is now directed into the analysis chamber we are able to put our sample in front of the beam for experimentation.

2.1.6 Deposition techniques

Thermal evaporation is a method of depositing volatile substances on to a prepared substrate. The molecule of interest is deposited via the crucible of a Knudsen cell (also known as a K-cell). The K-cell uses a crucible which is placed within the UHV chamber, and connected via electrodes to allow direct heating through electrical current. The crucible is made from an metal, such as tantalum, which has a very high melting temperature. The powder of molecule to be deposited is placed into a clean crucible of the K-cell prior to its fitting to the vacuum chamber. Once under vacuum, with a direct path from K-cell to the surface is available to the sublimed molecules as such the molecule can be deposited onto the surface by heating the crucible to the molecules sublimation temperature. Those and baked at a temperature below the sublimation point of the molecule, such that impurities like water can be removed. During deposition the crucible is again heated by an electric current, but this time to just above the sublimation point of the molecule. A channel is made available so that the molecule can travel from the crucible to the substrate. The amount of time the channel is open and the temperature of the K-cell will determine the amount of chemical deposited onto the surface. The surface can also be held above the sublimation temperature, therefore only molecules that become chemically bound to the surface will remain since any unbound molecule will sublime. Thus allowing the formation of monolayers on the surface. High temperatures within the crucible can cause some molecule to decompose before they sublime therefore requiring a different technique.

Electrospray is a method of depositing thermally fragile or non-volatile substances into a UHV environment, thus allowing the study of a broader range of molecules. With the molecule of interest is in a liquid state an electric field is

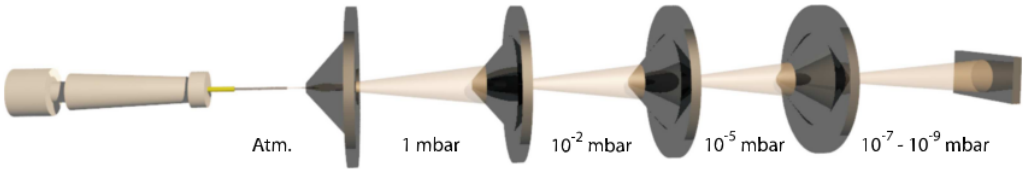

Figure 2.7: Schematic of electrospray deposition system, showing the thin capillary emitting molecular beam in atmosphere and travelling left to right, subsequent apertures through differentially pumped chambers of increasingly high vacuum before final incidence onto sample in UHV.[22]

used to ionise droplets of the solution. If a small capillary and a high positive bias (+1-5kV) is used the ionised droplets will repel each other creating a Taylor cone and plume of microscopic droplets, in ambient pressure.

The current generation of electrospray systems, partly developed in Nottingham, enables the transfer of some molecules in the plume through apertures into subsequent differential pumping chambers of increasingly high vacuum before transfer into UHV, see Fig.2.7. An entrance capillary of diameter 0.25mm is placed in front of the electrospray plume, this allows for a high flux of molecules while minimising the pressure increase at the deposition location. The first two chambers are pumped by a scroll pump, while the third is pumped with a turbo. Through each stage the solvent will further evaporate and be pumped away allowing the reduction in pressure. A gate value is then placed between the third chamber of the electrospray and the preparation chamber to allow it to be completely sealed from atmosphere. The substrate it typically placed 10-20 cm from the gate value. The electrospray deposition spot is approximately 3mm in diameter and of variable thickness, with highest coverage in the centre. It is therefore possible to deposit both monolayer and multilayer coverages in one deposition step.

Atomic layer deposition (ALD) is a thin film deposition technique which uses sequential self terminating surface reactions, see Fig.2.8. In stage 1, precursor A is initially exposed to the substrate bonding to it. The precursor consists of two parts, shown in blue and green, that are indented to remain on the surface and be removed in the byproduct respectively. The second precursor B is then exposed to the surface in stage 2, it reacts with precursor A,

removing the some of the green and grey byproduct and leaving the purple and blue structure of the thin film, labelled 2. The process can then be repeated, ABABAB, until the desired thickness of film is achieved. Steric hinderance caused by the green part of precursors A will prevent the surface from being saturated in one step, it may therefore take multiple steps to fully passivate the surface. Inevitably not all reactions will go to completion and some of the intended by product will remain in the film as impurities, (labeled 3).

2.1.7 Hemispherical electron energy analyser

Once the X-ray beam is focused on the sample electrons are produced via the photoelectric effect and Auger relaxation at a range of energies. To enable experimental analysis of these electrons a hemispherical analyser is used. Electrons pass through a retardation mesh or optics which alter their kinetic energy by a fixed offset allowing different energies to pass through the analyser, an entrance slit is used to prevent unusual trajectories. Electrons are then accelerated around a curve in the analyser using an electric field, only electrons near to the pass energy are curved by the required amount for them to be incident on the detector, allowing precise measurement of the number of electrons and their kinetic energy. Due to the width of the detector a range of electron energies will be incident upon it, red and blue lines representing the lower and higher kinetic energies respectively. A real detector would have a narrower detector and exit slit than pictured in the diagram, therefore allowing a smaller range of electron energies/paths.

There are two modes of detection: swept and fixed. Swept mode alters the retardation level of the incident electrons, while keeping the pass energy through the hemisphere the same, hence different initial energy electrons are now incident on the detector. The number of electrons at different energy levels are measured by progressively altering the retardation of the incident electrons. A full spectrum of electron kinetic energies can be measured at one fixed pass energy level on the detector, this tends to be the method used for XPS. If a narrow band is to be measured, fixed mode keeps the retardation level the same and measures the incident position on the detector to record

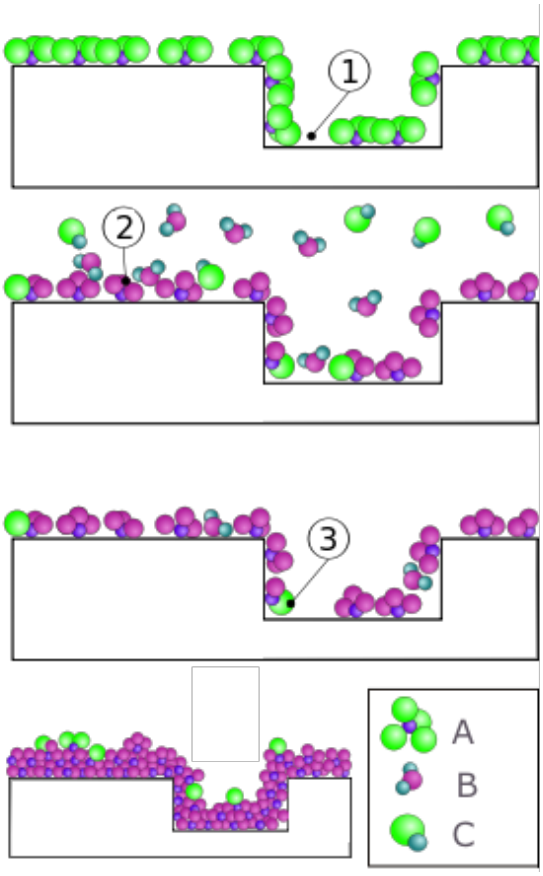

Figure 2.8: Schematic of the ALD process, showing the subsequent deposition of precursors A and B, with by product C to create a thin film on the substrate. The surface does not become fully passivated in stage 1, in stage two the precursor B is applied and the structure of the film is seen at 2, 3 indicates impurities that remain. Below indicates structure of the film after multiple sequential exposures of precursors A and B.

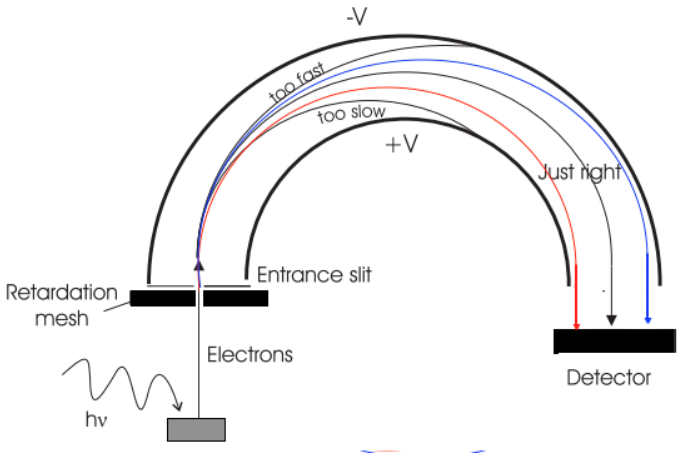

Figure 2.9: Schematic diagram of a hemispherical electron analyser.

the kinetic energy of the electrons for a small range of energies. When this technique is combined with a variable photon energy it allows the formation of RPES data, and when measuring across the kinetic energy of an Auger emission process, XAS data. The techniques of XPS, XAS and RPES are discussed in further detail in the following section.

2.2 Experimental techniques

The interaction between light and electrons was first observed in 1887 by H. Hertz,[24] when he realised that zinc lost negative charge when irradiated. The discovery lead in part to the quantum revolution since the explanation of this phenomena required that light act like a particle, or photon, instead of the previously well established wave model. The photoelectric effect has lead to photoelectron spectroscopy, which is immensely useful for studying the chemical structure and the electronic dynamics of absorbed molecules on surfaces. The synchrotron radiation used in this thesis is in the soft X-ray region, it is therefore important that we understand this interaction between these X-rays and electrons in the sample.

Soft X-rays can be absorbed and elastically or inelastically scattered by materials. For applications using synchrotron radiation, the only significant interactions between X-rays and electrons are elastic Thomson scattering, in-

elastic Compton scattering and photoelectric absorption. This is due to the interaction cross-section being relatively high for these processes at the photon energy of soft X-rays, while the interaction cross section of other processes is negligible. Thomson scattering can be explained classically. The X-ray is scattered when an electron is sinusoidally accelerated by an electromagnetic field of a photon, the electron then reradiates at the same wavelength hence an elastic process. Compton scattering involves only part of a photon's energy being transferred to an electron and hence a lower energy photon is scattered. During photoelectric absorption the photon transfers all its energy to the electron and raises it to a higher energy level. If the photon is in the X-ray region the process can be described as X-ray adsorption.

2.2.1 Photon-electron interaction cross-section

To describe the complex interaction between an electromagnet wave and electron during X-ray absorption a semi-classical model can be used. The molecule is treated with a quantum process, while the radiation uses the classical electrodynamics described by Maxwell's equations. This model is sufficient to provide theoretical insight but it neglects how a field alters due to the interaction. The probability of an electronic transition per unit time P_{i-f}, between an initial state, $|i\rangle$, and a final state, $|f\rangle$, driven by a harmonic time dependant perturbation $V(t) = \bar{V}e^{-i\omega t}$ is determined using Fermi's golden rule:[25, 26]

$$P_{i\to f} = \frac{2\pi}{\hbar}\left(\left\langle f\left|\bar{V}\right|i\right\rangle\right)^2 \rho\left(\varepsilon\right) \tag{2.2}$$

The variable $\rho\left(\varepsilon\right)$ represents the density of states for the final state for the defined energy range, the number of states that fall in the range $\epsilon \to \epsilon + \delta\epsilon$. The initial and final states include all the electrons in the molecule or atom as all the electrons are affected by the perturbation caused by the photon. The final state $|f\rangle$ of the excited electron is assumed to be a free electron in the presence of an ion. A correction will have to be made if the excited state is bound to an atom or in the presence of a neutral species.

The dominant term in the perturbation describes the interaction between a spin-less particle and electromagnetic field is given by:[25]

$$V(t) = \frac{e}{mc}\mathbf{A}.\mathbf{p} \tag{2.3}$$

Where e and m are the electronic charge and mass respectively, c the speed of light and $\mathbf{p}$ is the operator for linear momentum. For groups of electrons $\mathbf{p}$ becomes the sum of the individual operators. To calculate the total X-ray absorption cross section we must sum over all bound states that have an energy less than the photon energy. When the photon energy is able to excite core electrons the interaction cross section with valence or outer shell electrons have a smooth cross section,[25] hence the underlying cross section from these states can be omitted. Considering the interaction of the electromagnetic plane wave with a vector potential, ($\mathbf{A}$) the magnitude of the vector potential, A_0, is related to the magnitude of the electric field vector, E_0, via the equation, $E_0 = A_0\omega/c$. Where ω is the frequency of the incoming light. By using this plane wave, the wave-vector ($\mathbf{k}$) and a direction of polarisation $\hat{\mathbf{E}}$ with the electrons in the atomic orbitals, the amplitude of the perturbation can be derived as:

$$\mathbf{A} = \hat{\mathbf{n}}A_0 cos\left(\mathbf{k}.\mathbf{x} - \omega t\right) = e\frac{A_0}{2}\left(e^{i(\mathbf{k}.\mathbf{x}-\omega t)} + e^{-i(\mathbf{k}.\mathbf{x}-\omega t)}\right) \tag{2.4}$$

The magnitude of the wave vector is related to the wavelength of the X-ray, $|\mathbf{k}| = 2\pi/\lambda$. $\mathbf{A}$ and $\mathbf{E}$ are collinear, they are related by $E_0 = A_0\omega/c$. After realising that only the time dependent term in (2.4) causes transitions which absorb energy and then by substituting (2.3) and (2.4) into (2.2) we can obtain the transmission probability.

$$P_{i\to f} = \frac{e^2E_o^2\pi}{2\hbar m^2\omega^2}\left(\left\langle f\left|\hat{\mathbf{E}}.\mathbf{p}\right|i\right\rangle\right)^2\rho\left(\varepsilon\right) \tag{2.5}$$

For this plane wave the number of photons per unit time can be determined by dividing the total energy flux of the wave by the photon energy.

$$\Phi = \frac{A_0^2\omega}{8\pi\hbar c} = \frac{E_0^2 c}{8\pi\hbar\omega} \tag{2.6}$$

Since the X-ray absorption cross section is given by $\sigma_x = P_{if}/\Phi$, we can obtain.[25]

$$\sigma_x = \frac{4\pi^2 e^2}{c\omega m^2} \sum_f \left| \frac{E}{|E|} . \langle f \left| \mathbf{p} \right| i \rangle \right|^2 \rho\left(\varepsilon\right) \tag{2.7}$$

The initial state, $|i\rangle$, which describes the sample before electron ejection, has a total energy E(N). The final state $|f\rangle = |\mathbf{k}\rangle \otimes |N-1\rangle$ is composed of the electron transferred to a vacuum state with a wavevector $\mathbf{k}$ and energy E_{kin} and the sample with total energy E(N-1) after electron ejection, thus $E_i = E(N)$ and $E_f = E_{kin} + E(N-1)$. Absorption of photons with a well defined energy promotes electrons from the sample into the vacuum in an ionisation process. The cross section for the ionisation process is given by Equ.2.7, but certain transitions are far less likely and since we are dealing with vectors the polarisation of the light and orientation of then molecule and therefore it's electron orbitals become very important.

2.2.2 X-ray Absorption Spectroscopy (XAS)

Due to the energies involved there is a large interaction cross section between soft X-ray photons and core electron energy levels. Hence a soft X-ray photon can excite core electrons to a higher energy level with a vacancy and since energy levels within an atom are quantised, photons of specific energy are required for each different excitation, so synchrotron radiation is essential.

After X-ray absorption the atom is left in an excited state due to the hole in the core level, see Fig.2.10. The two dominant relaxation processes are when an electron drops into the core hole and the excess energy is released by ejection of either an electron or photon, in either Auger decay or fluorescence respectively. The process pictured is not strictly an Auger decay since a true Auger process leaves the atom in a +2 oxidation state, with both the initially excited electron and subsequent electron both leaving the atom. A slightly different process can occur after XAS to a bound state, since the initial excitation did not eject the photon, after relaxation by electron emission the atom is only in a +1 oxidation state, hence this similar process is called Auger-like.

The excess energy released is equal to the difference in energy levels between which the electron drops. The kinetic energy of the emitted Auger-like

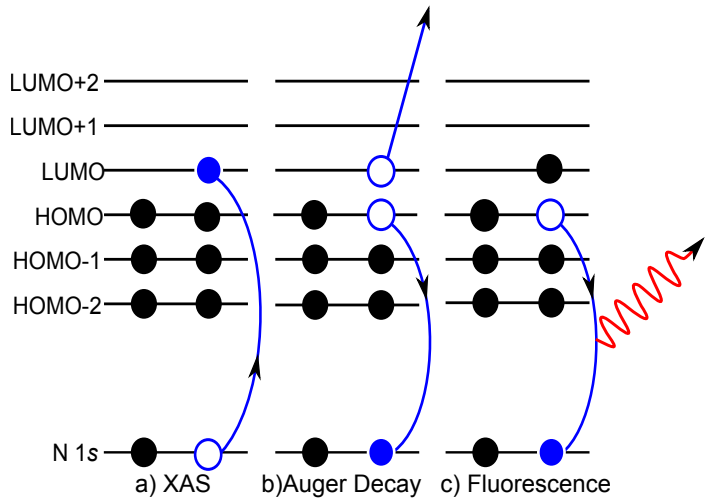

Figure 2.10: Excitation of a core level electron to a bound state XAS, followed by relaxation of the core-hole via Auger emission or fluorescence.

electron is $(E_c - E_n) - E_m$ where E_n is the initial energy of the electron which moves to the hole in the core, E_c is the energy of the core shell and E_m is the binding energy of the Auger electron. These binding energies have normally been increased relative to an atom in the ground state since the presence of the core hole provides less screening of the nucleus. Auger emission has an energy range which is typically in the 100-500 eV range.[19] At this energy level the mean free path through the substrate is a few nanometers, so the technique is highly surface sensitive. The number of Auger electrons emitted from the sample is directly proportional to the amount of X-ray absorption.[25] To count the number of Auger electrons emitted either a separate detector is placed under the sample with a positive bias to capture most emitted electrons. Alternatively the hemispherical analyser can be configured to capture the number of electrons emitted over the kinetic energy of an Auger, the work contained in this thesis used both techniques.

In a molecular system with well defined unoccupied orbitals, as the photon energy is increased there is an increase in the emitted intensity of Auger electrons. The first increase or peak occurs when the photon energy matches the energy difference between the core level and the LUMO. Subsequent peaks

in intensity are excitations to the LUMO+1 LUMO+2 etc, hence the energy levels of the unoccupied states of the system are probed. If the data has been measured using a hemispherical analyser it will produce an image such as Fig.2.11 a) a 2D line profile is taken from this 3D XAS data set by integrating with respect to the photon energy to produce Fig.2.11 b) indicating the variation in absorption of X-rays at different photon energies. In each case the approximate positions of the LUMO, LUMO+1 and LUMO+2 are indicated.

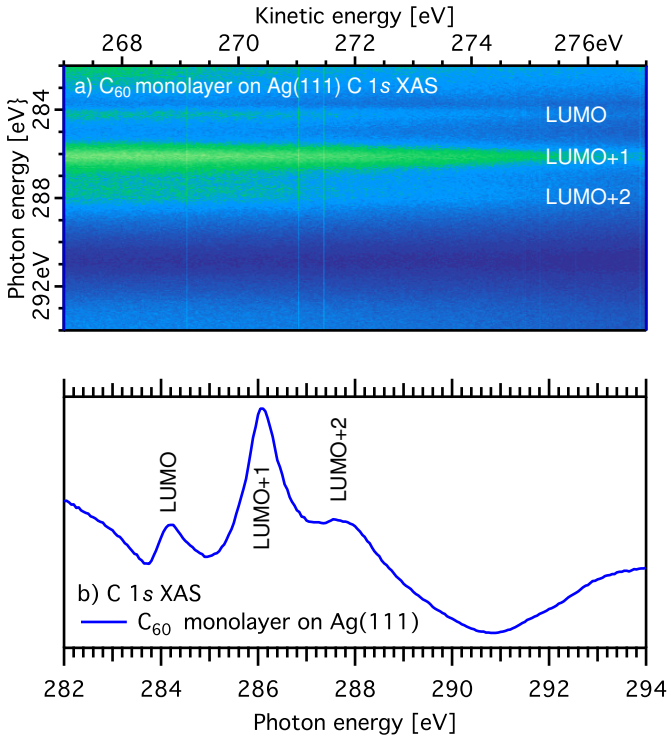

Figure 2.11: C 1s XAS example C_{60} monolayer on Ag(111) a) raw data from hemispherical analyser b) the integral of this data with respect to photon energy.

When the monochromator is set to a specific value, photons of integer multiples of that value will also pass through. Hence it is possible to make measurements at the appropriate binding energies of core electrons that have been emitted by the primary energy or 1st order light and 2nd order light with double the primary excitation energy. Hence after XAS is completed and without changing the monochromator position of a core state such as C

1s using both the first and second order light is measured. The difference in kinetic energy between these two peaks allows the measurement of photon energy at the end of the scan and thus gives a photon energy calibration point.

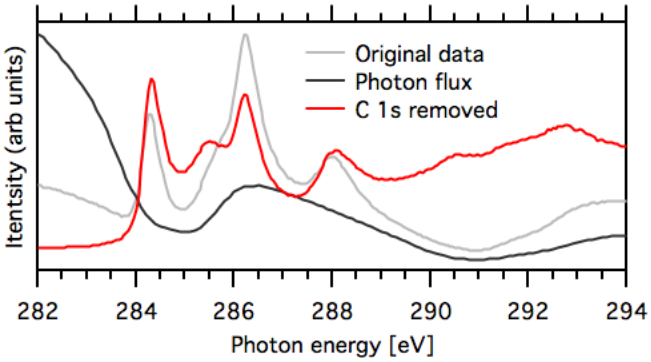

Figure 2.12: Data processing, original data from Ag C 1s XAS, grey. From this the carbon dip, black, is removed to produce red.

If the flux of photons at different photon energies is not constant across the XAS image some processing of the data is required, this is shown in Fig.2.12. This is especially true at the C 1s edge due to carbon on the mirrors of the monochromator since this contamination causes absorption and a variation in the beam intensity during the scan. To remove this from the data set and obtain a real density of unoccupied states a XAS of a clean metallic surface is taken to measure the variation in photon energy across the edge. This is shown in black and the original data is divided by it. Hence the carbon dip is now removed and the spectra now clearly shows the unoccupied orbitals, (red line in Fig.2.12).

2.2.3 X-ray Photoemission Spectroscopy (XPS)

While XAS uses a range of photon energies and counts the number of emitted electrons, XPS uses a fixed photon energy then measures the kinetic energy and number of emitted electrons. If a soft X-ray photon has greater energy ($h\nu$) it can excite core electrons to an unbound state, thus ionising the atom and providing kinetic energy to the emitted electron (E_{kin}). In such a case the binding energy can be expressed as the energy difference between the initial

state with N electrons and the final state with N-1 electrons. This leads to the fundamental equation behind X-ray photoemission, namely the photoelectric law:

$$h\nu = E_{kin} - \left(E_f^{N-1} - E_i^N\right) \tag{2.8}$$

Where the kinetic energy is measured with respect to the vacuum level. Energies of free molecules and atoms tend to be stated relative to the vacuum level, however solid states tend to be described relative to the Fermi level. The previous equation is therefore modified slightly to make the binding relative to the Fermi level instead of the vacuum level:

$$h\nu = E_{kin} + E_B + \phi \tag{2.9}$$

where ϕ is the difference between the HOMO and the vacuum level, which is known as the work function of the material, E_B is the energy difference between the initial position of the excited electron and the highest occupied molecular orbital (HOMO). Those electrons that undergo excitation and are elastically ejected from the sample contribute to the XPS peaks, the basic concept of this is shown in Fig.2.13. Here a core electron is excited out of the atom due to energy gained from an X-ray photon, the binding energy of an 1s electron goes as Z^2 to a first approximation, where Z is the atomic number. Hence measurement of the binding energy will allow identification of atomic species.

Since these photoelectrons have a very limited mean free path through matter, the technique probes the core states of the atoms effective for the top 10 nm depth. Photons can penetrate deeper into most matter but electrons can only travel through a couple of atomic layers before an interaction. Hence this technique is very surface sensitive, so careful sample preparation and as much freedom from contamination as possible is required. Surface sensitivity can be further increased by adjusting the angle of the surface with respect to the analyser. Thereby altering the path that electrons have to take before reaching the detector and decreasing the depth that the detected electrons can be emitted from.

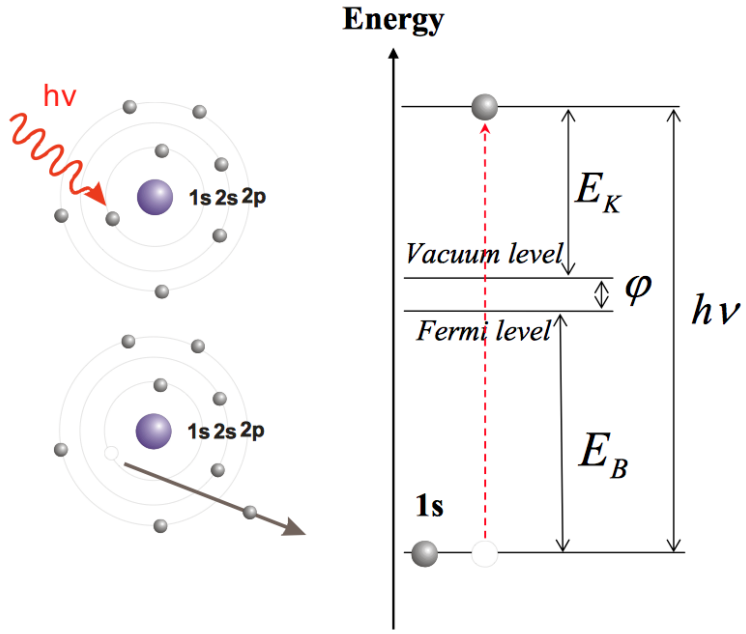

Figure 2.13: General concept of XPS, removal of core level electron through X-ray illumination with energy level diagram.

An overview spectrum of the clean TiO_2 surface is shown in Fig.2.14, the same spectrum was taken at two different photon energies to illustrate the constant binding energy XPS features such as O $1s$ and Ti $2p$ and $3p$ and the broader Auger features. These Auger features shift with the excitation energy because the energy of the emitted electron depends only on the difference between orbitals involved in core-hole decay and are therefore at constant kinetic energy, therefore there is an apparent shift in binding energy. The XPS peaks are due to electrons from the indicated atom and orbital, via the process already described that have undergone no inelastic processes. For both spectra there is a similar increase in the background level after each XPS and Auger peak on the higher binding energy side, this is due to an increase in inelastically scattered electrons, their loss of energy causing them to appear at higher binding energies.

The X-ray methods used here will tend to probe the binding energies of core electrons, due to the high interaction cross section. Core electrons have a localised wave function and therefore the energy does not depend on a wave

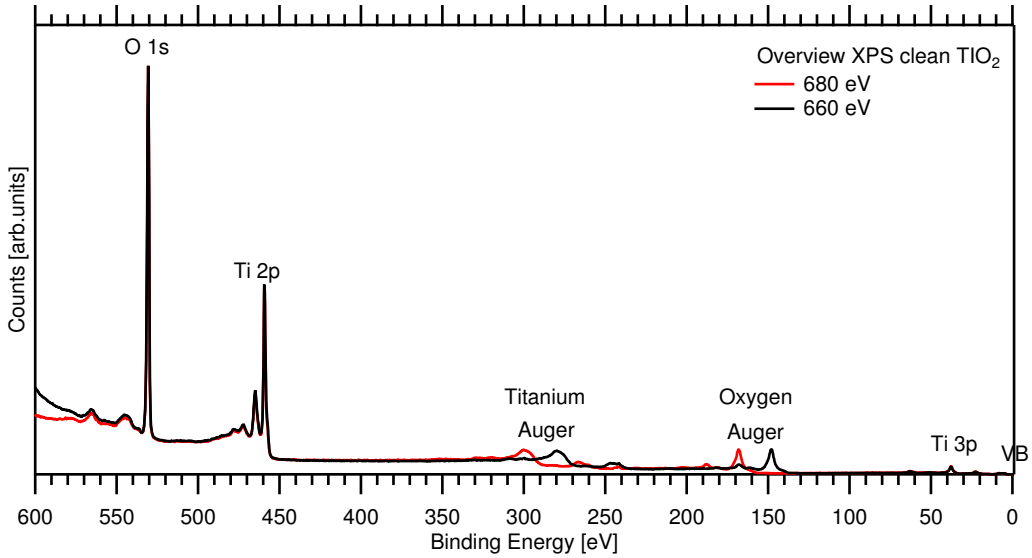

Figure 2.14: Example of an XPS overview taken on a clean TiO_2 surface, at two excitation energies, to show the fixed position of XPS peaks and excitation energy dependant position of Auger peaks.

vector. Due to random decay life-time of the core-hole, at a fixed photon energy we observe a range of Lorentzian peaks due to the element at the surface of the sample, each of which is at a characteristic binding energy. The core level spectrum will also have a Gaussian contribution due to instrument broadening of both the energy of electron in the analyser and incident photon energies from the monochromator. Hence a core state will be measured with Lorentzian and Gaussian broadening like those seen in Fig.2.15. These XPS peaks are constructed by having a small range of kinetic energy electrons indent on the detector then taking small increments in those energies. The software then totals the number of counts for each of the predefined energies that swept across the detector.

Although the core-level electrons are not directly involved in the formation of bonds, any change in the chemical environment of the element will involve spatial and energetic redistribution of the valence electrons in the atom and create a different potential at the core.[27] Changes in potential at the core causes a shift in binding energy which can be detected using XPS, for example in Fig.2.15(left) the C 1s spectra shows four different bonding environments

for carbon atoms. Hence as well as element identification we can acquire information about chemical bonding of those element and absorbed molecules at a surface using this technique. In the diagram on the left of Fig.2.15 again the effect of the inelastic scattering electrons it is clearly seen by the background on the higher binding energy side. This effect has been removed for the diagram on the left by doing a Shirley background removal,[28] which is used throughout this work. The diagram on the right shows such a spectra after background removal, it also indicates how more subtle differences in bonding can combine to give the complete measured XPS spectra. This can also give us evidence that molecules remain intact after deposition or interaction and bonding with the surface.

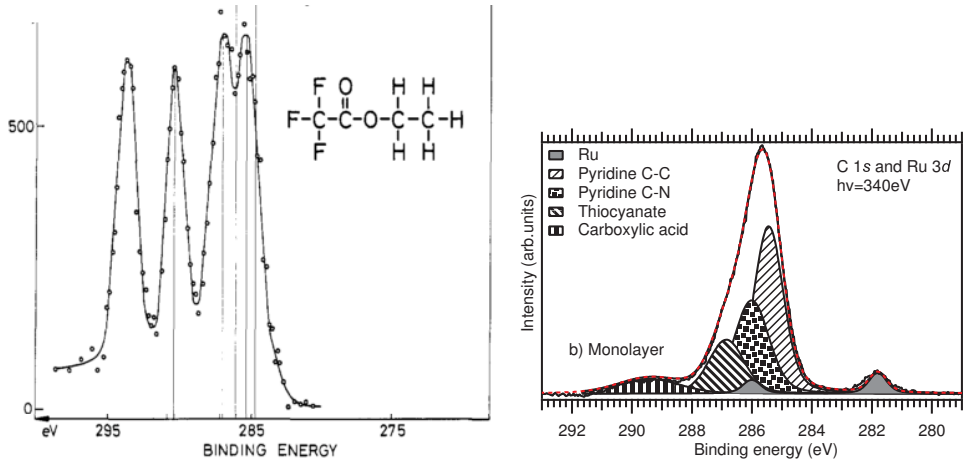

Figure 2.15: C1s XPS of; left Ethyl-trifluoroacetate from ref [27] and right N3 on ultra thin alumina, taken from Fig.3.2, both Figures illustrate the different chemical environments identifiable for one element in a molecule. see text from more detailed description.

Energy of ultra violet light is similar to valence electrons hence when UV illumination is used instead of X-ray the highest occupied molecular orbitals can be probed. During XAS as the photon energy is increased an intense signal is first seen when the photon energy matches the energy difference between the core level and the LUMO, there after it measured the position of the other unoccupied states. Therefore if the valence band and XAS can be calibrated to the same point then it is possible to place the valence band of the highest occupied molecular orbitals and XAS of the lowest unoccupied states onto

the same binding energy states to reveal the density of states of the system around the Fermi level. These density of states plot are particularly useful for DSC since possible molecule and surface interactions with visible light can be assessed. To achieve this end the valence band and binding energy of the core state are calibrated with either the Fermi level or binding energy of a known core state. We then can take the starting position of the XAS and shift it in the negative X axis direct by a value equal to the binding energy of the core state, for example on C 1s XAS the shift is equal to the C 1s binding energy. The XAS is then flipped in the y axis since increasing photon energy in XAS represents decreasing binding energy of the orbital. Then with the valence band calibrated to the same point as the C 1s core level used to shift the XAS the two are placed on the same binding energy axis and normalised in intensity. Hence the occupied and unoccupied states on the same binding energy scale, see example Fig.2.16. This process is taken from and described in future detail in ref[29].

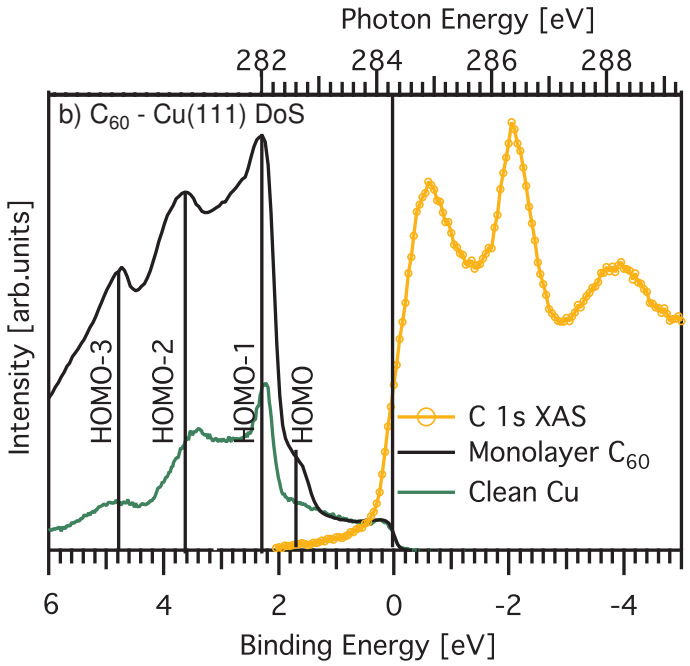

Figure 2.16: Example of density of states plot for C_{60} on Cu, taken from Fig.5.8

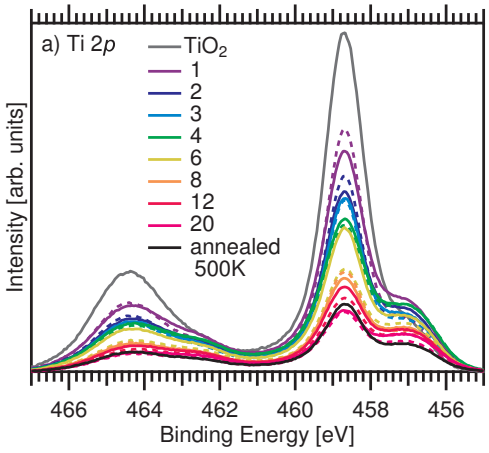

Figure 2.17: The Ti $2p_{1/2}$ on the left is half the size of the Ti $2p_{3/2}$ on the right, for further explanation of this figure see Sec.4.3.2

2.2.4 Spin-orbit coupling

Electrons paired in a core atomic orbital interact with each other to conserve total angular momentum j, which consists of electron spin s, and orbital angular moment l, such that j = s + l. After an electron is emitted from a core orbital through photoemission the remaining electron can have either spin s = $+^1/_2$ or s = $-^1/_2$ and zero orbital angular momentum. If the electron is emitted from an orbital where l is nonzero, such as a p, d or f orbital where l= 1, 2 or 3 respectively, l and s must couple in order to conserve angular momentum. This interaction causes a spilt in the final state energy levels of the exciton and therefore two different binding energies are measured for the emitted electron. Thus spin-orbit coupling causes a shift in an electron's binding energy measured in XPS, so instead of the singular peaks observed for an s orbital excitation, two peaks will be observed for p, d and f orbitals.

For example, the Ti $2p$ orbital has s = $\pm^1/_2$ and l = 1, therefore the total angular momentum j = $^1/_2$ or $^3/_2$. Since the number of electrons in each j state is given by 2j + 1, there must be 2 and 4 electrons in the j=$^1/_2$ and j=$^3/_2$ states respectively. Therefore the two Ti $2p$ peaks observed in XPS will have an intensity ratio of 1:2, see Fig.2.17.

2.2.5 Resonant Photoemission Spectroscopy (RPES)

Resonant photoemission spectroscopy allows understanding of the channels that are available during core-hole decay. It allows qualitative and quantitative understanding of the charge transfer dynamics between the surface and the adsorbate. The technique has relevance to exciton dissociation and charge transfers processes in DSCs, since charge transfer due a valence hole in a DSC is highly comparable to core-hole process in RPES.[30] RPES is quite similar to XAS, the only difference is that the kinetic energy of the emitted Auger and Auger-like electrons is now recorded and becomes part of the analysis. By measurement of the kinetic energy of the emitted Auger electron with respect to the initial excitation energy of the photon we can understand the various decay mechanisms that are available to the core-hole to a high degree of surface sensitivity. The states that electrons are promoted to in RPES are very similar to those that occur due to optical excitation, except that RPES is in the presence of a core-hole. Hence RPES is a useful process for investigating fundamental processes related to solar cells, since it involves similar exciton and subsequent relaxation.

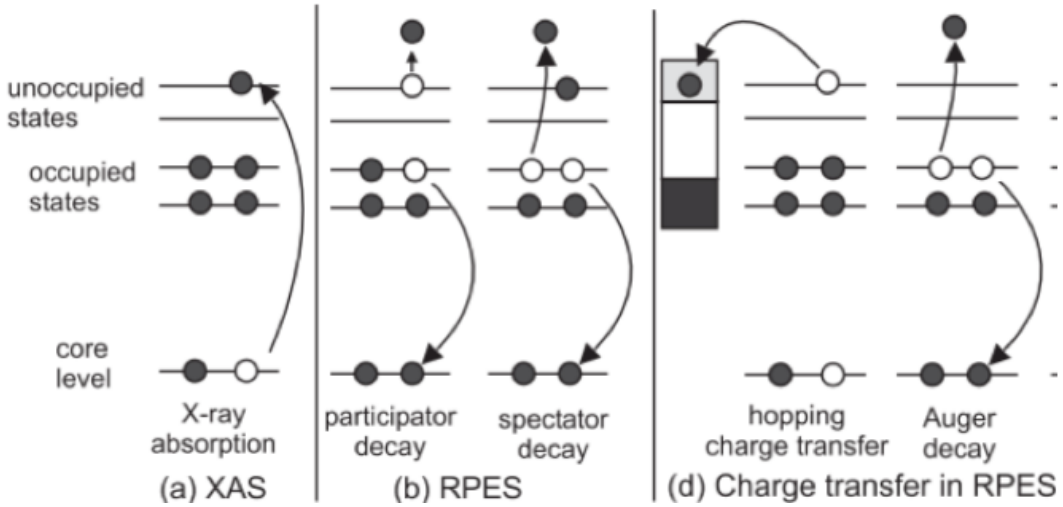

Figure 2.18: Core-hole decay mechanisms for resonant photoemission, see text for further explanation.

Different decay mechanism must be distinguished in order to further understand the relaxation process, these are shown in Fig.2.18. Fig.2.18(a) shows

the preferential core level excitation of an electron from core to unoccupied state (LUMO+1) during XAS. Fig.2.18(b) represent Auger-like emission of the participator electron where the already exited electron participates in the decay process by taking away the excess energy, hence the term *participator* decay. Participator decay leads to a final state identical to that of direct photoemission from the HOMO, hence this process emits an Auger electron with constant binding energy. This process is only available if the electrons in the excited state are not able to tunnel away before they participate in the Auger-like core-hole decay process, hence this is expected in molecules isolated from the surface such as those found in a multilayer and for those states that do not overlap with the available states in another system. Fig.2.18(b) also shows spectator decay, here the process is very similar to normal Auger decay, however, instead of the original excited electron being removed from the atom as in photoemission it is instead excited to a bound state as described in XAS, subsequently the excited electron spectates on the decay of another electron from the valence band to the core and the excess energy is emitted via the kinetic energy of another electron. Spectator electrons and Auger decay are features with constant kinetic energy, since the energy of the electron comes from the constant energy shift of the occupied state to core level decay and does not depend on the initial excitation energy, only the presence of a core-hole. The process in the Fig.2.18(spectator and Auger) involves two electrons from the HOMO which will give the highest kinetic energy of emitted electrons. This process results in a lower energy emission than participator decays since the final state of the system also represents emission direct from the HOMO with an addition excitation of another electron. Figure (d) represents charge transfer after XAS, this is where the excited electron tunnels into the substrate, followed subsequently by relaxation of the core hole similar to spectator decay. If charge transfer occurs then the resulting relaxation takes place from the ionised system which only has discrete states available for decay in a true Auger process. The transferred electron removes the excess energy from the molecule, hence this decay will exhibit constant kinetic energy.

An example of an RPES image is shown in Fig.2.19. Horizontal feature on the RPES scans represent an increase in electrons emitted at these pho-

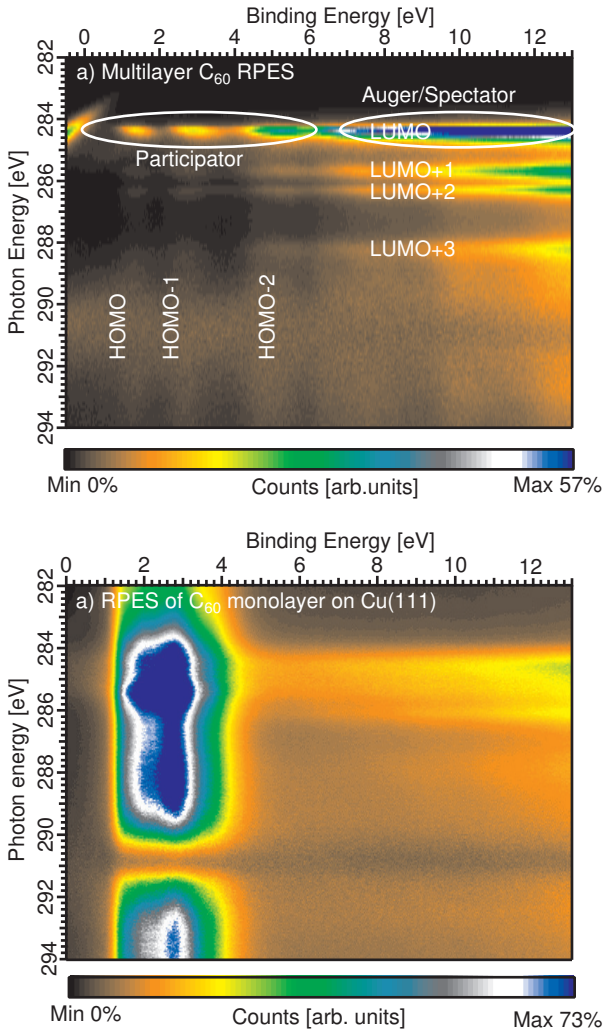

Figure 2.19: RPES spectra for a multilayer or isolated molecules of C_{60} (above), indicating the positions of the unoccupied states (horizontal features) and RPES spectra for monolayer of C_{60} on Cu(111) showing vertical features that are due to the highest occupied states of the Cu(111) substrate, taken from Fig.5.2(a) and Fig.5.8(a).

ton energies, hence these represent unoccupied states in a process similar to XAS. Vertical features are at constant low binding energy and therefore represent the valence band. This combination allows measurement of emissions from specific orbitals at specific photon energies. Participator decays have a final state identical to the direct emission from an occupied orbital. They are therefore seen as spots such as those circled in Fig.2.19a), where the three circles represent excitation to the LUMO and participator decay involving an electron in either the HOMO, HOMO-1 or HOMO-2. These features are also less clearly seen at higher photon excitation energies, mostly due to the lower interaction cross section of the absorption. When the incident photon energy has a higher interaction cross section with the highest occupied levels of the underlying surface then clear vertical features are seen on the RPES image such as that in blue on Fig.2.19b) these features tend to be from continuous valence of substrates rather than absorbed species.[26] RPES images require similar calibration in photon energy to XAS using first and second order light, horizontal features can be calibrated to the valence band of the system. C 1s XAS also shows the second order C 1s XPS diagonal line, which is partially viewable at the top left of the image Fig.2.19a), since the energy of the second order light doubles with photon energy this leads to diagonal features with a negative gradient of -1. Spectator and Auger features have a binding energy that is not dependant on the photon energy, they will also appear at higher binding energies since less energy is given to the expelled electron compared to spectator decay. These processes are seen on RPES images as horizontal line features such as those indicated on Fig.2.19.

Hence the horizontal, vertical and -1 gradient features of an RPES are relatively easy to explain and also allow calibration. However the diagonal features with unity gradient, representing a constant kinetic energy feature would represent a super Auger/super spectator feature requires further explanation and is investigated further in Chapter 6.

2.2.6 Core-hole clock analysis

Since XAS represents the full intensity of the unoccupied levels, whereas in the case of RPES the unoccupied states may be depleted by charge transfer into the surface. The presence of a participator signal in molecules isolated from the surface shows that some of the excited electrons are not able to tunnel away during the lifetime of the core-hole, which is to be expected if the solid form of the deposited dye is non-conducting. However in the monolayer if this signal is depleted it represents charge transfer from the dye and into the surface on a time scale similar to or faster than the core-hole relaxation.

The application of the core-hole clock relies on two main assumptions. Firstly, the charge transfer and core-hole relaxation are independent. Secondly that the probability of charge transfer and the core-hole decay decrease exponentially with time.[26]

The number of molecular systems in the excited state at time t, is given by:

$$N(t) = N(0)exp^{\frac{-t}{\tau}} \tag{2.10}$$

Where τ is the timescale of the core-hole, charge transfer or other event of interest, and N(0) is the initial number of excited systems. The probability of core hole decay P_d where τ_d is the average lifetime for core hole decay.

$$P_d(t) = \int_o^t exp^{\frac{-t'}{\tau_d}} dt' \tag{2.11}$$

Similarly the probability of charge transfer not occurring before time t is given by:

$$P_{(noCT)}(t) = 1 - \int_o^t \frac{1}{\tau_{CT}} exp^{\frac{-t'}{\tau_{CT}}} dt' \tag{2.12}$$

where τ_{CT} is the average time of charge transfer. Since these two events are considered independent the probability of charge transfer occurring at any time is given by combining the previous two equations, to give:

$$P_{(d\&CT)}(\infty) = 1 - P_{(d\&noCT)}(\infty) = 1 - \left(\int_0^\infty \frac{1}{\tau_d} exp^{\frac{-t'}{\tau_d}} dt' \left[1 - \frac{1}{\tau_{CT}} \int_a^b exp^{\frac{-t'}{\tau_{CT}}} dt' \right] \right) \tag{2.13}$$

$$P_{(d\&CT)}(\infty) = 1 - \frac{\tau_{CT}}{\tau_d + \tau_{CT}} \tag{2.14}$$

$$P_{(d\&CT)}(\infty) = \frac{\tau_d}{\tau_d + \tau_{CT}} \tag{2.15}$$

This probability can be constructed in terms of the experimental intensity of normal Auger (I_{normal}) and resonant Auger ($I_{resonant}$) channels:

$$P_{(d\&CT)}(\infty) = \frac{I_{normal}}{I_{resonant} + I_{normal}} \tag{2.16}$$

Normal Auger and Spectator Auger processes are too similar in energy to be separated, however as seen in the PRES data, the participator peaks for the multilayer molecules can be easily measured. The decrease in the participator peaks between the multilayer and the monolayer $I^{multi}_{participator}$ - $I^{mono}_{participator}$ can be normalised to the isolated participator channel to determine the probability of charge transfer through that channel

$$P_{(d\&CT)}(\infty) = \frac{I^{multi}_{participator} - I^{mono}_{participator}}{I^{multi}_{participator}} \tag{2.17}$$

Hence

$$\frac{\tau_d}{\tau_d + \tau_{CT}} = \frac{I^{multi}_{participator} - I^{mono}_{participator}}{I^{multi}_{participator}} \tag{2.18}$$

$$\frac{\tau_d + \tau_{CT}}{\tau_d} = \frac{I^{mono}_{participator}}{I^{multi}_{participator} - I^{mono}_{participator}} \tag{2.19}$$

Since experimentally the signal will decrease in the monolayer compared to the multilayer, due to fewer molecules we must normalise the participator peaks, leading to the final core-hole clock equation which allows experimental measurement of the charge transfer time relative the lifetime of the core-hole.

$$\tau_{CT} = \tau_d \frac{I^{mono}_{RPES}/I^{mono}_{XAS}}{I^{multi}_{RPES}/I^{multi}_{XAS} - I^{mono}_{RPES}/I^{mono}_{XAS}} \tag{2.20}$$

When fitting a curve to an XAS or RPES peak such as those in Fig.2.16 the main variables are the position, intensity of the the peak and the Voigt line profile which is formed from Lorentzian and Gaussian broadening mechanism. Obtaining a fit for a single peak involves small errors in these variables. However similar peaks on a Multilayer and Monolayer will vary. In order to compare them the same position and Voigt function should be used and only the intensity varied. With the comprising fit somewhere in-between the ideal fits for the multilayer and monolayer, the degrees of freedom mean that it is down to the researcher's interpretation to find the ideal compromise for the curve fit. Hence the only logical way to do this is to repeat the fits many times using different parameters. During this thesis the key result taken from the fit is the area of the peak, since this is used in the core hole clock calculation. Hence all core hole clock calculations are calculated by taking many measurements of the peak area from different, but always visually reasonable fit parameters, and the result given is always the mean, with the standard deviation of the result quoted as the error.

2.2.7 Surface coverage

Once a thin film or molecule has been deposited on the substrate the thickness of the film, or number of monolayers must be calculated. A thin film or multilayer coverage of molecules can be estimated by looking at the suppression of an underlying substrate peak, with the equation:

$$d = \frac{-\lambda}{cos\phi} ln\left(\frac{I}{I_0}\right) \tag{2.21}$$

Where d is the film thickness, λ is the inelastic mean free path of the substrate photoelectrons through the adsorbed material, I_0 = integrated intensity of the XPS peak of the clean substrate, I is the integrated substrate intensity of the same peak after deposition and ϕ photoelectron emission angle with respect to the surface normal.

For sub monolayer formulas the Charley and Roberts equation[31] is required:

$$\sigma_A = \frac{KE_A}{KE_S} \times \frac{I_A}{I_B} \times \frac{\mu'_S N_A \lambda_S \rho_S cos\phi}{\mu'_A M_S} \tag{2.22}$$

Where σ_A is the surface concentration, A adsorbate and S the underlying substrate, KE kinetic energy, μ the photoionisation cross section, N_A Avogadro's number, M_S the molar mass of substrate and ρ_S the substrate density.

The inelastic mean free path (IMFP) λ (in $\dot{A}$) through the molecule was approximated as a function of electron energy, it can be calculated via TPP-2M predictive equation[32], as a function of electron energy, E (in eV) given by the equation:

$$\lambda = \frac{E}{E_p^2 \left[\beta ln\left(\gamma E\right) - \left(C/E\right) - \left(D/E^2\right)\right]} \tag{2.23}$$

where:

$$\beta = -0.10 + 0.944(E_p^2 - E_g^2)^{-1/2} + 0.069\rho^{0.1} \tag{2.24}$$

$$\gamma = 0.191\rho^{-1/2} \tag{2.25}$$

$$C = 1.97 - 0.91U \tag{2.26}$$

$$D = 53.4 - 20.8U \tag{2.27}$$

$$U = N_\nu \rho / M = E_p^2 / 829.4 \tag{2.28}$$

Where Ep = 28.8 $(N_\nu \rho/M)^{1/2}$ is the free-electron plasmon energy (in eV). E is the electron energy in eV, N_ν for compounds is the number of valence electrons per atom, M is the atomic or molecular weight . ρ is the density (in g cm^{-3}), E_g is the band-gap energy Ms = Molar mass of substrate. Hence the calculation of the mean free path through the adsorbed material enabled the calculation of thin film thicknesses or molecule coverage.

Chapter 3

N3 on $Al_{10}O_{13}$

The interaction of the dye molecule N3 with the ultra-thin oxide layer on a AlNi(110) substrate, has been studied using synchrotron radiation based photoelectron spectroscopy, resonant photoemission spectroscopy (RPES) and near edge X-ray absorption fine structure spectroscopy (XAS). Calibrated X-ray absorption and valence band spectra of the monolayer and multilayer coverages reveal that charge transfer is possible from the molecule to the AlNi(110) substrate via tunnelling through the ultra-thin oxide layer and into the conduction band edge of the substrate. This charge transfer mechanism is possible from the LUMO+2&3 in the excited state but not from the LUMO, therefore enabling core-hole clock analysis, which gives an upper limit of 6.0 ± 2.5 fs *for the transfer time. This indicates that ultra-thin oxide layers are a viable material for use in dye-sensitized solar cells (DSC), which may lead to reduced recombination effects and improved efficiencies of future devices.*

3.1 Introduction

In a dye-sensitised solar cell (DSC), a photo excited dye injects an electron into the conduction band of the substrate. DSCs offer a potential lower cost alternative to their inorganic counterparts, with cheaper materials and manufacturing processes.[33] They can also be engineered into flexible sheets, making them easier to transport and install.[34] DSC are currently less efficient than other thin film technologies such as CuInxGa$_1$-xSe$_2$ or CdTe.[8] How-

ever, the lower cost makes them a very competitive alternative. Ultra-thin oxide layers have already improved the performance of inorganic solar cells, by reducing recombination affects at surface defects through passivation.[35] In DSCs reduced recombination rates have been attributed to surface passivation, with the aluminium oxide coating serving as a tunneling barrier between the redox mediator and conductive electrons, (see Sec.1.2).[36] Hence aluminium oxide layers between a dye and TiO_2 substrate have been shown to increase power conversion efficiency,[37] by reducing dark current and increasing electron lifetimes.[38] A thicker oxide layer will reduce recombination rates[39] but also suppress the injection of an electron into the substrate,[40] an optimal thickness should be obtainable. An ultra-thin oxide may provide an attractive option for future DSC devices by passivation of the surface, therefore reducing recombination effect with minimal disruption to charge injection. However the potential for ultra-thin oxide layers to be used for this application has not been extensively studied. In this chapter charge transfer from a dye molecule through an ultra-thin oxide layer and into the underlying substrate is investigated, thus giving important information on the fundamental processes which will affect future DSC devices.

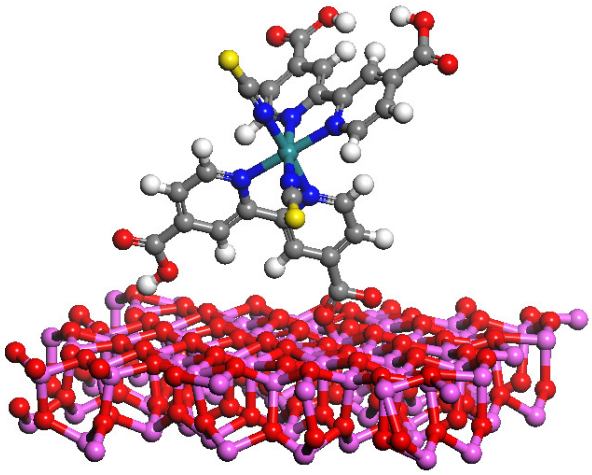

Figure 3.1: Schematic of N3 molecule on ultra-thin aluminium oxide layer. O - Red, H - White, C - Grey, N - Blue, S - Yellow, Al - Purple. The underlying AlNi(110) substrate is omitted.

The dye molecule N3 (cis-bis(isothiocyanato)bis(2,2-bipyridyl-4,4'-dicarboxylato)-

ruthenium(II)), shown in Fig. 3.1, was chosen because of its performance as a photosensitive molecule used in the construction of DSCs. It was unmatched for 8 years and as such it has become the benchmark for heterogeneous charge transfer in mesoporous solar cells.[41] For N3, if rapid charge injection can take place out of the molecule then chemical transformations cannot occur. This leads to a highly stable solar cell arrangement that can operate for approximately 20 years, without noticeable loss in performance.[41]

The aluminium oxide surface is one of the most intensely studied metal oxide surfaces, but most previous applications relate to models of catalysts.[42] A well ordered oxide layer is not formed on pure aluminium,[43] however, oxidation of clean AlNi(110) does form a well ordered, self terminating, ultra-thin oxide layer on the surface. The stoichiometry of this oxide is $Al_{10}O_{13}$,[44] and previous studies have reported on the spectroscopy and organisation of this surface.[44, 45] The film self terminates at three atomic layers because oxygen in the gas phase does not dissociate on the oxygen terminated surface.[42] Since the oxide layer is only three atomic layers thick and the ultra thin film is an semi conductor with a band gap, measured from XPS and XAS density of states, as 6.7 eV[46] there is potential for electrons to easily tunnel from the dye through the oxide and into the underlying AlNi substrate, while still reducing recombination affects. Thus $Al_{10}O_{13}$ on AlNi(110) provides a model for a DSC device which could be developed in the future.

In order to develop our understanding of N3 on $Al_{10}O_{13}$, its bonding must first be considered. Prior research of N3 on Au(111) showed that the bonding is dominated by the sulphur atom on the thiocyanate and van der Waals forces from the remainder of the molecule.[23] On TiO_2 N3 has been shown to bond via de-protonation of two carboxylic acid groups on the bi-isonicotinic acid ligand, and via the interaction of sulphur on the thiocyanate ligand.[22] Since the surface in this experiment is oxygen terminated it is expected that N3 will form chemical bonds with the surface in a manner similar to that seen on TiO_2.[22] The O'Shea group have previously reported the charge transfer interaction of N3 and its bi-isonicotinic acid ligand on Au(111)[17, 47] and N3 as well as related water splitting molecules on TiO_2.[22, 48, 49] The upper limit for the charge transfer time from N3 to Au(111) and TiO_2 was 4.4 fs[47]

and 12 fs[48], respectively.

In order to further develop DSCs it's important that an understanding into the subtle bonding and electronic properties that lead to efficient photon-to-current efficiencies is achieved. Here X-ray photoemission spectroscopy (XPS) results are presented, which allowed characterisation of the bonding between the molecule and the surface. Resonant photoemission spectroscopy (RPES) as well as near edge X-ray absorption fine structure (XAS) that allow measurement of charge transfer interactions between the surface and the molecule.

3.2 Experiment

Experiments were carried out at the D1011 bending magnetic beamline at the MAX-lab Swedish synchrotron radiation facility. The beamline covers photon energies in the range 30 to 1600 eV, the end station is equipped with a SCIENTA SES200 (upgraded) electron energy analyzer and an MCP detector for electron yield measurements. The baseline operating pressure was 3×10^{-10} mbar.

The sample used was a single crystal AlNi(110) which was sputtered at 1kV and then flash annealed to 1300 K via ebeam heating. Subsequent sputtering and annealing cycles were repeated until C $1s$ and O $1s$ peaks were no longer observed in XPS. The oxide layer was formed by dosing the sample with 1800 L of O_2 at 3×10^{-6} mbar and 600 K, followed by an anneal at 900 K for 10 mins. Further details on the formation and detailed description of this oxide layer are given elsewhere.[45, 50] Other research[51, 52] have recommended a two step oxidation process, with high temperature (1050 K), in order to close open metal patches in the oxide layer. However during our analysis of the surface it became clear that slightly higher temperature annealing caused a significant reduction in the oxide signal in XPS. A lower temperature anneal following oxidation was therefore adopted. N3 obtained from Solaronix SA, Switzerland, was deposited via a ultra-high vacuum compatible electrospray deposition system (MolecularSpray, UK) with methodology described in Sec.2.1.6.[22] N3 has been shown to remain stable after electrospray deposition onto TiO_2[22, 48, 53] and Au(111).[23, 47] The dye molecule was dissolved in

a solution of 3(methanol):1(water) and sprayed for 90 mins during which the pressure rose to 2×10^{-7} mbar due to gas load from the electrospray system and the presence of solvent molecules in the molecule beam. This formed a deposition spot on the surface a few millimetres in diameter with a range of coverages in a Gaussian distribution, from partial monolayer at the edges to multilayer in the centre. The multilayer data was combined with data obtained in previously published experiments of N3.[22, 48]

All measurements were performed at room temperature. XPS data were calibrated to the Fermi edge. A Shirley background[28] was removed and the spectra normalised to the photon flux and the number of sweeps, before curve-fit analysis using pseudo-Voigt functions.[54] XAS data were recorded at the N $1s$ adsorption edge with the emitted electrons collected by a partial yield detector with a retardation potential of 200 V. For XAS and RPES the photon energy was calibrated by taking the energy separation of the Al $2p$ core-level photoemission peaks excited by X-rays in first and second order.

To calculate coverages the inelastic mean free path (IMFP) λ (in Å) through the molecule was approximated as a function of electron energy and calculated via the TPP-2M predictive equation.[32] This was then used to calculate surface concentration by looking at the increased intensity of the adsorbate C $1s$ peak in comparison to the suppression of the Al $2p$ surface. The IMFP was used in the Carley-Roberts formula[31] to calculate surface concentration, coverage was then calculated via the footprint of the molecule as measured in DFT analysis. In the multilayer the number of photoelectrons in PES, which came from substrate, or the layer of molecules, which were bonded to the substrate, was negligible. Hence this represents molecules that are isolated from the surface.

3.3 Results and Discussion

3.3.1 Adsorption bonding

To build a complete picture of the interaction between N3 and $Al_{10}O_{13}$ we must first consider the way the molecules bond to the surface. Fig.3.2 shows

the C 1s and Ru 3d XPS data for the multilayer (a) and the monolayer (b).

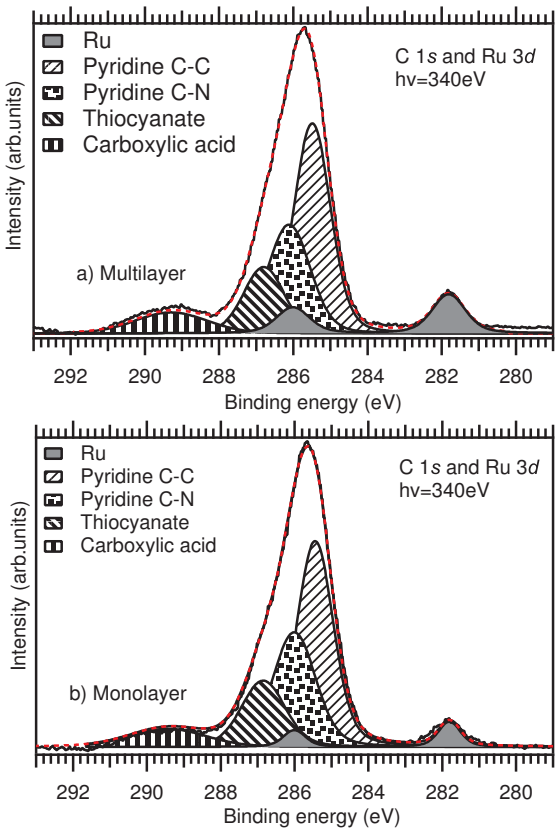

Figure 3.2: C 1s plot fit for (a) multilayer data and (b) monolayer, with different peaks for each of the different bonding environments of carbon. The ratios of the peaks fit with expected result for the intact molecule. Peak positions are the same across all coverages with the exception of the carboxylic acid peak, which is involved in intermolecular bonding in monolayer and multilayer coverages. hν=340 eV.

The normalised areas of the peaks in the multilayer should be in the ratio 6:4:2:1 when this ratio represents Pyridine ring C-C:Pyridine ring C-N:Carboxylic acid:Thiocyanate. The actual ratio when normalised to the Thiocyanate is 5.3:3.1:1.8:1.0 for the multilayer and 5.8:3.7:2.2:1 for the monolayer. Hence there is good agreement with expected results. Peak assignment also agrees with previously published data.[23] No change in energy of the C 1s peaks related to pyridine and thiocyanate was observed. These parts are in the same chemical environment in both the monolayer and multilayer, which

indicates that these parts of the molecule are not involved in bonding to the surface. The carboxylic acid peak is 7.6 eV above the Ru $3d$ peak in the case of partial monolayers and this shifts to 7.4 eV for the full-monolayer and multilayer coverages. This could be due to the carboxylic acid groups, which are not bound to the surface, being involved in intermolecular hydrogen-bonding to either the surface or other N3 molecules at coverages of a monolayer and above.

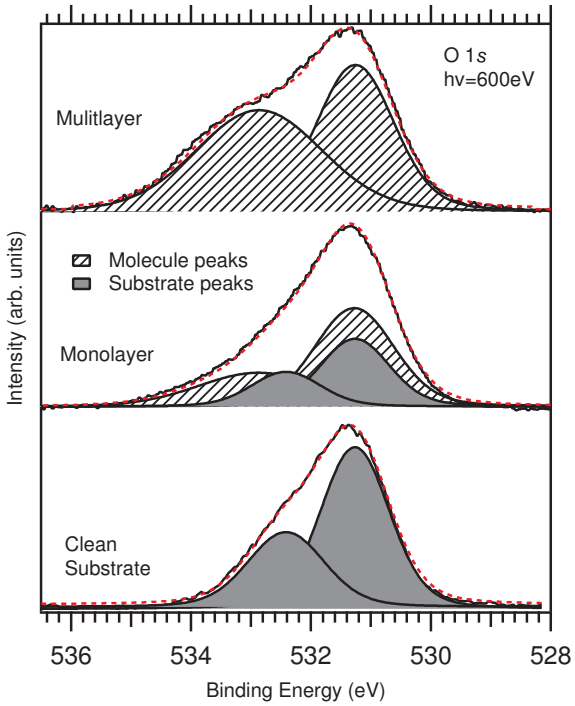

Figure 3.3: O $1s$ Plots normalised to the surface peak, black is background data of the clean surface with identical peak position and shape in the clean surface and monolayer, striped peaks are from the molecule with identical peak position and shape in the multilayer and monolayer. The ratio of the peaks in the monolayer suggest a combination of single and double de-protonation is involved when the molecule bonds to the surface. hν=600 eV.

Analysis of the O $1s$ spectra should indicate if the carboxylic acid group deprotonates and forms chemical bonds with the surface, XPS O $1s$ data is shown in Fig. 3.3. There are two O $1s$ peaks from the ultra-thin oxide layer with an intensity ratio of 2:1. The smaller peak at 533.0 eV binding energy is assigned to a fraction (8 out of 28) of the O $1s$ surface atoms, while the higher

intensity peak at 531.3 eV is due to the remaining surface atoms and the interface layer of oxygen atoms which lie directly on top of AlNi(110).[45] Two peaks related to the molecule are also observed in the monolayer and multilayer O 1*s* spectra. The peak at 533.0 eV binding energy is assigned to the C-OH carbon atoms[22] and thus represents carboxylic acid groups which have not deprotonated. The peak at 531.3 eV is assigned to C=O and deprotonated COO-.[22] In the multilayer, the ratio of the two peak areas is 1:1, which is to be expected as we have a 1:1 ratio of C-OH:C=O in the unbound molecule, where the carboxylic acid groups remain protonated.

In order to fit the monolayer data the peak position and shape of the multilayer and substrate peaks were kept the same as the multilayer and surface respectively. Only the intensity was adjusted to give the best fit, which gives a 2:1 ratio of C=O and COO-:C-OH. If both the carboxylic acid groups on one bi-isonotinic acid ligand had de-protonated and bound to the surface, we would expect to see a 3:1 ratio, as previously observed on TiO_2.[22] If only one carboxylic acid group had deprotonated we would expect a 5:3 ratio. Hence we have a different bonding environment to those previously observed for N3. Since a 2:1 ratio doesn't fit with the eight oxygen atoms in the N3 molecule we suggest the molecule can take on a range of different bonding geometries on this surface. Some molecules bond to the surface by a single bond via one deprotonation, while other molecules bond via de-protonation of two carboxylic acid groups on the bi-isonicotinic acid ligand. Similar multi-conformational adsorption geometries have recently been observed via low temperature STM of N3 on TiO_2.[53] It is also possible that bonds to the surface can form without deprotonation, thus forming monodentate structures.[55] Aluminum oxide prepared in UHV is prone to hydroxylation even under UHV conditions, so mismatch in O1s peak ratios could be due to presence of OH groups on the alumina surface.

Previous results for N3 adsorbed on rutile $TiO_2(110)$ exhibited two chemical environments in the S 2*p* region for the monolayer, indicating that one of the thiocyanate ligands were involved in the bonding to the surface.[22] Here, in contrast, only one spin-orbit split peak is observed in Fig. 3.4 for both the monolayer and multilayer, indicating that the thiocyanate group, is not

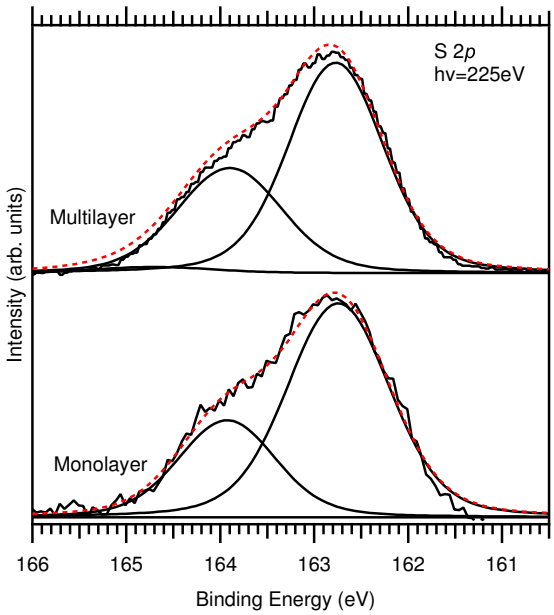

Figure 3.4: S $2p$ XPS showing the spin-orbit split S $2p\frac{1}{2}$ (left) and S $2p\frac{3}{2}$ (right) contributions, exhibiting a single chemical state for the sulphur atoms in the molecule with no binding energy shift at different coverage. Spectra were measured with hν = 225 eV and normalised to the height of the main peak.

involved in the adsorption bonding.

XPS measurements of the N $1s$ region, shown in Fig.3.5, show no change at different coverages, indicating the nitrogen atoms are not involved in bonding to the surface. This provides further evidence that the molecule is intact on the surface.

3.3.2 Electronic coupling

The occupied molecular orbitals and substrate densities of states were measured as a function of surface coverage. The valence band photoemission is shown in Fig.3.6 for a multilayer (d), monolayer (c), partial monolayer (b) and the clean oxide surface layer (a). Detailed peak assignments were made on the basis of previously published data for the clean surface.[46, 50] In these papers it was demonstrated that the peak around 2 eV is due to the underlying Ni d states in the bulk of the alloy, while the peaks between 5 eV and 10 eV are

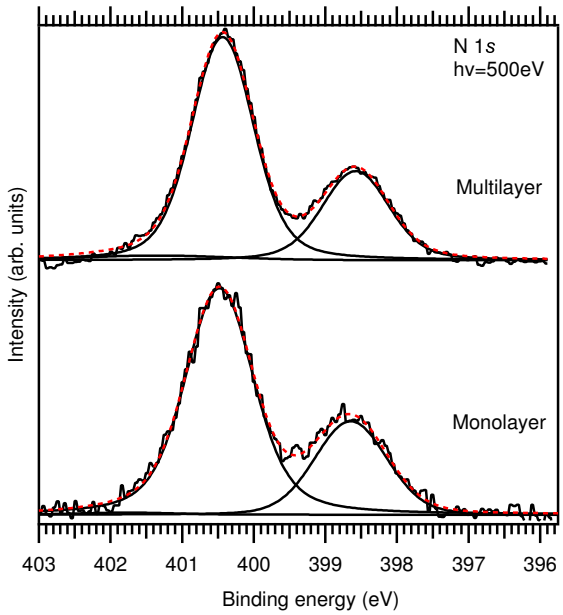

Figure 3.5: N 1s XPS measured for multilayer and monolayer of N3, indicating no change in chemical environment between different coverage. The larger peak is due to nitrogen in the bi-isonicotinic acid ligands, while the smaller peak is due to the thiocyanate ligands, with a 2:1 intensity ratio. Spectra were measured with hν = 500 eV and normalised to the height of the main peak.

due to the oxide layer, which was consistent with previously published angle resolved spectra.[50]

The unoccupied molecular orbitals can be probed by XAS, in this case at the N 1s absorption edge. This process is illustrated for excitation of the core-electron into the LUMO in Fig.3.7(a). If this resonantly excited state overlaps energetically with empty states in the substrate then charge transfer can occur. In the case of a thin oxide film on a metallic substrate there are two relevant conduction bands; that of the oxide and that of the metal substrate. The band gap of aluminium oxide at 6.7 eV[46] is too large for there to be any overlap of the oxide conduction band with the LUMO states of the core-excited molecule. However, if the oxide film is thin enough the excited electron may tunnel through the oxide and into the conduction band of the metal surface as shown in Fig.3.7(d), but only for those states that lie energetically above the Fermi level of the metal surface. To identify the

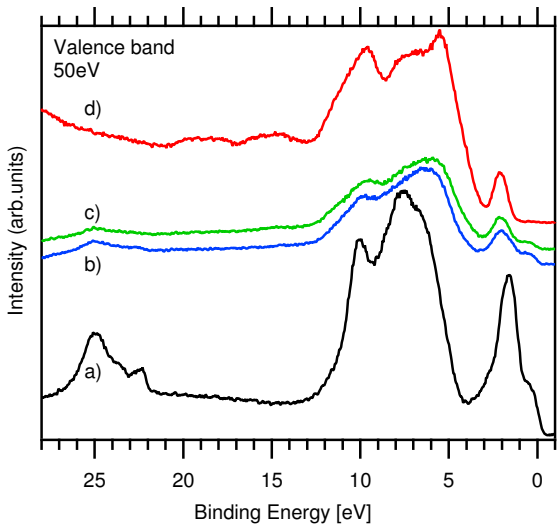

Figure 3.6: Valence band plots at varying coverages, a) clean substrate (black). Higher lines represent increasing coverage. b) partial monolayer (blue), calculated at 0.3ML c) monolayer (green) 0.85ML d) is a thick film or multilayer (red) 9ML. All taken at hν=50 eV.

relevant states that can participate in charge transfer from the molecule to the surface for N3 on $Al_{10}O_{13}$, the occupied and unoccupied states probed by valence band photoemission and x-ray absorption can be placed on a common binding energy scale using methods described in detail elsewhere.[29]. This data is shown for the N3 monolayer and multilayer in Fig.3.8.

The N 1s (Auger yield) XAS is shown in Fig.3.8 it was measured across the photon energy range 397-407 eV and placed on the binding energy scale via the N 1s binding energy in the pyridine group 400.8 eV. The binding energy of the pyridine N 1s core level was taken in preference to the N 1s binding energy of the thiocynate group. This is based on density functional theory (DFT) calculations[22] showing that the LUMO is located on the bi-isonicotinic acid ligand and the central Ru atom, with no intensity on around the thiocyanate ligand. The photon energy scale from the XAS is also indicated. The HOMO-LUMO gap in the monolayer is 1.5 eV and 0.8 eV in the multilayer. This is most likely due to surface screening in the monolayer of the excitonic energy shift induced by the core-hole,[56] resulting in the LUMO states being pulled down less energetically in the monolayer than in the multilayer. The band gap

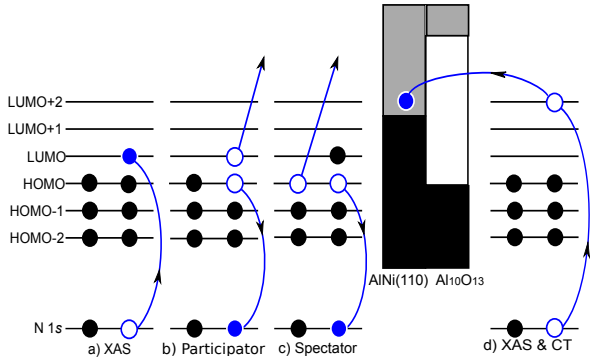

Figure 3.7: Electron excitation and subsequent core-hole induced decay processes: (a) x-ray absorption, resonant core-level excitation into unoccupied bound states; (b) participator decay; (c) spectator decay; and (d) x-ray absorption in the presence of charge transfer from molecular orbital into states near the fermi level of the metal substrate. For the substrate solid colour black white and grey represents occupied states, unoccupied states and band gap respectively.

of the oxide layer is drawn on as a guide, its location is taken from[46] and positioned relative to the Fermi edge. The position of the band gap indicates that charge transfer from the LUMO through to the LUMO+3 states into the oxide layer is not possible, thus any observed charge transfer must be tunnelling through the oxide layer and into the AlNi(110) substrate. Data for the monolayer shows that the LUMO+2 and LUMO+3 states of the molecule lie above the Fermi edge and therefore they overlap with the conduction band edge of the underlying AlNi, while the LUMO overlaps occupied states in the surface. This indicates that charge transfer into the substrate from the LUMO+2 and LUMO+3 of the monolayer is possible, but would not be available from the LUMO, and only partly available to the LUMO+1.

3.3.3 Charge transfer dynamics

In order to calculate an upper limit on the charge transfer time, the core-hole clock implementation of RPES was used, discussed Sec.2.2.6.[26] Fig.3.9 shows 2D RPES datasets for the multilayer (a) and the monolayer (b), each of which have been compiled from six individual data sets. The multilayer data shows

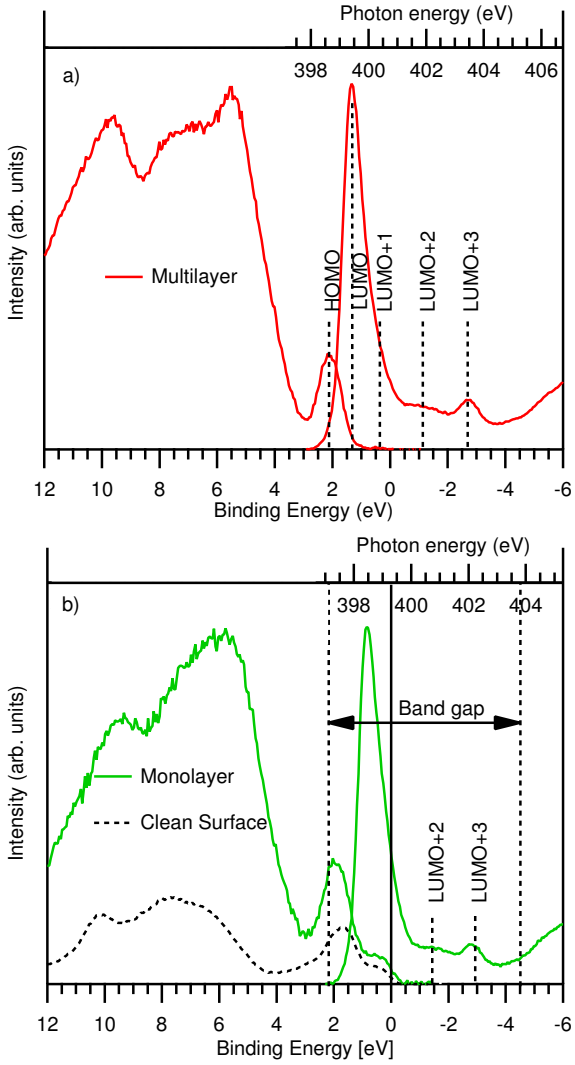

Figure 3.8: Density of States plot constructed from N 1s XAS and VB data, (a) multilayer and (b) monolayer coverage with the underlying substrate in black indicating a clear overlap between the unoccupied states of the molecule with the conduction edge of the AlNi(110) substrate.

an enhancement at 2 eV binding energy at the absorption photon energy of the LUMO and LUMO+1, which is attributed to participator decay resulting in resonant photoemission of the HOMO (only weakly visible in Fig.3.9). This is described schematically in Fig.3.7(b). Here, the excited electron is emitted in an Auger-like decay process and the final state of the atom is identical to photoemission from the HOMO state. Similar enhancements are also ob-

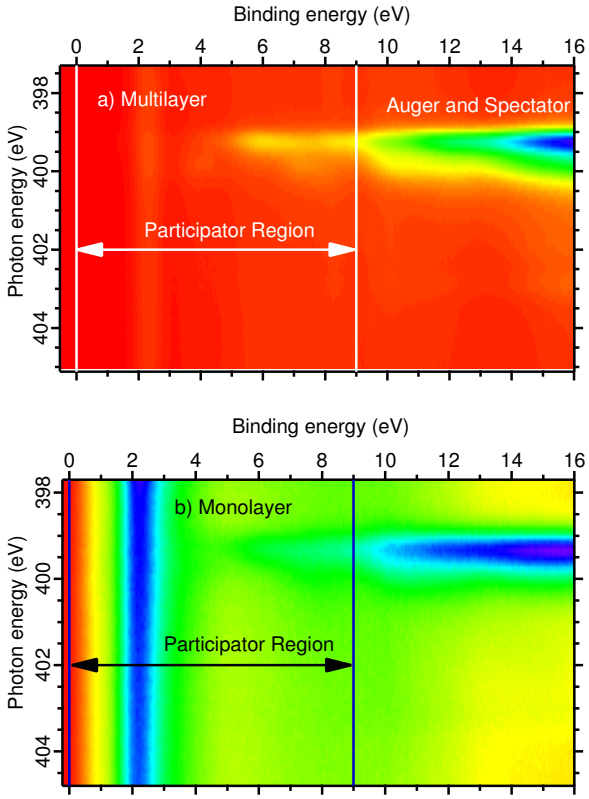

Figure 3.9: N 1s RPES multilayer (a) which is the sum of six individual RPES images, four of which are from,[22, 48] the monolayer (b) is also the sum from six individual RPES spectra. All images were normalised to the beam intensity. The integration window (0-9eV) for the core-hole-clock calculation is also indicated.

served for the other occupied molecular orbitals to varying degrees, including small enhancements at 4 and 7.5 eV binding energy and approximately 400 eV photon energy (labelled LUMO+1), and also a strong enhancement around 6 eV binding energy and 399.2 eV photon energy (labelled LUMO). These enhancements are due to spacial overlaps on the molecule between the different occupied and unoccupied orbitals, the LUMO at 399.2 eV and the occupied orbital at 6 eV overlap on the Bi-Iso ligand, while the LUMO+1 at 400 eV and the occupied orbitals at binding energy 4 and 7.5 eV overlap on the thiocynate ligand.[22] In order to measure the charge transfer time and enable core-hole clock analysis[26] this data was integrated over the region 0-9 eV binding energy. In this binding energy window there is some contribution from Auger and spectator decay in the region close to the photon energy of the LUMO, however proportionally this is the same for the monolayer and multilayer. Since this feature tracks out at constant kinetic energy, the contribution will be negligible at the LUMO+2&3 photon energies, where only the participator channel will be probed.

The results of the integration are shown in Fig.3.10 where the RPES and corresponding XAS from multilayer and monolayer data are normalised to the LUMO intensity. The background in the RPES is due to direct photon emission of the valence band, the cross-section for those states decrease with increasing photon energy, leading to an increase in the sloping background of the XAS compared to the RPES. The LUMO+1 is too close in energy to the LUMO for these peaks to be separated. Charge transfer from the LUMO into the surface is not possible since the LUMO lies below the fermi level. It was assumed more likely that charge transfer from the surface into the LUMO does not occur on the timescale of the core-hole lifetime since this would result in superspectator decay features as previously observed for bi-isonicotinic acid adsorbed on a Au(111) surface.[17] Such features are not observed here, but charge transfer within the lifetime of the core hole cannot be eliminated as a possibilty. By normalising the data to the LUMO channel for which no charge transfer is allowed for either the monolayer or the multilayer, changes in the intensity of the participator channel due to charge transfer out of the LUMO+2 and LUMO+3 states can be probed.

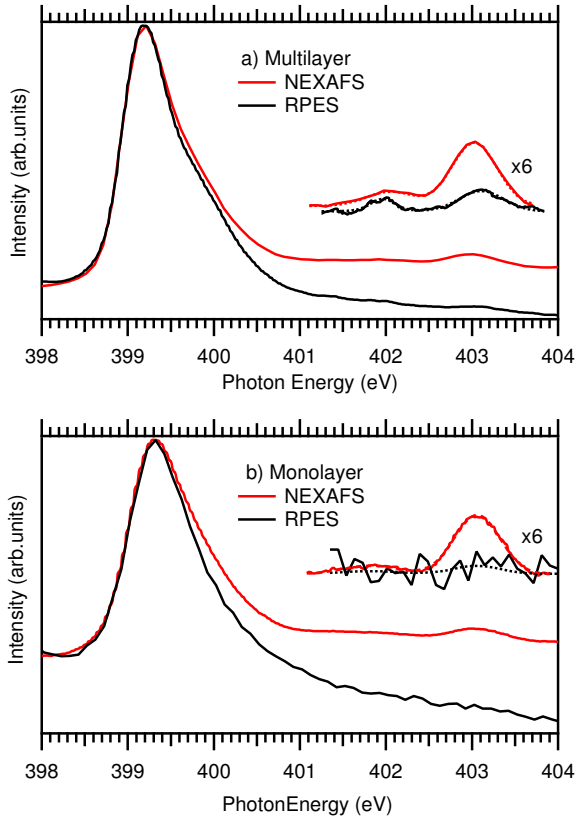

Figure 3.10: N 1s RPES and N 1s XAS spectra for the N3 multilayer (a) and monolayer (b). The multilayer data are integrations from 0 eV to 9 eV over all datasets. Also shown are the 6× magnification of the LUMO+2 and LUMO+3 regions after background removal.

The XAS represents the full intensity of the unoccupied levels, whereas in the case of RPES the unoccupied states may be depleted by charge transfer from the LUMO+2 and LUMO+3 into the substrate, hence in Fig.3.10 the LUMO+2 and LUMO+3 region of the RPES signal is lower than the XAS. The charge transfer must compete with other decay channels and therefore must be completed within the life-time of the N 1s core hole. Hence, the charge transfer time can be measured relative to the lifetime of the core hole. The resonant channels are populated in the multilayer, since the excited electron cannot transfer from the isolated molecule, this represent the maximum intensity resonant channel. The relative depletion of this channel in the monolayer must therefore be due to coupling with the surface. By comparing the

relative heights of the XAS to the RPES in both the monolayer and multilayer an upper limit for the charge transfer time can be calculated:[26]

$$\tau_{EI} = \tau_{CH} \frac{I^{mono}_{RPES}/I^{mono}_{XAS}}{I^{multi}_{RPES}/I^{multi}_{XAS} - I^{mono}_{RPES}/I^{mono}_{XAS}} \tag{3.1}$$

The I^{mono}_{RPES} and I^{multi}_{RPES} terms represent the intensities of the LUMO+2 and LUMO+3 peaks from the RPES data of the monolayer and multilayer respectively. I^{multi}_{RPES}=0.35 while, I^{mono}_{RPES}=0.13. The constant τ_{CH} is the average lifetime of the N $1s$ core hole which is 6.6fs,[57] hence there is an upper limit to the charge injection time of 6.0±2.5 fs. The charge transfer time for the LUMO+2 and LUMO+3 individually were 6.5±3.5 fs and 6.0±2.0 fs respectively. This compares to upper limits of 4.4 fs for N3 on Au(111),[47] 12 fs on TiO_2,[48] and 3 fs for bi-isonicotinic acid on TiO_2.[30] That charge transfer through the ultra-thin aluminium oxide is possible on very short time scales indicates that this is a viable material for incorporation into DSCs.

3.4 Conclusion

UHV-compatible electrospray deposition (See sec.2.1.6) has been used to deposit N3 onto an ultra-thin aluminium oxide layer on AlNi(100) *in-situ*. Photoelectron spectroscopy was employed to study the bonding geometry of the dye complex on this surface. It was demonstrated that the thiocyanate ligand is not involved in bonding with the surface. One or both of the carboxylic acid groups on one bi-isonicotinic group will de-protonate giving a chemical bond to the surface, with the possible addition of monodentate bonds. The energetic alignment of the system was determined by placing the N $1s$ XAS and valence band photoemission onto a common binding energy scale. This indicated that for the monolayer the LUMO is dragged below the Fermi level, and that charge transfer is possible through the oxide layer and into the substrate. Ultra-thin aluminium oxide layer could be a viable material for DSCs, since it allows the transfer on a time scale of less than 6.0±2.5 fs. Although reduction in recombination effects will not be as significant as for larger aluminium oxide layers, the charge injection from the dye will suffer little suppression and the

passivated surface may lead to more stable devices. The next step for this research is to build an ultra-thin oxide layer on TiO_2 to investigate the charge transfer dynamics.

Chapter 4

Growth of and charge transfer through alumina on titania.

The Atomic Layer Deposition (ALD) of aluminium oxide on titanium oxide in UHV has been studied at regular intervals using synchrotron radiation based photoelectron spectroscopy, indicating a fast initial growth rate of 0.7 nm *per ALD cycle, approximately six times higher than the later growth rate, with non-homogeneous growth throughout. Using resonant photoemission spectroscopy (RPES) and X-ray absorption spectroscopy (XAS) we report on charge transfer from bi-isonicotinic acid through different thicknesses of alumina and into the underlying titania substrate, thus giving important information on the fundamental charge transfer processes which will affect future dye-sensitised solar cell devices. Due the non-homogeneous alumina growth a range of alumina thicknesses were observed after 20 ALD cycles, the surface was categorised into thin (2.8* $\pm$ 0.2 nm*), medium (3.4* $\pm$ 0.2 nm*) and thick (4.0* $\pm$ 0.2 nm*) alumina layers with charge transfer times increasing with alumina thickness which were 25* $\pm$ 4 fs*, 33* $\pm$ 6 fs *and 50* $\pm$ 9 fs *respectively.*

4.1 Introduction

A dye-sensitised solar cell (DSC) consists of a mesoporous TiO_2 electrode with a monolayer of dye chemically anchored to it, an electrolyte comprising redox species and a catalytic counter electrode. One limiting factor of these

cells' operation is the recombination between the photo generated electrons in the porous TiO_2 electrode and either the dye or the electrolyte.[58] Surface passivation using an oxide layer to act as a tunnelling barrier[59] between the redox mediator and conductive electrons has been shown to reduce recombination effects and increase power conversion efficiency,[37, 39, 60] using aluminium oxide has also been shown to increase dye adsorption.[61] However, every additional layer of oxide suppresses forward injection from the dye into the underlying TiO_2[62] and further isolates the dye molecule from the surface reducing the injection rate.[63] Hence there should be an optimal thickness of the oxide layer in order to balance these affects.

By alternating reactants that are exposed to a surface, Atomic Layer Deposition (ALD) can be used to deposit thin films of Aluminium oxide to a specified thickness. The atomic layer deposition of aluminium oxide using trimethylaluminum (TMA) and H_2O is considered to be a model/ideal ALD process since the reactants are very reactive but thermally stable and the by product of the growth, methane, does not interfere with the growth process.[64, 65] The overall equation for the growth of aluminium oxide is represented by:

$$2Al(CH_3)_3(g) + 3H_2O(g) \rightarrow Al_2O_3(s) + 3CH_4(g) + 3H^+ + 3e^- \qquad (4.1)$$

The literature suggests several different values for an optimal oxide thickness in a DSC: 0.12 nm (one ALD layer),[58, 59, 66, 67] 0.2 nm,[68] 0.36 nm (three ALD layers),[62] 2 nm,[60] 12 nm,[61] and 14.1 nm.[39] The majority of the more recent literature is suggesting 1ALD cycle of TMA and H_2O is the optimal thickness with regards to device efficiency, however, the formation of the oxide is reported to be non-homogeneous, this is due to the steric hinderance of the methyl group blocking aluminium from further active sites on the surface, hence one cycle will not be enough to fully passivate the surface.[69] Hence the long term viability and effectiveness of a device will not only depend on the efficiency measured in the lab. In this experiment we have studied the growth of the oxide layer using XPS to look at the growth of alumina on titania in UHV conditions to add more evidence and understanding to the mechanism

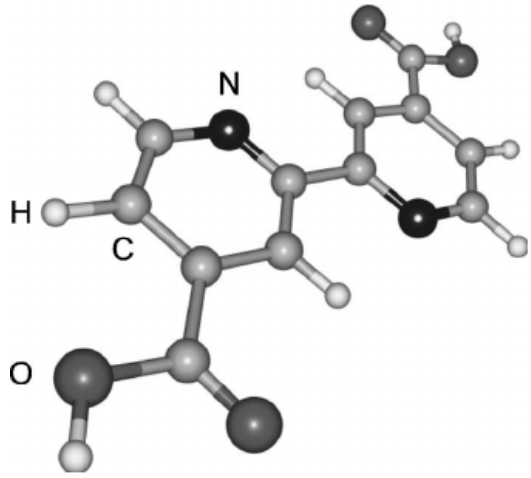

Figure 4.1: Schematic diagram of Bi-isonicotinic acid molecule, (4,4'-dicarboxy-2,2'-bipyridine).

of this 'ideal' ALD process. Since this leads to a significantly non homogenous thickness of alumina on titania, we took the opportunity to study charge transfer times from the same molecule through different thicknesses of oxide, since we have not seen any similar experiment in the literature. The molecule we used is one of the ligands of N3, namely 4,4'-dicarboxy-2,2'-bipyridine (bi-isonicotinic acid). We anticipate this will provide further experimental evidence and attempt to dispel some of the confusion behind the ideal thickness for the alumina layer in DSC applications.

The dye molecule N3 (cis-bis(isothiocyanato) bis (2,2- bipyridyl-4,4'-dicarboxylato)- ruthenium(II)), was unmatched for 8 years as a DSC molecule and as such it has become the benchmark for heterogeneous charge transfer in mesoporous solar cells.[41, 47] However its non-volatile nature makes it difficult to get our required monolayer coverage on different thicknesses of alumina in a UHV environment.[22] Electrospray gives a nonuniform deposition spot[70] and in-situ wet chemistry preparations can be highly complex and can easily lead to contamination,[17]as such both were deemed inappropriate for this experiment. N3 and several organometallic dyes used in dye sensitised solar use the volatile ligand bi-isonicotinic acid, which is easily able to anchor to oxide surfaces and therefore form monolayers under UHV. Since bi-isonicotinic acid is the major ligand of N3 at it provide anchoring to substrates, it can be used

as a model for N3. Therefore understanding the bonding and interaction of this molecule and the alumina coated titania surface should give insight into the critical dye-surface interaction as part of a DSC. We therefore chose this ligand to create a model of part of a oxide passivated DSC. [17, 49, 71, 72]

4.1.1 Background on ALD growth and conditions

Bulk Aluminium oxide is Al_2O_3, however the element ratio is not the same when near to the interface with TiO_2, it is therefore often referred to as AlO_x. [69] The growth mechanism $AlMe_3/H_2O$ process is usually expressed as two half reactions:[69, 73]

$$\| S - OH + Al(CH_3)_3(g) \rightarrow \| S - O - Al(CH_3)_2 + CH_4(g) \tag{4.2}$$

$$\| Al - (CH_3)_2 + 2H_2O(g) \rightarrow \| Al - (OH)_2 + 2CH_4(g) \tag{4.3}$$

Where $\| S$ represents the substrate as either Ti initially or Al on subsequent depositions. TMA is mainly adsorbed onto the OH groups,[74] however our data, presented later in this chapter will clearly show Al adsorption after only TMA dosing too. As part of our experiment we repeatedly dosed the clean $TiO_2(110)$ sample with TMA to find the saturation point. These experiments were conducted in UHV, whereas typical ALD tends to be conducted at higher pressure, however, this has been shown to not make a significant difference to the oxide growth rate.[75] Also, whereas normal ALD is conducted at elevated temperatures, to improve XPS resolution and maintain a constant sample temperature in this experiment the deposition and measurement was conducted at room temperature (RT). This also should not have a significant effect since growth rate is also approximately constant from RT up to 550 K. Only above 550 K does the growth rate start to drop off.[74, 76] Al-C-H and Al-O-H absorption increase with decreasing temperature, but the reaction is thought to not go to completion therefore there is minimal effect on growth rate.[74] RT ALD of alumina does produce highly pure[76] and very smooth[77] samples, the growth rate of which is not significantly affected by the concentration of

reactants.[78] Lengthening the deposition/exposure time does not increase the amount of adsorption, since the available sites become saturated,[74] or inaccessible due to steric hinderance. No major differences were found with the thin films grown with small and large water doses.[79] During normal ALD of aluminium oxide very long H_2O purging times of up to 300 s, can be required to avoid TMA and H_2O combining the gas phase in the chamber and allowing CVD-like deposition and increased growth rate.[74, 76] Since this experiment is in a UHV environment and the pressure recovered between depositions any combination of reactants in the gas phase is negligible. Hence we propose that the differences between our deposition conditions that allows the reaction to be followed using XPS and normal ALD shouldn't have any significant affect on the oxide, and should lead to highly pure samples.

4.2 Experiment

Experiments were carried out at I311 the undulator based VUV and soft X-ray beamline at the MAX-lab Swedish synchrotron radiation facility.[20] The beamline covers photon energies in the range 30 to 1500 eV, with a resolution of 4 meV to 1.4 eV respectively. The end station is equipped with a SCIENTA SES200 (upgraded) electron energy analyser. The radiation has a high degree of elliptical polarisation and may be considered to be linearly polarised. The baseline operating pressure of the analysis chamber was mid 10^{-10} mbar range.

The sample was a square rutile TiO_2 (110) single crystal ($10 \times 10 \times 2$ mm) mounted onto a sample plate using tantrum clips. It was cleaned by repeated cycles of AR^+ sputtering at 2 kV for 5 mins, followed by 1 kV sputtering for 10 mins and then annealed to 800 K via ebeam heating for 20 mins. The sample was assumed clean when C $1s$ and K $2p$ peaks were no longer observed in the XPS. Alumina was deposited by dosing the sample with TMA followed by H_2O, each at 5×10^{-8} mbar for 620 s allowing the pressure to recover to the mid 10^{-9} mbar range between doses. TMA was obtained from Sigma Aldrich packed for use in deposition system with a 25 g in stainless a steel cylinder and leak valve. After twenty complete rounds of TMA and H_2O dosing the sample was annealed to 500 K for 20 mins.

In order to evaporate any physisorbed molecule to create a chemisorbed monolayer of molecules on the surface, bi-isonicotinic acid obtained from Alfa Aesar, was sublimated from a homebuilt K-cell at 470 K, while the sample was held at 480 K at a distance of approximately 30 cm from the K-cell (also see Sec.2.1.6).[17, 80]

All measurements were performed at room temperature. XPS data were calibrated to the TiO_2 $2p_{3/2}$ peak at 458 eV[81, 82] The O $1s$ peak cannot be used for calibration due to the different oxide species in alumina and titania . A Shirley background[28] was removed and the spectra normalised to the photon flux and the number of sweeps, before curve-fit analysis using pseudo-Voigt functions.[54] XAS data were recorded at the N $1s$ adsorption edge. For XAS and RPES the photon energy was calibrated by taking the energy separation of the Al $2p$ core-level photoemission peaks excited by X-rays in first and second order.

4.3 Results and Discussion

4.3.1 Aluminium oxide growth rate

The thickness of the aluminium oxide layer can be calculated from equation 4.4 which uses the attenuation of the underlying $TiO_2(110)$ substrate.

$$d = -\frac{\lambda ln\left(\frac{I}{I_0}\right)}{cos\phi} \tag{4.4}$$

where d is the thickness of the aluminium oxide layer, I integrated intensity of the titanium peaks after deposition, I_0 integrated intensity of the clean titania substrate, ϕ photoelectron emission angle with respect to the surface normal. λ The inelastic mean free path through the aluminium oxide layer is calculated from:

$$\lambda = \sum_{i=1}^{n} k_i E^{P_i} \tag{4.5}$$

n=2 for these fits, k_i and p_i are fitting parameters $k_1 = 23086, p_1 = -1.986, k_2 = 0.1019, p_2 = 0.7726$ for complete description of these parameters

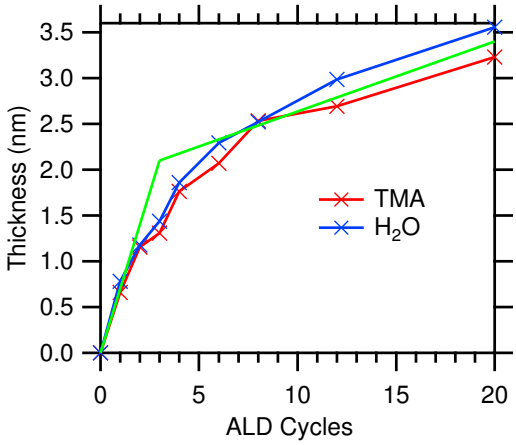

Figure 4.2: Rate of alumina growth over 21 cycles of ALD, green line indicates initial growth rate and constant growth rate similar to that previously seen in the literature after 8 cycles.

see ref[83]. Therefore a mean free path of λ =1.44 nm, for an initial excitation energy of 600 eV is calculated.[83]

Previous experiments showed an average growth rate was 0.12 nm per cycle[67], 0.1-0.2 nm per cycle[66] and 0.11 nm and linear over 800 cycles.[74] In this experiment the growth of alumina was measured using the attenuation of TiO_2 and equations (2) and (3) after 1st, 2nd, 3rd, 4th, 6th, 8th, 12th and 20th TMA and H_2O cycles, each time measuring in three different locations on the sample to calculate the average thickness, the data is presented in Fig.4.2. The initial growth rate for the three cycles is 0.7 nm per cycle, shown by the steeper green line. The growth rate then exponentially decreases until reaching a constant rate at 0.1 nm after the initial eight cycles, the lower gradient part of the green line has a gradient of 0.1 nm indicates the standard growth rate shown in the literature.

The growth of the Aluminium oxide layer is also non uniform. One paper suggest that five ALD cycles or more are required to complete a monolayer and that at less than 0.5 nm the oxide is discontinuous.[64] DFT studies have also shown non uniform growth due to steric hinderance.[69] Our results indicate that the distinct change in growth rate is due to a change in material, initially the Aluminium oxide is growing on TiO_2, the oxide does not grow at

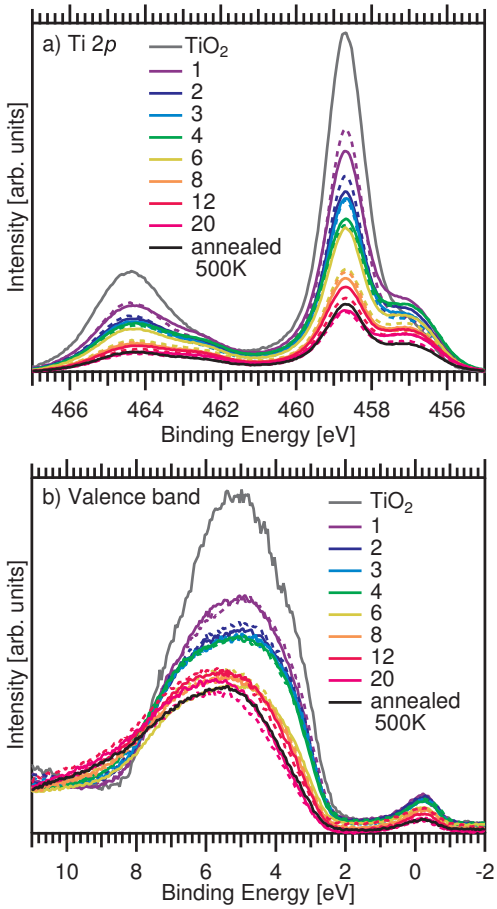

Figure 4.3: Suppression of the TiO_2 (a) and valence band (b) with subsequent cycles of ALD, taken at 600 eV and 50 eV respectively.

one monolayer per cycle due to steric hinderance, the methyl ligand on TMA prevents Al from bonding to every available site. Hence for the first six cycles TMA is still bonding to TiO_2 and shows increased adsorption and higher growth rate. After 8-10 cycles the surface is fully passivated and Al oxide is growing on alumina, which has a different reactivity and therefore different growth rate. Between 5 and 10 cycles there is a transition between the faster initial growth rate and bulk growth rate.

4.3.2 XPS of Aluminium oxide growth

The XPS valence band and Ti $2p$ spectra during alumina growth are shown in Fig.4.3, the sample was measured after the indicated number of complete TMA and H_2O cycles. Since the bulk TiO_2 is not changed the main Ti $2p_{3/2}$ peak was calibrated to 458.7 eV binding energy, during alumina growth both the taller Ti $2p_{3/2}$, and the smaller Ti $2p_{1/2}$ peaks were equally suppressed. However peaks observed at 463 and 457 eV have increased in comparison to the main peaks. These are defect peaks (Ti^{3+})[84] which indicates that defects in the TiO_2 are propagated by the growth of alumina.

The profile of the valence band does not change significantly as more alumina is grown on the surface, data was calibrated to the 22 eV O $2s$ peak, this peak on alumina is at 0.8 eV higher binding energy compared to titania .[85, 86] This would cause the valence band to appear to move to lower binding energy so this does not account for the slight movement of the valence band to higher binding energy as more alumina is deposited. The transition from methyl terminated to hydroxyl terminated surfaces during the H_2O part of the cycle also has negligible impact. The only clear change is the reduction in intensity after each subsequent cycle as the the surface transitions from titania to alumina.

The Al $2p$ data and curve fitting during oxide growth are shown in Fig.4.4. As more alumina is deposited, the peak clearly grows and shifts to higher binding energy relative to the Ti $2p$ peak. The interfacial peak is initially at 74.2 eV, and after 20 cycles it is at 74.7 eV. After twenty cycles the peak position is comparable to bulk alumina peak is between 73.85 and 75.0 eV.[84, 87, 88] Once a dose of H_2O is added the peak seems to adopt a near constant position of 74.3±0.1 eV (with the exception of after the eight an twenty cycles then it is 0.2 eV higher.) This is due to the switch from a mostly methyl terminated surface to mostly hydroxyl terminated after water dosing, as described in Sec.4.1.1.

The change in the O $1s$ peak during alumina growth is shown in Fig.4.5. As shown in the fit during alumina growth there is a consistent decrease in a peak 530.2 eV and growth of another peak at 531.2 eV. Clean TiO_2 has a major peak at 530.2 eV, with a very small shoulder peak at 531.5 eV which is

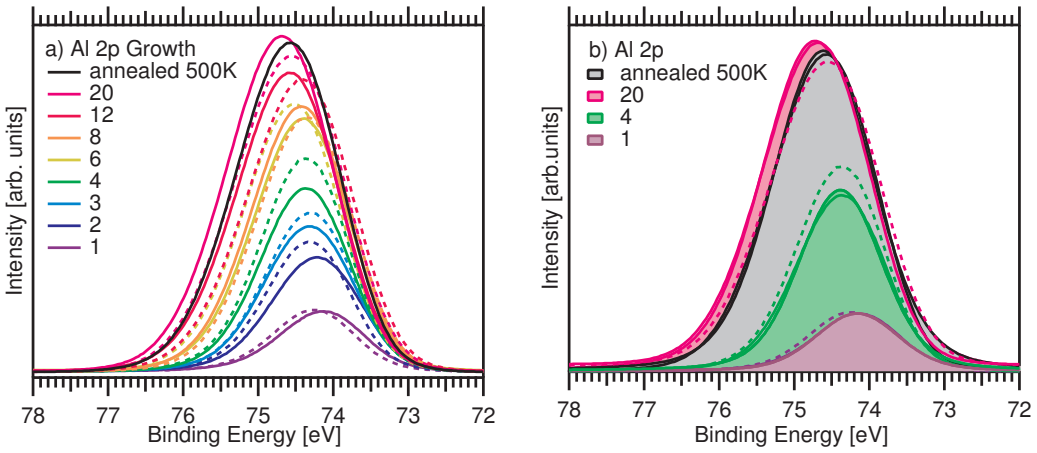

Figure 4.4: Shift in the Al $2p$ XPS peak from 74.2 to 74.7 eV during the alumina growth, b) sample of the Gaussian fits. Solid line are the data taken after TMA while dashed line of the same colour is after the subsequent H_2O dose.

an intrinsic[89] or OH peak.[90] As alumina grows the oxygen species at the surface are converted from Ti-O species to Al-O. Alumina O $1s$ peak is at 531.2 eV, intermediate spectra are just a combination of these peaks with no change to the fit parameters. The lack of additional peaks would indicate that there is no significantly different O $1s$ environment at the interface between alumina and titania.

The C $1s$ XPS data during oxide layer growth is shown in Fig.4.6, prior to deposition there was no visible C $1s$ peak, the peak undergoes significant shifts throughout the oxide growth. After the initial TMA dosing a peak formed at 283.2 eV which is due to the methyl groups, and a shoulder peak at 284.7 eV. After H_2O dosing the methyl peak has been greatly reduced in intensity and shifted up in binding energy by 0.5 eV as the methyl groups are substituted for a hydroxyl group during water dosing. While the shoulder peak has risen, there is also an additional small peak at 286.0 eV. As more TMA cycles are adsorbed the main peak shifts in binding energy to 283.7 eV, the shoulder and satellite peak remain in the same position. However after H_2O dosing between the fifth and twentieth dose there is no change in peak position, only the intensity of the main peak has increased. After annealing most of the methyl groups are removed,[91] with the intensity of the C $1s$ peak now being similar

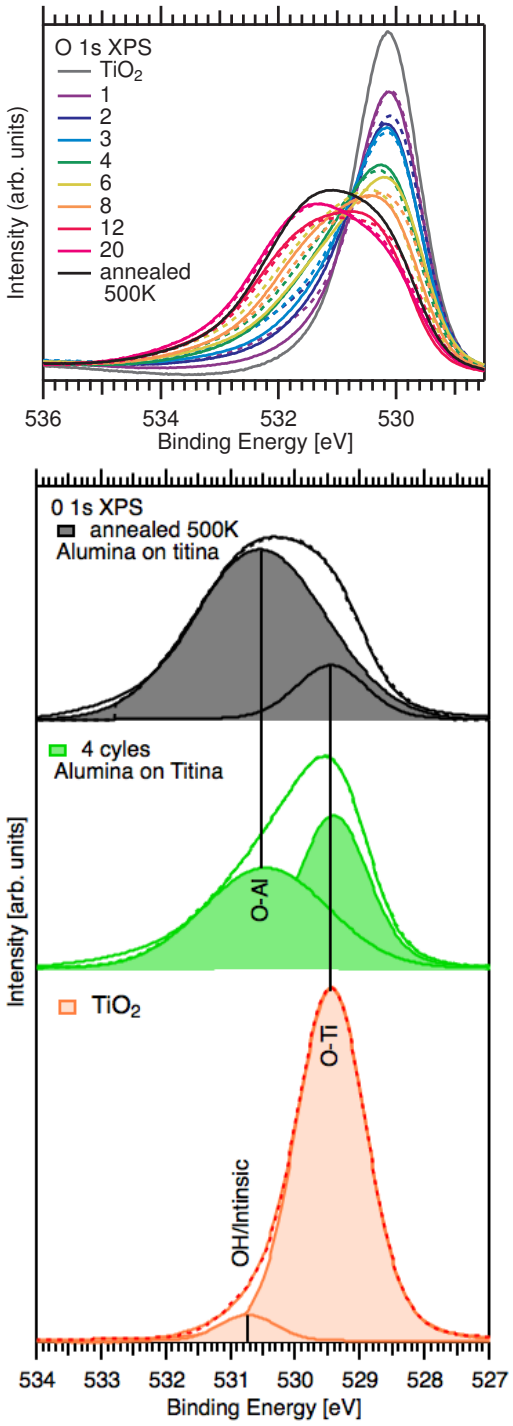

Figure 4.5: O 1*s* XPS a) during alumina growth, b) fits indicate two clear species, Ti-O and Al-O at 530.1 eV and 531.2 eV respectively.

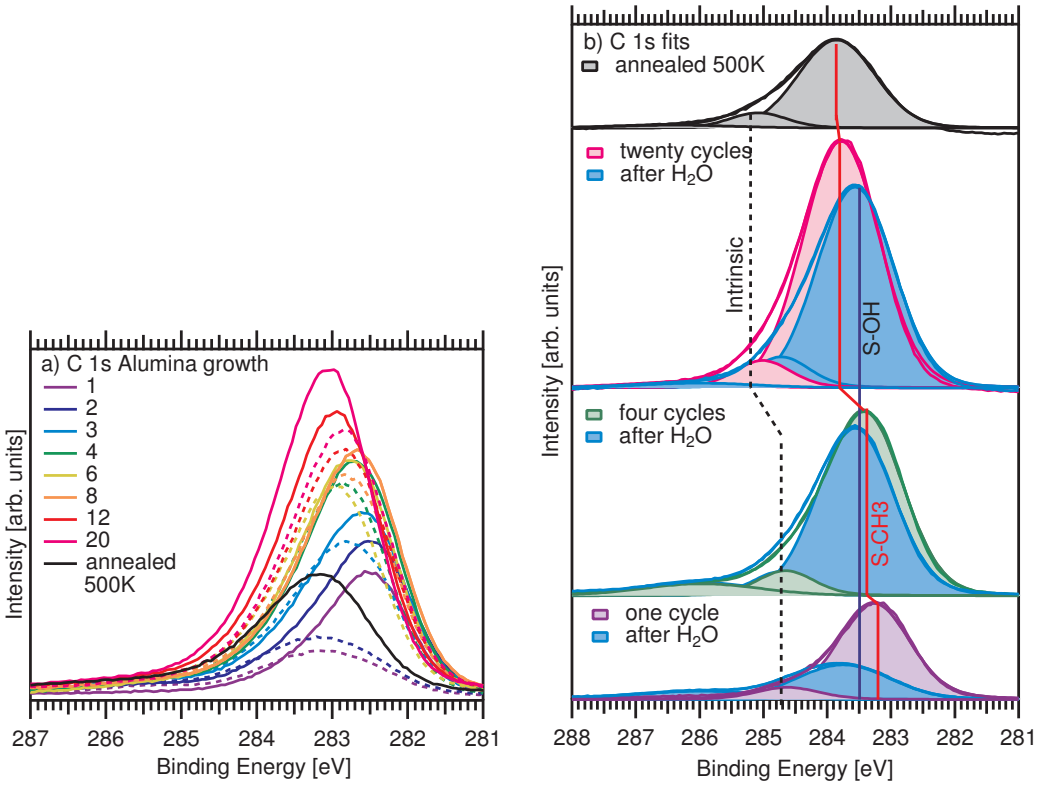

Figure 4.6: Shift in the C 1*s* XPS peaks during the Al oxide growth, showing the first (purple), four (green), twentieth (pink), completed TMA dosing and after twenty completed rounds and annealed to 500K for 20 mins (black), the corresponding subsequent H_2O dose is also shown (blue). Red line indicate shift on the main peak after TMA dosing, while blue line shows the persistent position of the peak after H_2O dosing.

to the first TMA cycle. The increase in carbon peak size maybe due to an increased adsorption of methyl group on the alumina oxide in preference to titania and increased surface contamination with carbon.

4.3.3 Bi-isonicotinic acid on alumina on titania.

The XPS data for bi-isonicotinic acid mono and multilayers are shown in the following Figures, with the exception of density of states plots Fig.4.9, all spectra have been normalised to the ring current, in order to compare relative intensities of the species.

The O 1s peaks of molecule isolated from the surface in the multilayer bi-isonicotinic acid are shown in Fig.4.7, two peaks with approximately the same area one at 531.1 eV with another 1.26 eV higher, this is a close agreement with previous data.[17, 92] The shift betweens these two bi-isonicotinic acid peaks is due the presence of the proton on the carboxylic acid group and therefore two different O 1s environments. Both bi-isonicotinic acid peaks are also seen in the monolayer, with a significant decrease in the C-OH peak such that there is a 3:1 ratio between C=O:C-OH indicating de-protonation of only one carboxylic acid group. This is clearly different to clean TiO_2 where both carboxylic acid groups de-protonate,[71] and is similar to the range of bonding geometries seen with N3 on an ultra-thin alumina oxide seen in Chap.4.[70] This might explain the increased adsorption seen on alumina compared to titania as if only one carboxylic acid group deprotonates there is less steric hinderance and therefore increased adsorption.

The C 1s peaks of the bi-isonicotinic acid multilayer, monolayer and clean substrate are shown in Fig.4.8, the multilayer spectra indicate two clear species, the larger peak at 285.0 eV is due to the pyridine ring, while the smaller at 288.5 eV is due to the carboxyl group. From the multilayer to the monolayer the main peak has shifted 0.25 eV higher, while the carboxyl group is 0.5 eV higher. The monolayer data is very similar to bi-isonicotinic acid on the clean TiO_2 surface.[71] A similar shift in the main peak has previously been observed on Au(111)[49], however the larger carboxyl shift has not previously been observed and maybe due to larger amount of charge transfer to the surface

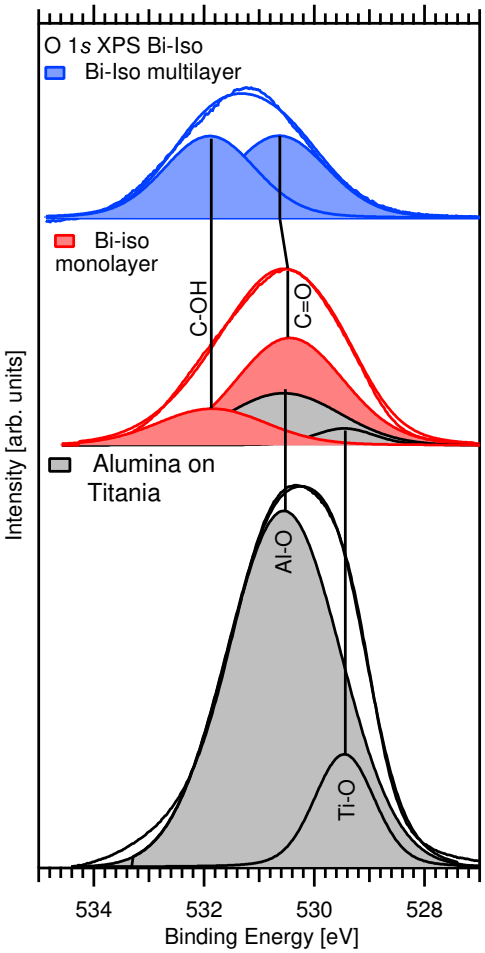

Figure 4.7: O 1s of alumina on titania substrate shown in black, isolated bi-isonicotinic acid two peak O 1s in blue, and monolayer bi-isonicotinic acid on alumina on titania shown in red.

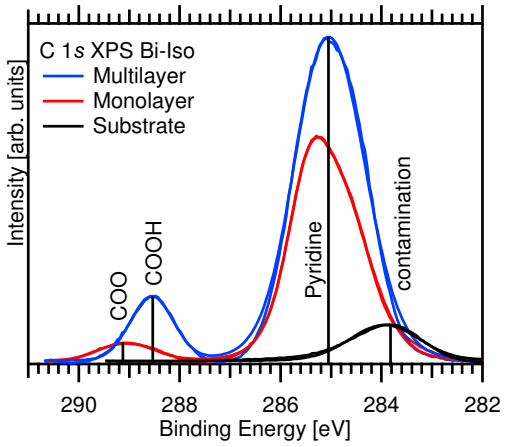

Figure 4.8: C 1s of alumina on titania substrate shown in black, isolated bi-isonicotinic acid two peak O 1s in blue, and monolayer bi-isonicotinic acid on alumina on titania shown in red.

during bonding.

The density of states for multilayer and monolayer are shown in Fig.4.9 and were complied through methodology discussed in Sec.2.2.3.[29] N 1s XAS shows an intense LUMO peak, with a LUMO+1 3.7 eV higher, this is similar to data shown in.[17, 71] The LUMO peak at 398.3 eV photon energy is attributed to a π^* antibonding orbital, while the broader features are σ^* antibonding orbital resonances of the pyridine rings.[92] Other density of states have seen a LUMO+1 peak at -2eV binding energy [17, 93] this feature is removed when the surface is prepared hot. The valence band for the monolayer is similar to the surface with the addition of a broad state at 9.3 eV, which corresponds with the HOMO-1 in the multilayer. The band gaps of the alumina and titania layers are drawn on as a guide, their locations are taken from Refs.[46]and [94] respectively and positioned relative to the Fermi edge.

The N 1s XPS of bi-isonicotinic acid multilayer and monolayer is shown in Fig.4.10, for the bi-isonicotinic acid multilayer it is very broad due to disordered hydrogen bonding between the isolated molecules. Previously for N 1s bi-isonicotinic acid monolayers on TiO_2[80] there was a shakeup peak seen at 402 eV, here on alumina the spectra are completely flat in this region, there is however a small shoulder in the monolayer at 400.2 eV.

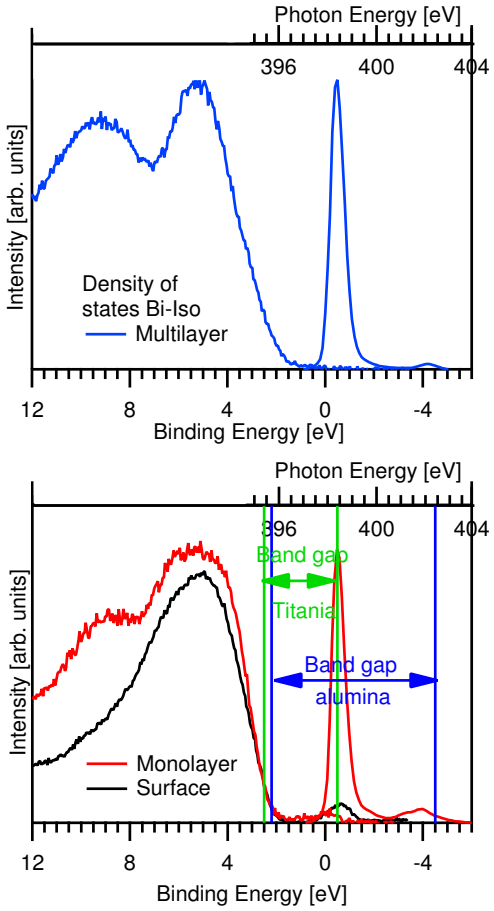

Figure 4.9: Density of states plots of bi-isonicotinic acid isolated from the surface two peak in (blue), monolayer bi-isonicotinic acid on alumina on titania shown (red) and the alumina on titania surface (black).

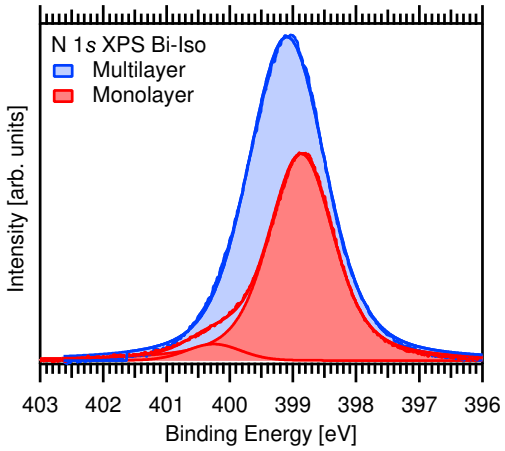

Figure 4.10: bi-isonicotinic acid on alumina on titania , XPS isolated bi-isonicotinic acidtwo peak in (blue), monolayer bi-isonicotinic acid on alumina on titania shown (red).

4.3.4 Charge transfer dynamics and core hole clock

After twenty cycles of ALD there were still significant differences in the thickness of alumina across the sample due the random nature of the growth.[69] Hence data sets were taken at multiple points and sorted into three categories of aluminium oxide thickness by comparing the suppression of the Ti $2p$ peak and the growth of the Al $2p$ peak see Fig.4.11. Some data had to be excluded since they did not fit either category consistently across both Ti and Al, this may have been due to either inconsistent growth across the sampled region for example island growth or gaps in the bi-isonicotinic acid monolayer. Since the bi-isonicotinic acid monolayer was deemed to suppress the underlying TiO_2 surface by a factor of four hence this was applied to the Equ.4.4 to calculate the alumina thicknesses as thin 2.8 ± 0.2 nm, medium 3.4 ± 0.2 nm and thick 4.0 ± 0.2 nm.

Separate RPES datasets were calibrated in intensity by the synchrotron ring current, the images were aligned in binding energy and photon energy. The photon energy was calibrated to the energy separation of the Al $2p$ core-level photoemission peaks excited by X-rays in first and second order respectively. The images of different alumina thicknesses were combined to form three composite RPES for each category Fig.4.12. A broadening of the oc-

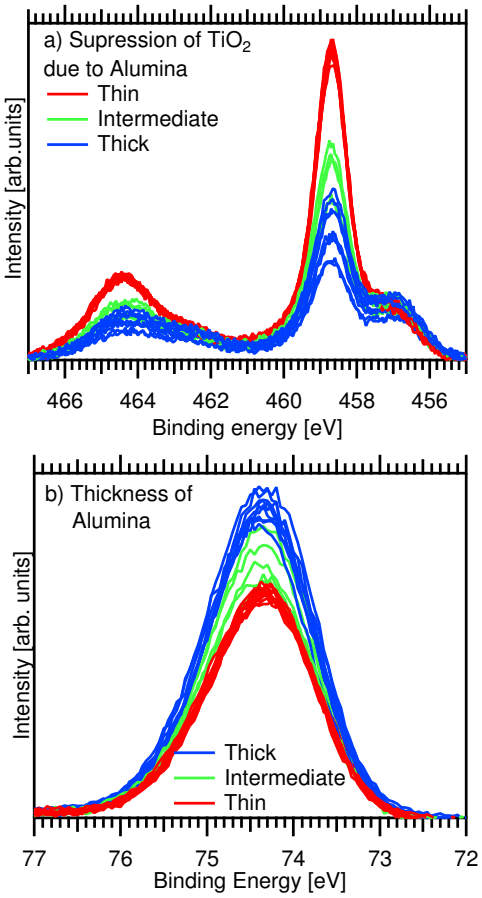

Figure 4.11: Aluminium oxide thickness a) the suppression of TiO_2 due to b) increased alumina coverage. Thick alumina (blue), intermediate (green) and thin (red).

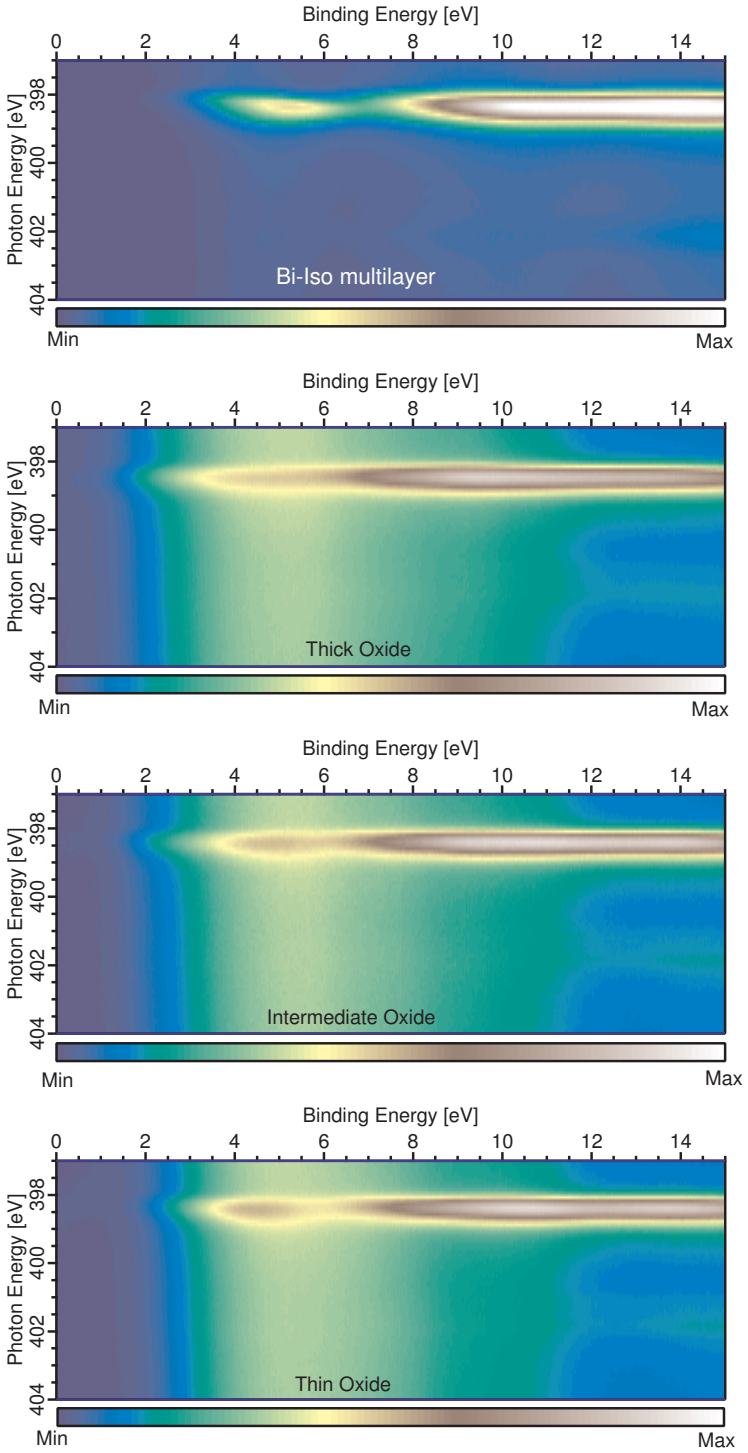

Figure 4.12: RPES data of molecules isolated from the surface in the multilayer and monolayer on three categorised thicknesses of alumina.

cupied states is shown as an increasing width to the vertical green feature on the RPES images as the thickness of the alumina increases. Also there is more enhancement of the HOMO at the LUMO excitation energy on the thinner alumina coatings. This data was integrated over the 0-8 eV range and 12-16 eV range to form the RPES and XAS respectively, in order to form the plots necessary for core-hole-clock analysis.

This integrated data is shown in Fig.4.13, the LUMO is labelled A, in the multilayer the LUMO+1 is B, in the monolayer data there is another unoccupied state in between these labelled C on the thick oxide, monolayer investigations of bi-isonicotinic acid on TiO_2 have also seen a peak lying close to 400 eV. [17, 80] Theoretical calculations attribute this as a consequence of bonding to the TiO_2 surface and possible damaged to the molecule breaking the link between bi-isonicotinic to form two bi-isonicotinic acid molecules. [17, 92, 93]. Qualitatively there is a clear change in the shape of the peak B when bonded to the surface, instead of a single peak in the LUMO+1 for the multilayer the same peak in the monolayer clearly comprises three separate peaks B, B' and B", implying additional orbitals available after bonding to the surface. In order to get a good comparison with the isolated molecules only the main central peak (B) was used for the core-hole-clock calculation.

In principle, a charge transfer time for electron transfer out of a particular unoccupied molecular orbital can be calculated using equation 5.1,

$$\tau_{EI} = \tau_{CH} \frac{I^{mono}_{RPES}/I^{mono}_{XAS}}{I^{multi}_{RPES}/I^{multi}_{XAS} - I^{mono}_{RPES}/I^{mono}_{XAS}} \tag{4.6}$$

where the $I^{mono}_{RPES}/I^{mono}_{XAS}$ terms represent the relative intensities of the participator channel in the RPES as a fraction of the total x-ray absorption for the relevant molecular orbital given by the XAS. The $I^{multi}_{RPES}/I^{multi}_{XAS}$ term represents the fraction of participator electrons that would be expected in the absence of charge transfer as determined from the decoupled molecules in the multilayer film. The lifetime of the C $1s$ core-hole is given by τ_{CH} and is approximately 6.6 fs.[95] For a complete discussion of the core-hole clock implementation of RPES, including derivation of this equation, we direct the reader to Brühwiler et al.[26]

The calculation showed that charge transfer times from bi-isonicotinic acid through the oxide and into TiO_2 increased with increasing alumina thickness, thin (2.8 ± 0.2 nm) 25±4 fs, medium (3.4 ± 0.2 nm) 33±6 fs, and thick (4.0 ± 0.2 nm) 50±9 fs. These charge transfer time are long in comparison to 2.8±1.5 fs for bi-isonicotinic acid on TiO_2,[96] and 6.0±2.5 fs from N3 through 2 atomic layers alumina coating on NiAl(110), see Chap.4.[70] This demonstrates that dye molecules are very quickly becoming isolated electronically from the underlying titania conduction band after only a few cycles of ALD.

4.4 Conclusion

ALD using TMA and H_2O has been used to create a thin layer of alumina on titania in UHV, the sample was analysed via synchrotron radiation based photoelectron spectroscopy at regular intervals during the alumina growth. We have shown a faster than previously though initial growth rate of 0.7 nm per cycle, in comparison to 0.1 nm per cycle during bulk growth. bi-isonicotinic acidbonds to the surface via de-protonation of the carboxylic acid, the singlet LUMO also changes to a triplet during bonding. The random nature of alumina growth lead to a range of thickness, resonant photo emission spectroscopy was used to measure the charge transfer time through thin (2.8 ± 0.2 nm), medium (3.4 ± 0.2 nm) and thick (4.0 ± 0.2 nm) alumina and into the underlying titania these were thin 25±4 fs, medium 33±6 fs, and thick 50±9 fs.

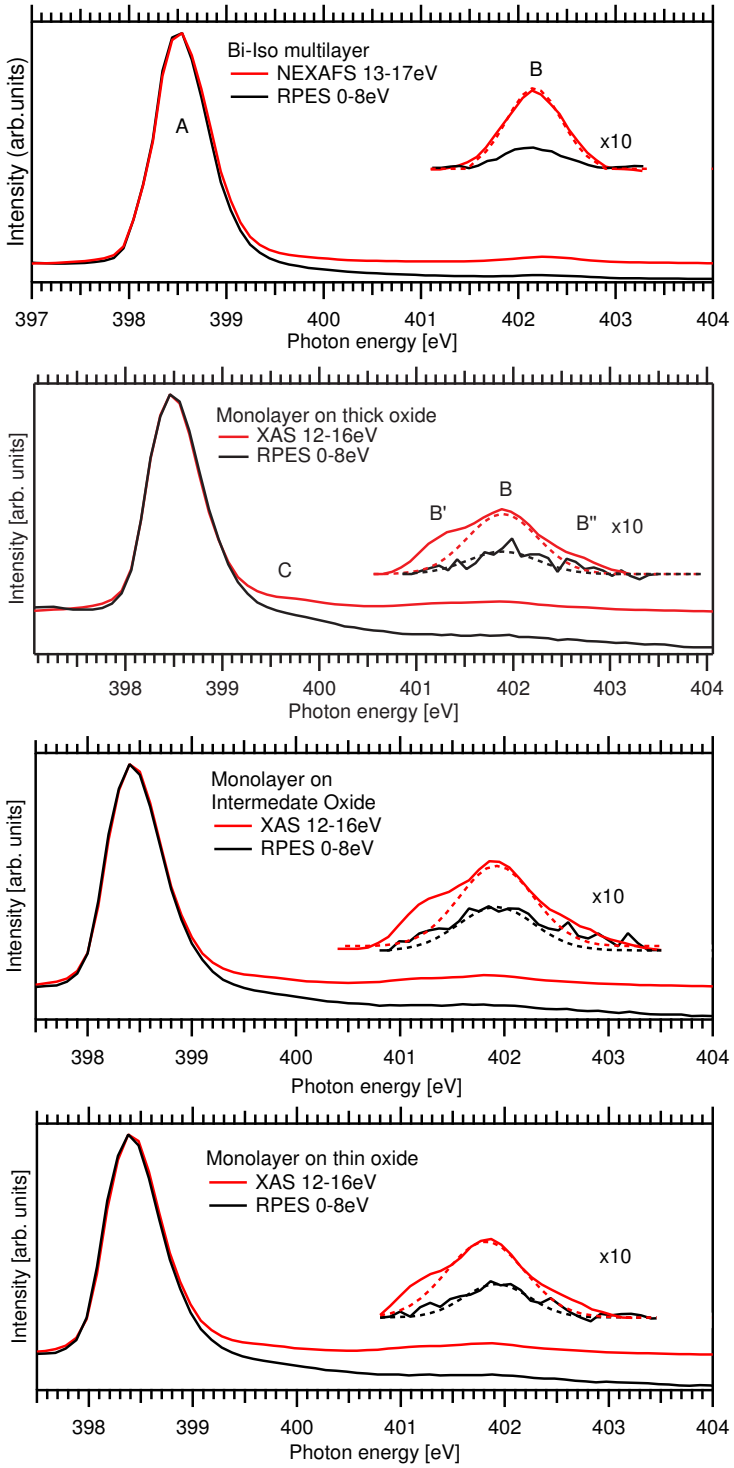

Figure 4.13: C 1s XAS and RPES data obtained by integrating of the indicated regions of Fig.4.12 in order to perform Core-hole-clock analysis.

Chapter 5

Charge transfer interaction between C_{60} and metal surfaces

Charge transfer interactions between C_{60} and the metal surfaces of Ag(111), Cu(111), Au(111) and Pt(111) have been studied using synchrotron-based photoemission, resonant photoemission and X-ray absorption spectroscopies. By placing the X-ray absorption and valence band spectra on a common binding energy scale, the energetic overlap of the unoccupied molecular orbitals with the density of states of the underlying metal surface have been assessed in the context of possible charge transfer pathways. Resonant photoemission and resonant Auger data, measuring the valence region as a function of photon energy for C_{60} adsorbed on Au(111) reveals three constant high kinetic energy features associated with Auger-like core-hole decay involving an electron transferred from the surface to the LUMO of the molecule and electrons from the three highest occupied molecular orbitals, respectively and in the presence of ultra-fast charge transfer of the originally photoexcited molecule to the surface. Data for the C_{60}/Ag(111) surface reveals an additional Auger-like feature arising from a core-hole decay process involving more than one electron transferred from the surface into the LUMO. An analysis of the relative abundance of these core-hole decay channels estimates that on average 2.4 ± 0.3 electrons are transferred from the Ag(111) surface into the LUMO. A core-hole clock analysis has also been applied to assess the charge transfer coupling in the other direction, from the molecule to the Au(111) and Ag(111) surfaces.

Resonant photoemission and resonant Auger data for C_{60} molecules adsorbed on the Pt(111) and Cu(111) surfaces are shown to exhibit no super-Auger features, which is attributed to the strong modification of the unoccupied molecular orbitals arising from stronger chemical coupling of the molecule to the surface.

5.1 Introduction

Molecule-molecule and molecule-surface charge transfer interactions lie at the heart of many molecular electronics applications, in particular organic solar cells where the molecular components act as both electron donors and acceptors. Fullerenes are excellent electron acceptors for molecular electronics in general and molecular photovoltaic devices in particular.[97] Over the past two decades the majority of organic photovoltaics have focused on an approach using conjugated, semiconducting polymer electron donors (such as P3HT) with fullerene-based acceptors (such as PCBM).[98, 99]

In our previous studies of organic molecules on metal surfaces using resonant photoemission and resonant Auger spectroscopies, the transfer of electrons from a Au(111) surface into the lowest unoccupied molecular orbital (LUMO) of the molecule was shown to give rise to a new core-hole decay channel directly involving the transferred electron.[17, 18] The resulting core-hole decay process was suggested as one in which the photoexcited core-electron is localised in an unoccupied molecular orbital on the timescale of the core-hole lifetime and spectates as the electron transferred from the surface into the LUMO fills the core-hole with the energy being liberated by the emission of an electron from the highest occupied molecular orbital (HOMO). The kinetic energy of an electron emitted in such a Core/LUMO/HOMO decay process is greater than that of a normal Core/HOMO/HOMO spectator decay by an amount equal to the HOMO-LUMO gap of the molecule, and thus referred to as *superspectator* decay. The presence of these high and constant kinetic energy features in resonant photoemission spectroscopy (RPES) can therefore provide direct evidence for charge transfer into the LUMO of the molecule. This was first observed in the case of bi-isonicotinic acid (4,4'-dicarboxy-2,2'-bipyridine) molecules adsorbed on a Au(111) surface,[17] and later for a C_{60} monolayer on

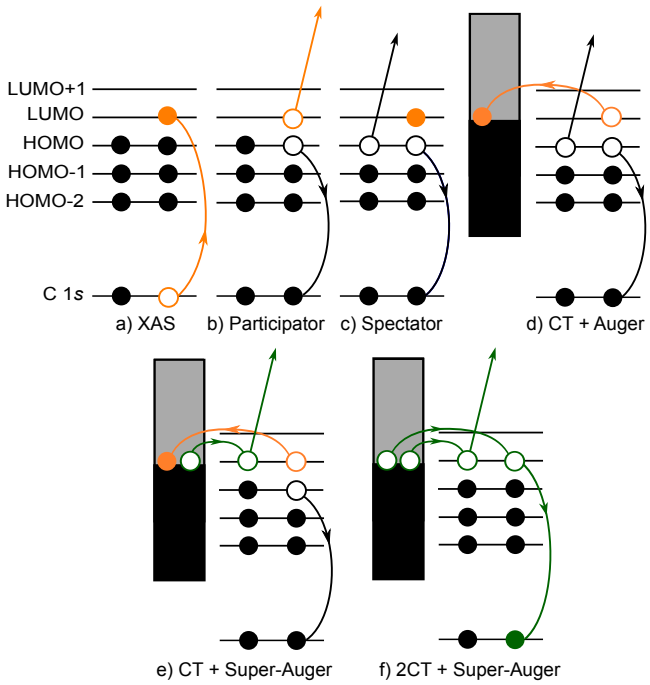

Figure 5.1: Schematic illustration of the key electron excitation and subsequent core-hole decay processes observed for a molecule adsorbed on a metallic surface and relevant charge transfer interactions. (a) XAS excitation of a core-level electron (orange) into an unoccupied molecular orbital, in this case the LUMO; (b) participator decay; (c) spectator decay; and (d) charge transfer of the photoexcited electron to the substrate conduction band followed by Auger decay (black and grey shaded areas represent occupied and unoccupied states of the surface respectively), (e) charge transfer of an electron (green) from the substrate valence band into the LUMO of the molecule, followed by ultra-fast charge transfer of the originally photoexcited electron into the substrate conduction band and subsequent super-Auger decay involving the electron (green) transferred from the surface, and (f) charge transfer of two electrons (green) from the substrate valence band into the LUMO of the molecule, followed by super-Auger decay involving the electrons (green) transferred from the surface (ultra-fast charge transfer of the originally excited electron assumed to take place but omitted for clarity).

Au(111).[18] In both cases, the high kinetic energy Auger-like features are not observed for molecules isolated from the surface of the substrate in a multilayer, or for the clean surface itself confirming that the core-hole decay process arises directly from the molecule-surface interaction. Similar high kinetic energy features have also been observed in a recent RPES study of bipyridine monolayers adsorbed on Au(111), epitaxial graphene on Ni(111) and graphene nanoribbons, attributed to ultra-fast bidirectional charge transfer between the molecules and the surface.[100]

The mechanisms for the different non-radiative core-hole decay channels available to a molecule coupled to a metal surface are schematically illustrated in Fig. 5.1. X-ray absorption (XAS) causes excitation of a core-level electron (orange) - in this case the C 1s orbital - to an unoccupied molecular orbital (Fig. 5.1a) after which the resulting core-hole must be filled by a higher-lying electron. In the case of *participator* decay (Fig. 5.1b) the originally excited electron is a direct participant in the decay process and the system is left in a final state identical to direct photoemission of the valence state involved. Participator decay therefore results in a resonant enhancement of the photoemission (RPES) and will have a constant binding energy as the photon energy increases. In the case of *spectator* decay (Fig. 5.1c) the originally excited electron is not a direct participant in the transition and the system is left in a two-hole final state via an Auger-like Core/HOMO/HOMO decay process. The kinetic energy of a spectator electron is therefore constant and lower than that of a participator electron by at least the HOMO-LUMO separation. Alternatively, if the originally excited electron is not localised on the molecule on the timescale of the core-hole lifetime (through tunnelling into the empty states in the underlying substrate or through excitation above the ionisation threshold) the core-hole will decay via a *normal Auger* process (Fig. 5.1d). Auger electrons also have a constant kinetic energy, which is lower that of the spectator process due to the presence in the latter of the additional electron in final state (the so called spectator shift). In this chapter the case in which an electron has been transferred from the metal surface into the LUMO of the molecule is considered, whereupon that electron is available to participate in the core-hole decay resulting either in a *superspectator* decay if the orig-

inally excited electron is localised on the timescale of the core-hole lifetime, or *super-Auger* decay if not ((Fig. 5.1e). In both cases the kinetic energies of the emitted electrons are increased by the fact that one of the participating electrons originates from the LUMO rather than the HOMO, resulting in an energetic uplift corresponding to the HOMO-LUMO separation. If two electrons were to transfer into the LUMO (Fig. 5.1f) this would open up an additional a Core/LUMO/LUMO decay process, allowing additional energy to be transferred to the emitted electron since now both electrons involved in the transition originate from the LUMO. By considering the energies of the electrons measured in RPES as a function of photon energy over the C $1s$ absorption edge in this this chapter the data is interpreted in terms of these available core-hole decay processes and infer from these the charge transfer processes and dynamics at the C_{60}/metal surface. As superspectator and super-Auger processes rely on the transfer of electrons from the surface into the LUMO of the molecule, by tuning the coupling strength of the molecule, in this case C_{60} with the metal surface it is in principle possible to observe differences in the intensity of these channels in the RPES. Previous studies have found varying amounts of charge transfer between different metal surfaces and adsorbed C_{60} molecules,[101–108] and in this chapter the effect that changes in the adsorption interaction have on the presence of high constant kinetic energy core-hole decay features for C_{60} molecules adsorbed at Au(111), Ag(111), Cu(111) and Pt(111) surfaces is explored.

5.2 Experiment

Experiments were carried out at the I311 beamline on the MAX-II storage ring at the MAX-lab facility in Lund, Sweden. The beamline covered a photon energy range of 30-1500 eV with a resolution of 4 meV-1.4 eV respectively. The spot size was 0.5 mm horizontally and 0.1 mm vertically. The end-station was equipped with a *Scienta* SES200 hemispherical electron analyser. The radiation had a high degree of elliptical polarisation, and is considered as linearly polarised, further details of I311 can be found elsewhere.[20] The base pressure in the analysis chamber was in the low 10^{-10}mbar range and in the

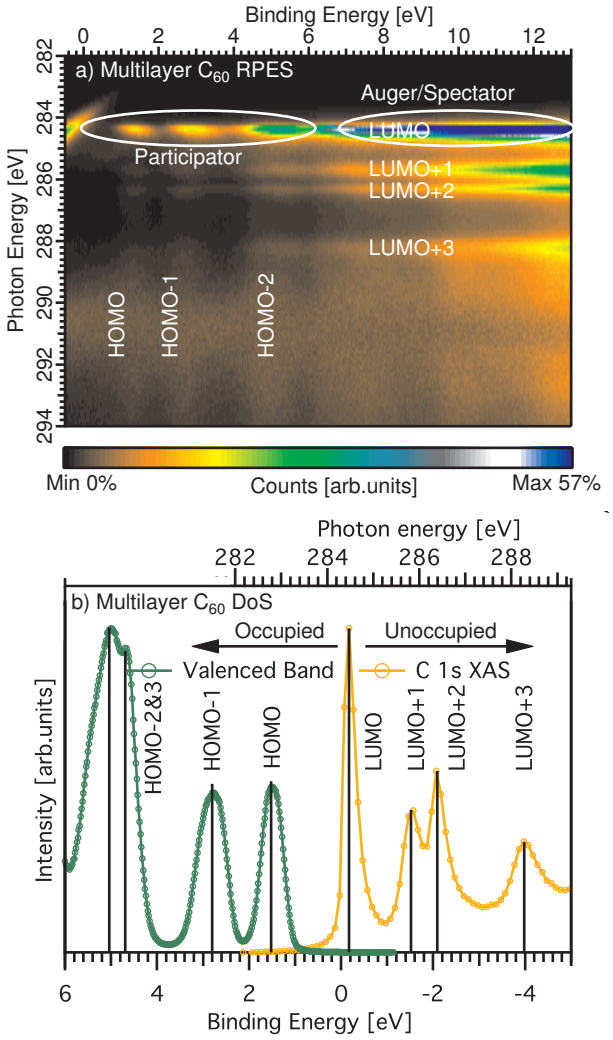

Figure 5.2: a) RPES for a C_{60} multilayer obtained by measuring the valence photoemission whilst incrementally increasing the photon energy over the C 1s absorption edge, and b) a density of states plot for multilayer of C_{60} obtained by placing the C 1s XAS on a common binding energy scale with the valence band photoemission (hν = 60 eV).

preparation chamber the mid 10^{-10}mbar region. The metal substrates were all circular single crystals mounted to loops of tungsten wire to provide resistive heating. Thermocouples were mounted directly to each crystal.

The Cu(111) single crystal was cleaned with 2 kV Ar^+ ion sputtering for 20 mins, followed by annealing at 470 °C for 20 mins. The Au(111) and Ag(111) single crystals were cleaned in a similar manner, but with annealing temperatures of 600 °C and 550 °C, respectively. The Pt(111) single crystal was cleaned with 2 kV Ar^+ ion sputtering for 20 mins, followed by annealing in O_2 at 10^{-7}mbar for 10 mins at 670 °C, followed by a flash anneal to 800 °C in UHV.[104] For all crystals sputtering and annealing cycles were repeated until C 1s and O 1s peaks were no longer observable by x-ray photoemission spectroscopy (XPS), and the metal core-level spectra exhibited the characteristic metallic line shapes. All XPS was measured at normal emission while RPES and XAS were measured at normal incidence in order to increase surface sensitivity and thus minimize the contribution of direct photoemission of the substrate valence band.

A multilayer of C_{60} was thermally evaporated from a Knudsen-type cell at approximately ∼360 °C for 20 mins. The samples were located at a distance of approximately 20 cm and held at room temperature. Following multilayer deposition the substrate photoemission peaks were completely suppressed and the characteristic shake-up structure and symmetric main peak observed in the C 1s spectrum.[109] C_{60} monolayers were prepared by heating the samples to 300 °C for 10 mins to desorb the physisorbed multilayers, leaving only the more strongly bound/chemisorbed C_{60} monolayer. The presence of a monolayer was confirmed by the emergence of the characteristic asymmetry of the C 1s peak and modification of the shake-up features.[110, 111]

For resonant photoemission spectroscopy (RPES) and x-ray absorption spectroscopy (XAS) measurements the beamline was set such that the photon energy resolution was 50 meV for photons of 340 eV. A taper of 3 mm was applied to the undulator to reduce the intensity variation of the radiation over the photon energy range of the measurement. The analyser was set to record spectra in fixed mode with an energy resolution of 200 meV, in order to give the best compromise between signal and resolution. The photon energy scale

for the RPES data was calibrated to the kinetic energy difference of the C 1s photoemission peak measured with first and second order x-rays. The binding energy scale of the RPES and all photoemission data was calibrated to the Fermi level of the metal. XAS and RPES data were divided through by the XAS spectra of the clean surface in order to account for variations in flux as a function of photon energy. It should be noted that the 'carbon dip'[20] arising from surface contamination of the beamline optics meant that close to 291 eV photon energy the photon counts are effectively zero, resulting in a narrow band of lost information observed in the RPES data sets. To enhance the weaker features of interest in the RPES data the intensity scales have been clipped to the indicated range.

5.3 Results

5.3.1 C_{60} multilayer

The C 1s RPES data for a C_{60} multilayer is shown in Fig. 5.2a. When the excitation photon energy matches the LUMO resonance (284.2 eV) there is intense absorption and subsequent non-radiative core-hole decay. Three bright features can be observed in the RPES at this photon energy, centred around binding energies of 1.5, 3 and 5 eV, which correspond to the binding energies of the HOMO, HOMO-1 and HOMO-2,3 respectively. These features are attributed to a resonant enhancement of the photoemission of the relevant occupied molecular orbitals due to participator decay involving the originally photoexcited electron localised in the LUMO on the timescale of the core-hole lifetime. Above a binding energy of around 6 eV an intense band of electrons attributed to spectator and Auger decay (see Fig. 5.1) is observed. As the photon energy is increased over the LUMO+1,+2 and +3 resonances the constant kinetic energy spectator and Auger features drift out of the binding energy window to higher binding energy. Although weaker than for the LUMO, participator enhancements of the HOMOs are also observed for all three of the higher lying resonances (the reduced intensity is due to matrix element effects arising from the different orbital overlaps). The diagonal line in the upper

left corner is due to the C 1s core-level excited by second order x-rays from the monochromator, this features is clear prior to photon energy normalisation however is now only partially visible at the C 1s edge. Fig. 5.2b shows the density of states for multilayer C_{60} molecules constructed by placing the valence band (occupied molecular orbitals) and C 1s XAS (unoccupied molecular orbitals) on a common binding energy scale, using procedures described elsewhere.[29]

5.3.2 C_{60}/Au(111) monolayer

The C 1s RPES data for a C_{60} monolayer adsorbed on the Au(111) surface is shown in Fig. 5.3a. At the LUMO resonance around 284 eV photon energy three enhancements are observed at the binding energies of the HOMO, HOMO-1 and HOMO-2,3 similar to the multilayer data. These features are again attributed to the same participator decay process that gives rise to these features for the multilayer. Electrons excited from the C 1s core level into the LUMO are able to participate in the core-hole decay due to being localised in that orbital on the timescale of the core-hole lifetime. Fig. 5.3b shows the valence band photoemission and C 1s XAS placed on a common binding energy scale to determine how the unoccupied molecular orbitals of the core-excited C_{60} monolayer overlap with the filled and empty densities of states in the Au(111) surface. The LUMO is located just below the Fermi level and therefore overlaps with filled states in the surface into which charge transfer from the molecule will be forbidden. These localised core-excited electrons can also play the role of a spectator in the decay process resulting in an Auger-like Core/Valence/Valence transition (see Fig. 5.1c) that together with normal Auger decay gives rise to a broad constant kinetic energy feature on the high binding energy side of the data.

Three distinct constant kinetic energy features can also be observed in the RPES as diagonal lines that track back to the participator signals at the HOMO, HOMO-1 and HOMO-2 binding energies at the LUMO resonance. These features are attributed to a Auger-like decay process in which an electron has been transferred from the surface into the LUMO of the molecule.

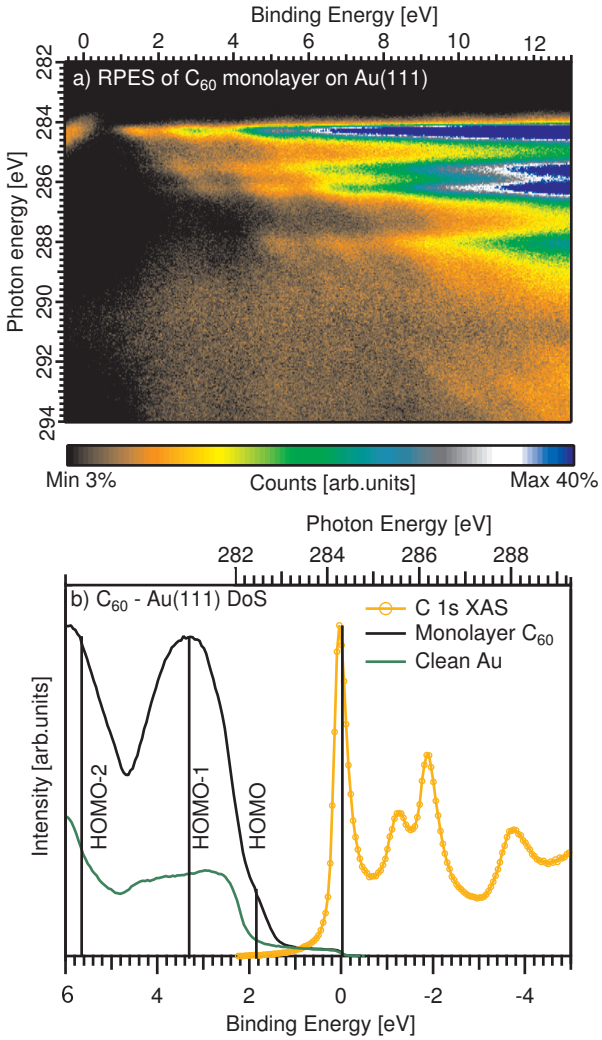

Figure 5.3: (a) C 1*s* RPES plot for monolayer C_{60} adsorbed on the Au(111) surface, exhibiting three diagonal constant high kinetic energy lines, (b) density of states plot for the C_{60}/Au(111) monolayer prepared in the same way as in Fig. 5.2b.

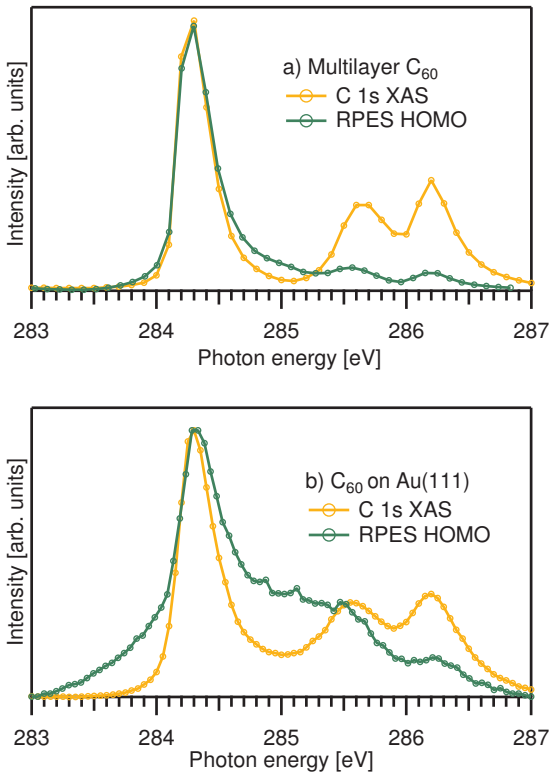

Figure 5.4: C 1*s* XAS and RPES traces for a) isolated molecules, and b) a monolayer of C_{60} on Au(111) obtained by integrating Auger (XAS) and participator (RPES) regions of Fig. 5.2a and Fig. 5.3a, respectively.

Since the LUMO lies just below the Fermi level (as shown in Fig. 5.3b), charge transfer from the surface into those electronic states of the molecule that overlap with the filled states of the surface is possible. In the case where the originally photoexcited electron is localised on the timescale of the core-hole lifetime, the three diagonal features are attributed to spectator decay processes involving Core/LUMO/HOMO (see Fig. 5.1d), Core/LUMO/HOMO-1, and Core/LUMO/HOMO-2 transitions made possible by a partially occupied LUMO.

Charge transfer in the other direction - from the molecule into the unoccupied states of the surface - can be investigated by considering the participator electrons in the RPES. By comparing the relative intensities of the participator channel to the XAS for both the monolayer and multilayer the timescale of the charge transfer dynamics can be estimated.[26] The XAS represents the full intensity of the unoccupied levels, whereas in the RPES the unoccupied states may be depleted by charge transfer from the molecule into the substrate. Charge transfer competes with the core-hole decay so to have an observable effect on the intensity of the participator channel it would need to be on the same timescale as the C $1s$ core-hole lifetime. The participator channels are maximally populated in the multilayer since the excited electron cannot transfer from the uncoupled molecule to the surface, this represents the maximum intensity of the participator channel. Depletion of this channel in the monolayer is therefore indicative of charge transfer to the surface on the timescale of the core-hole lifetime. Line traces for the C $1s$ XAS and RPES are shown in Fig. 5.4, the traces where made by integrating over the relevant binding energy window as a function of photon energy. The RPES trace is an integration over the HOMO region ($1-3$ eV), while the XAS region is an integration over the normal Auger region (above 10 eV).

In principle, a charge transfer time for electron transfer out of a particular unoccupied molecular orbital can be calculated using equation 5.1,

$$\tau_{EI} = \tau_{CH} \frac{I^{mono}_{RPES}/I^{mono}_{XAS}}{I^{multi}_{RPES}/I^{multi}_{XAS} - I^{mono}_{RPES}/I^{mono}_{XAS}} \tag{5.1}$$

where the $I^{mono}_{RPES}/I^{mono}_{XAS}$ terms represent the relative intensities of the par-

ticipator channel in the RPES as a fraction of the total x-ray absorption for the relevant molecular orbital given by the XAS. The $I^{multi}_{RPES}/I^{multi}_{XAS}$ term represents the fraction of participator electrons that would be expected in the absence of charge transfer as determined from the decoupled molecules in the multilayer film. The lifetime of the C $1s$ core-hole is given by τ_{CH} and is approximately 6.6 fs.[95] For a complete discussion of the core-hole clock implementation of RPES, including derivation of this equation, the reader is directed to Brühwiler et al.[26] A normalisation of the monolayer and multilayer data is typically achieved by considering a molecular orbital for which charge transfer is forbidden in all situations. This is often achieved by normalisation to the LUMO intensity in cases where this orbital lies energetically well below the conduction band edge or the Fermi level of the surface to which the adsorbed molecules are coupled. However, in the case of C_{60} on Au(111) the LUMO straddles the Fermi level so that charge transfer is possible from those vibrational levels of the LUMO that overlap with the empty states above the Fermi level. A convenient normalisation point for this system and by extension a quantitative timescale for the charge transfer dynamics therefore cannot be found. Nevertheless, the data shown in Fig. 5.4 have been normalised to the intensity at the LUMO resonance for both the monolayer and multilayer in order to assess qualitative differences in the charge transfer coupling of the different molecular orbitals with the Au(111) surface.

For both the C_{60} multilayer and the monolayer on Au(111) there is a significant participator (RPES) signal for all three of the unoccupied molecular orbitals probed. This implies that the core-excited electrons are localised in the LUMO, LUMO+1 and LUMO+2 long enough to participate in the core-hole decay and is indicative of a slow rate of charge transfer to the surface even for those molecular orbitals that overlap with empty states above the Fermi level. The monolayer RPES integration in Fig. 5.4 contains additional intensity around 285 eV absorption energy resulting from the highest kinetic energy Auger-like feature which overlaps the integration window at the LUMO+1 photon energy. A quantitative analysis concerning the LUMO+1 is not possible, however the region around the LUMO+2 lies beyond affected energy range and thus the intensity of the LUMO+2 participator channel can be assessed rela-

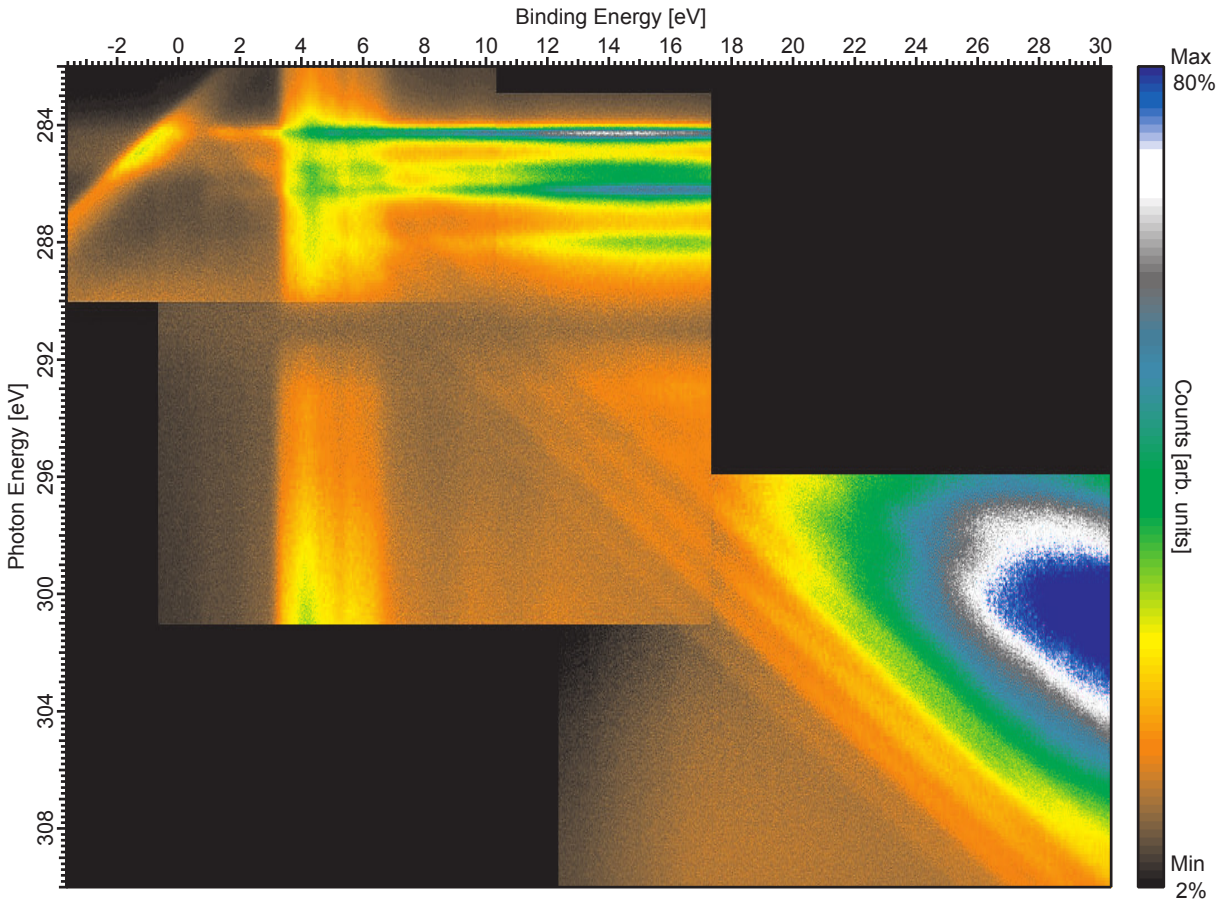

Figure 5.5: C 1s RPES plot for a C_{60} monolayer adsorbed on a Ag(111) surface, constructed from three separate datasets to show the full extent of the constant high kinetic energy Auger-like features as the photon energy is increased above the LUMO resonances and above the ionisation threshold.

tive to the LUMO. By curve fitting the spectra, $I^{mono}_{RPES}/I^{mono}_{XAS}$ and $I^{multi}_{RPES}/I^{multi}_{XAS}$ for the LUMO+2 orbital were found to be 0.35 ± 0.04 and 0.15 ± 0.01 respectively. Quantitatively this is interpreted as a higher relative drop in intensity for LUMO compared to the LUMO+2, which is indicative of faster charge transfer out of the LUMO compared to the LUMO+2.

5.3.3 C_{60}/Ag(111) monolayer

The C 1s RPES data for a C_{60} monolayer adsorbed on the Ag(111) surface is shown in Fig. 5.5. At the LUMO resonance around 284 eV photon energy three

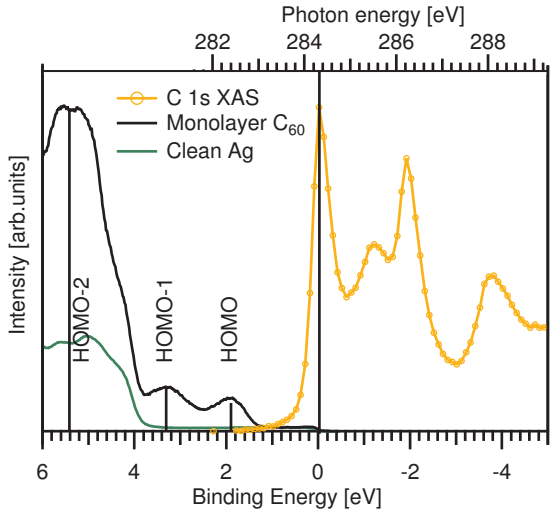

Figure 5.6: Density of states plot for the C_{60} monolayer adsorbed on the Ag(111) surface.

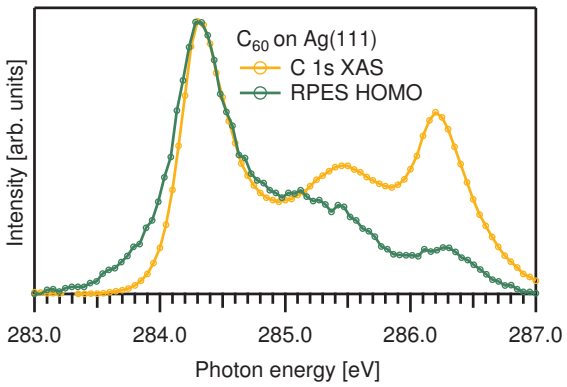

Figure 5.7: C 1s XAS and RPES traces for the C_{60} monolayer adsorbed on the Ag(111) surface.

enhancements are observed at the binding energies of the HOMO, HOMO-1 and HOMO-2,3 similar to those observed for both the multilayer film and the C_{60} monolayer adsorbed on the Au(111) surface. These features are again attributed to participator decay involving the electron localised in the LUMO on the timescale of the core-hole lifetime and electrons from each of the highest occupied molecular orbitals respectively. The vertical band of intensity between 3 and 7 eV binding energy is due to direct photoemission of the valence band of the underlying metal surface, which is more evident for Ag(111) than Au(111) due to a larger photoionisation cross-section for the Ag $4d$ states compared to the Au $5d$ state (0.73 and 0.19 Mbarn, respectively).[112, 113]

Three constant high kinetic energy features can be seen to track back to the binding energy positions of the HOMO, HOMO-1 and HOMO-2,3 at the LUMO resonance. These are attributed to the same Auger-like decay transitions presented for the C_{60}/Au(111) in section 5.3.2. In order to explore how these features develop as the absorption photon energy is increased further above resonance Fig. 5.5 is composed of three RPES datasets that span a binding energy window up to 30 eV and a photon energy up to 310 eV. The three features associated with the Core/LUMO/HOMO, Core/LUMO/HOMO-1 and Core/LUMO/HOMO-2 transitions are clearly observed at higher absorption energies. Moreover, a fourth, slightly weaker and even higher kinetic energy feature is also observed. The kinetic energy of this line is approximately 2 eV higher than the Core/LUMO/HOMO line. This energy shift is consistent with the HOMO-LUMO separation of the C_{60} molecule as measured in the core-excited state by placing the valence band and C1s XAS on a common binding energy scale as shown in Fig. 5.6. Confirmation of the kinetic energy shift and an indication of the origin of this highest kinetic energy line is found by extrapolating back to the LUMO resonance, where it intersects with a binding energy consistent with the LUMO itself. Indeed, a careful inspection of the RPES data shown in Fig. 5.5 reveals a weak enhancement at a binding energy of 0 eV at the LUMO resonance, consistent with the position of the LUMO in Fig. 5.6. This enhancement is attributed to participator decay of the partially occupied LUMO at the LUMO resonance. Such a weak enhancement is only observable in this data due to the nature of the measurement that re-

veals the increased intensity superimposed on the second order C 1s peak with which it coincides. In the case where the originally excited electron is localised on the timescale of the core-hole lifetime, the highest constant kinetic energy line observed in the C_{60}/Ag(111) data is attributed to a Core/LUMO/LUMO spectator transition, which can only take place if more than one electron is transferred from the silver surface into the LUMO (see Fig. 5.1f).

A core hole clock analysis of the RPES data for the C_{60} monolayer on Ag(111) is shown in Fig. 5.7 normalised as for Au(111) to the intensity at the LUMO resonance. The ratio of participator electrons to x-ray absorption for the LUMO+2 in this case is $I^{mono}_{RPES}/I^{mono}_{XAS}$ is 0.25 ± 0.3, compared to the multilayer value of 0.15 ± 0.01. As in the case for Au this is interpreted quantitatively as a larger relative drop in intensity for the LUMO compared to the LUMO+2, which is again indicative of faster charge transfer from the LUMO compared to the LUMO+2.

5.3.4 C_{60}/Cu(111) monolayer

The C 1s RPES data for a C_{60} monolayer adsorbed on the Cu(111) surface is shown in Fig. 5.8a. The data is dominated by the valence states of the copper surface due to the large photoionisation cross-section of the Cu 3d states at these photon energies (1.2 Mbarn[112, 113]), observed as an intense vertical band from 1 eV to 5 eV binding energy. No clear participator enhancements are detectable in the RPES data and no distinct narrow constant kinetic energy features are observed unlike the data for Au(111) and Ag(111). The density of states plot is shown in Fig. 5.8b, and a substantial modification of the unoccupied molecular orbitals compared with the multilayer is observed. There is no distinct LUMO resonance observed around 0 eV binding energy. This is consistent with substantial charge transfer into the LUMO of the molecule due to the adsorption interaction with the surface. The occupied density of states for the molecule shown also in Fig. 5.8b exhibits some intensity just below the Fermi level consistent with charge transfer into the LUMO, which is now observed as an occupied molecular orbital. In addition to a partially filled LUMO state, the valence spectra exhibit four occupied molecular peaks

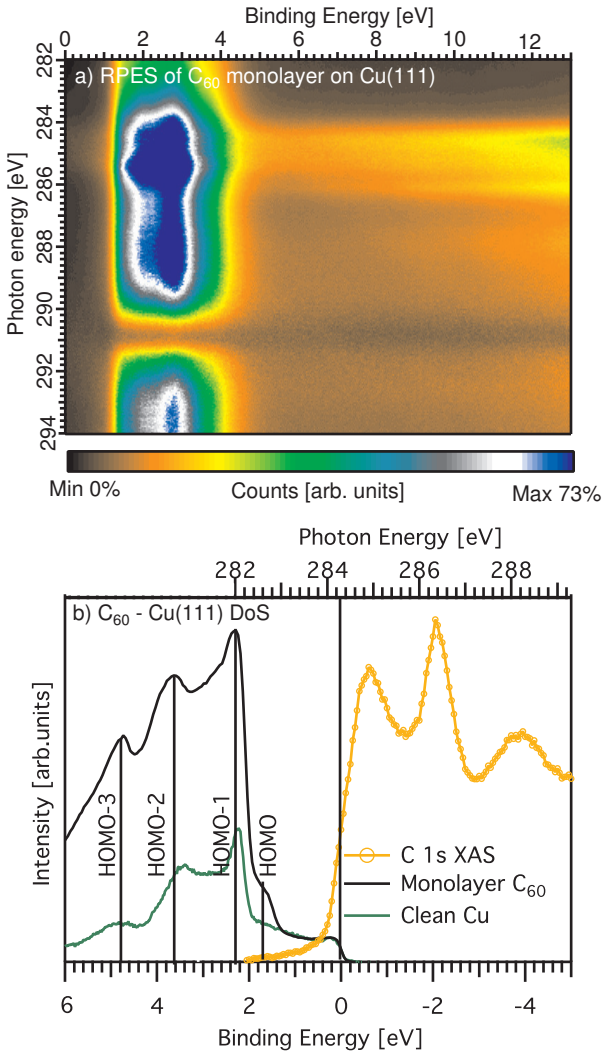

Figure 5.8: a) RPES and b) density of states plot for the C_{60}/Cu(111) monolayer.

attributed to the HOMO to HOMO-3 orbitals. The binding energies of these orbitals are shifted relative to the multilayer, in particular the HOMO-1 and HOMO-2 peaks. This is indicative of the molecules still intact on the surface but forming a relatively strong chemical interaction with the surface. The absence of any high kinetic energy Auger features for the C_{60} monolayer adsorbed on the Cu(111) surface is notable since one might expect such features to be more intense where more electron density is transferred to the molecule.

5.3.5 C_{60}/Pt(111) monolayer

The C 1s RPES data for a C_{60} monolayer adsorbed on the Pt(111) surface is shown in Fig. 5.9a. The data is dominated only by the Auger decay feature observed at the absorption energies of the lowest unoccupied molecular orbitals, with virtually no contribution from the underlying surface due to the low photoionisation cross-section of the Pt 5d states at these photon energies (0.098 Mbarn[112, 113]). The density of states plot is shown in Fig. 5.9b revealing a substantial modification of the molecular orbitals compared with the multilayer, consistent with a strong chemical interaction with the surface. The LUMO of the chemisorbed molecule now lies 0.6 eV above the Fermi level so charge transfer into this state from the surface is not possible. Based on the data for Au(111) and Ag(111), charge transfer into the LUMO is required for the Core/LUMO/HOMO core-hole decay channel to be populated, and the absence of this or similar features for the C_{60}/Pt(111) monolayer is consistent with a negligible energetic overlap of the LUMO with the occupied density of states in the surface.

5.4 Discussion

The resonant photoemission and resonant Auger data for monolayers of C_{60} on metal surfaces presented in this paper show evidence for a series of Auger-like core-hole decay processes in which electrons transferred from the metal surface into the LUMO of the molecule play a direct role in filling the core-hole. Three questions remain though: i) whether or not there is simultaneously ultra-fast

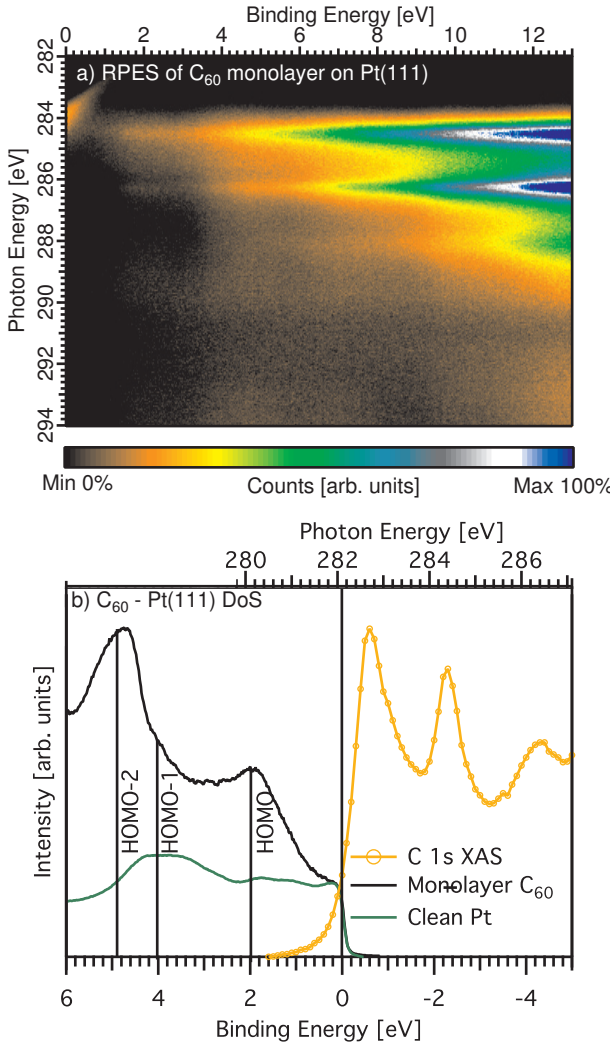

Figure 5.9: a) RPES and b) density of states plot for the C_{60}/Pt(111) monolayer.

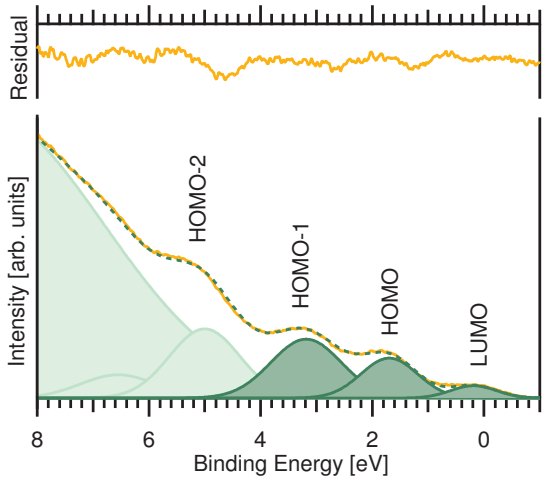

Figure 5.10: Integrated intensity over the super-Auger features as a function of constant kinetic energy in the photon energy region from 300 to 305 eV photon energy in Fig.5.5 for the C_{60}/Ag(111) monolayer. The spectrum has been converted to a binding energy scale by extrapolating back to the binding energy positions at the LUMO resonance.

charge transfer from the molecule to the surface on the timescale of the core-hole lifetime, ii) whether or not the charge transfer from the surface to the LUMO occurs already in the ground state or only in the core-excited state (in which case it would also be ultra-fast on the timescale of the core-hole lifetime of a few fs), and iii) whether or not it is possible to estimate how much electron density is transferred into the LUMO.

In the case of C_{60}/Au(111) three constant high kinetic energy features are observed separated by the energy spacing of the three highest occupied molecular orbitals and track back the binding energies of those orbitals at the LUMO resonance. If we consider the energy levels schematically represented in Fig. 5.1 and perform a *Gedankenexperiment* for core-excitation to the LUMO, we find three different scenarios of core-hole decay using only the electrons intrinsic to the molecule. Participator decay in this case (Fig. 5.1b) leaves the system in a final state identical to photoemission from the HOMO. Participator electrons will therefore be observed in the RPES dataset at the binding energy of the HOMO regardless of the incident photon energy. Spectator decay in the illustrated case (Fig. 5.1c) leaves the system in a final state similar to

photoemission from the HOMO plus an excitation of an electron from the HOMO to the LUMO. These electrons have a constant kinetic energy and when excited with photons corresponding to the LUMO resonance will therefore be observed in the RPES at a binding energy that is shifted by an amount corresponding to the HOMO-LUMO gap to higher binding energy than the HOMO, and by extension the participator. Spectator electrons, since they always involve the same energy levels (in this case Core/HOMO/HOMO) will track with constant kinetic energy. Both participator and spectator decay require the originally photoexcited electron to be localised in the core-excited molecule on the timescale of the core-hole lifetime (a few fs). If on the other hand it tunnels into the conduction band of the coupled surface the system will undergo Auger decay. Auger decay in the illustrated case (Fig. 5.1d) leaves the system in a state similar spectator decay plus an excitation of an electron from the LUMO out of the molecule. Auger electrons again have a constant kinetic energy and at the LUMO resonance will appear in the RPES at a binding energy that is shifted to even higher binding energy than the spectator feature by an amount corresponding to the cost of removing the electron from the LUMO (the energy difference between the normal Auger and spectator decay is referred to as the spectator shift). So while Auger and spectator electrons track with constant kinetic energy as a function of increasing photon energy, they cannot track back to the binding energy of the HOMO at the LUMO resonance because no transition exists using only the electrons intrinsic to the molecule that can result in such a high kinetic energy electron emission.

To understand the origin of the high kinetic energy Auger-like features observed for C_{60}/Au(111) we need to consider charge transfer from the metal surface into the LUMO of the molecule, schematically shown in the lower half of Fig. 5.1. A constant kinetic energy feature that tracks back to the binding energy of the HOMO at the LUMO resonance requires an Auger-like core-hole decay process that leaves the system in a final state identical to photoemission from the HOMO. The corresponding *Gedankenexperiment* is represented in Fig. 5.1e, where the core-hole is filled by an electron from the HOMO as in previous schemes and the emitted electron is now the electron that was transferred from the surface into the LUMO. However, this scheme also

requires that the originally photoexcited electron tunnels into the substrate on the timescale of the core-hole lifetime, otherwise the kinetic energy would be increased due to the presence of that electron in the LUMO (a spectator shift). This core-hole decay channel is therefore an Auger decay involving an electron transferred to the LUMO from the surface and will appear in the RPES as a constant kinetic energy feature (since the photoexcited electron does not play a role) that tracks back to the position of the HOMO at the LUMO resonance. The lower kinetic energy features that track back to the HOMO-1 and HOMO-2/3 are explained by the analogous transitions where the electrons that fill the core-hole originate from those orbitals respectively.

Rather than superspectator electrons, a more accurate term for the observed high constant kinetic energy features would be *super-Auger* electrons since the originally excited electron is no longer present to spectate on the process. The ultra-fast charge transfer of electrons from the unoccupied molecular orbitals of the molecule is facilitated by the energetic overlap of all the LUMO states of the core-excited molecule with empty density of states in the metal surface as shown in Fig. 5.3b. In addition, while the presented core-hole clock analysis cannot be determine an absolute charge transfer timescale, it does however provide evidence for differences in the charge transfer dynamics on the timescale of the core-hole lifetime indicating that tunnelling of the electrons out of the molecule occurs on a timescale on this order. Ultra-fast charge transfer between an adsorbed molecule and a surface on the low femtosecond timescale is well established in RPES studies,[22, 26, 30, 48, 49, 70, 114] and a similar interpretation involving ultra-fast *bidirectional* charge transfer has also recently been presented for bipyridine molecules adsorbed on the Au(111) surface.[100] Further support for a super-Auger interpretation of the high kinetic energy features is shown in the C_{60}/Ag(111) data (Fig. 5.5) which extends to photon energies far above the ionisation threshold. The kinetic energy of the super-Auger features are observed to track perfectly linearly with photon energy with no observable spectator shift that would be expected to be present below and not present above the ionisation threshold where the electron is no longer localised on the molecule. It seems reasonable to conclude that the core-hole decay channel that gives rise to these high kinetic energy features

involving charge transfer from the surface into the molecule is accompanied by ultra-fast charge transfer out of the molecule to the surface.

However, while this interpretation requires charge transfer from the LUMO states into the surface to occur on the timescale of the core-hole lifetime, there is no such requirement on the timescale of charge transfer from the surface into the LUMO - all that is required is that there is an electron in the LUMO prior to the core-hole decay. This requires an energetic overlap of the LUMO with the filled states in the surface. The energy level alignments shown in Fig. 5.3b and Fig. 5.6 show that the LUMO of the C_{60}/ molecule crosses the Fermi edge of the surface and thus overlaps the occupied density of states in both the Au(111) and Ag(111) surfaces. However, XAS measures only the unoccupied molecular orbitals in the core-excited state where excitonic effects have been shown to lower the energy of the LUMO states sometimes significantly.[56, 110] It is therefore possible for a molecule LUMO to be located above the Fermi level and to be pulled down below the Fermi level only in the core-excited state. In this case the charge transfer from the surface into the LUMO that gives rise to the super-Auger channels that we observe would need to take place on the low femtosecond timescale, comparable to the core-hole lifetime. Charge transfer from the surface into a molecule is likely to be much slower process than from the molecule into the conduction band of a surface. This is due to vastly more conduction band states than molecular states, when the electron transfers into the surface, coherence with the initial state is lost on a timescale of 10 fs, compared with transfers of the order 100 fs in the reverse direction.[49, 115, 116] Ultra-fast charge transfer into the LUMO of bipyridine molecules has recently been studied[100], however in the case of C_{60} several studies have reported charge transfer in the ground state associated with adsorption showing a varying degree of charge transfer between the C_{60} molecule and the surface during bonding to the metal surface.[101–108] The C 1s X-ray absorption shown in Fig. 5.3b closely matches in both energies and intensities that of the C_{60} multilayer in Fig. 5.2b. This suggest a relatively small amount of charge transfer into the molecule during binding to the surface, which is consistent with previous results that found a charge transfer from Au(111) of 0.8-1.0 electrons per C_{60} molecule.[101, 107] The C 1s RPES data for Ag(111) shown in Fig. 5.5 ex-

hibits three well-defined, narrow and relatively intense lines corresponding the same Core/LUMO/Valence transitions as discussed for Au(111). The fact that these are much more easily measured for the Ag(111) surface than Au(111) suggests that these channels are more populated. This would be consistent with the transfer of more electrons to the molecule than on the Au(111) surface. The C 1*s* XAS shown in Fig. 5.6 qualitatively supports a higher degree of electron transfer into the LUMO since the relative intensity of the LUMO is weaker than either the multilayer or the C_{60}/Au(111) monolayer, reflecting a lower unoccupied density of states. It would seem reasonable to conclude that there is sufficient overlap of the LUMO of C_{60} with the valence states of the gold and silver surfaces to facilitate charge transfer into the LUMO already in the ground state even if the energy of the LUMO in the core-excited state is lowered due to the creation of a core-LUMO exciton. This would imply that the effect of the core-LUMO exciton on the binding energy of the LUMO is limited to around 0.3 eV otherwise no appreciable overlap between this level and the occupied states of the surface would be present in the ground state to enable charge transfer. This would imply efficient screening of the core-hole by the metal surface or that the LUMO is pinned to the Fermi level of the substrate.

The most significant result from the Ag(111) data shown in (Fig. 5.5) is the presence of a fourth, even higher kinetic energy super-Auger feature that tracks back to the binding energy of the LUMO at the LUMO resonance. The process requires two electrons to be present in the LUMO to participate in the core-hole decay as illustrated in Fig. 5.1f. Two LUMO electrons are required to drive this Core/LUMO/LUMO Auger-like transition at all photon energies. The originally photoexcited electron is not shown in the scheme since we assume that it tunnels into the conduction band and plays no further role. The extent of charge transfer from silver to adsorbed C_{60} is debated. The bond to polycrystalline Ag has been shown to be ionic with a charge transfer of 1.7 ± 0.2 electrons per molecule via UPS.[101] Combined UPS/XPS experiments performed on single crystal Ag(111) also assumed an ionic coupling but with only 0.7 electrons involved in the charge transfer.[102] Other experiments using XAS have reported a covalent nature to the C_{60}-Ag(111) bond due to some

degree of hybridization between the two highest molecular orbitals and the valence band of the surface.[110] A hybridization between the HOMO-1 of the molecule and the Ag $4d$ state of the surface has also been reported.[103] The observation of the fourth super-Auger feature in (Fig. 5.5) strongly suggests that the amount of electron charge transfer into the LUMO must certainly be more than one electron (see Fig. 5.1f).

By integrating the intensities over the four super-Auger lines observed in Fig. 5.5 in the photon energy region from 305-310 eV at constant kinetic energy we can obtain the intensity of the LUMO-related peak in the resonant Auger relative to those associated with the HOMO, HOMO-1 and HOMO-2 orbitals. The resulting spectrum has been converted to binding energy by extrapolating back to the binding energy positions at the LUMO resonance and is shown in Fig. 5.10. The high binding energy peaks in Fig. 5.10 shown as faded components are based on the Auger region of the multilayer data from Fig. 5.2 and are included only as an aid to obtaining more accurate fits of the HOMO-1, HOMO and LUMO components, and were adjusted so the HOMO-1:HOMO was fixed at the expected 1.8:1 ratio for the C_{60} molecule.[117] If we assume that the intensities of the features associated with super-Auger decay from the HOMO, HOMO-1 and HOMO-2 orbitals are a result only of the occupation of each molecular orbital and not due to any matrix element effects in the transition probability we can infer the relative occupation of the LUMO state and thus the degree of charge transfer from the surface. The intensity of the LUMO-derived super-Auger peak is (24 $\pm$ 3)% of the HOMO-derived peak. Based on a HOMO occupation of 10 electrons, this result suggests that 2.4 $\pm$ 0.3 electrons on average are transferred from the Ag(111) surface to each C_{60} molecule.

The adsorption of C_{60} to the Cu(111) surface is also thought to be ionic with differing degrees of charge transfer reported. Valence band photoemission and XAS data have estimated the charge transfer at 1.5-2 electrons per molecule.[105] A more recent STM and STS study indicated a 3 electron transfer to the molecule.[106] while another photoemission study estimates a charge transfer of 1.6 electrons per molecule.[107] Our photoemission and XAS data clearly show a significant degree of charge transfer, however no super-Auger

features were observed in the RPES. We attribute this to the profound change in the unoccupied molecular orbitals clearly observed in the XAS of Fig. 5.8b resulting in broad molecular orbital features.

In the case of C_{60} adsorption on Pt(111) the interaction with the surface is even stronger and molecular orbital peaks in both the occupied and unoccupied density of states shown in Fig. 5.9 are profoundly modified compared to the multilayer. Again, no super-Auger decay channels were observed for this surface, despite the possibility of significant charge transfer into the molecule previously estimated to be around 2 electrons per C_{60} molecule.[104] It has also been shown that even moderate temperatures can induced polymerisation and decomposition of C_{60} on Pt(111) which might complicate the situation on this surface.[104, 118]

5.5 Conclusion

Resonant photoelectron spectroscopy at the C 1s absorption edge for C_{60} monolayers adsorbed on Au(111) and Ag(111) surfaces exhibit high constant kinetic energy Auger-like features associated with Auger decay of the core-hole via a transition involving electrons charge transferred from the metal surface into the LUMO of the molecule and therefore referred to as super-Auger electrons. The presence of three super-Auger channels for the C_{60}/Au(111) monolayer corresponding to the Core/LUMO/HOMO, Core/LUMO/HOMO-1 and Core/LUMO/HOMO-2 transitions suggests that only one electron is transferred to the LUMO since the channel associated with the Core/LUMO/LUMO transition is not observed. This channel is however observed for the C_{60}/Ag(111) monolayer and by comparing the intensity of the Core/LUMO/LUMO channel with the Core/LUMO/HOMO channel we are able to estimate the degree of charge transfer from the silver surface states into the C_{60} LUMO to be 2.4 $\pm$ 0.3 electrons on average for each C_{60} molecule. For systems in which more than one electron is transferred thus opening the LUMO-derived super-Auger channel in the RPES data, the degree of charge transfer can be inferred from the relative abundance of each channel. This approach is applicable to a large number of molecule-surface

combinations in which significant charge transfer takes place upon adsorption. In contrast, monolayers of C_{60} on the surfaces of Cu(111) and Pt(111) do not exhibit these core-hole decay features in any resolvable way due to the stronger molecule-surface interactions and the substantial modification of the molecular orbitals.

Chapter 6

Summary and Conclusions

I used the introduction of this thesis to look at the broader use of electricity worldwide since 1980, highlighting the need for further research and investment in all renewable technologies and solar in particular. From this data is it undeniable that renewable technologies such as solar are vital in our fight against ever growing demand for energy and irreparable manmade climate change from CO_2 emissions.

This research is less the practical development of solar technology and more the fundamental understanding behind the critical adsorption bonding, electron coupling and charge transfer processes which underpin that technology. The goal of this thesis was to better understand the charge transfer dynamics in model molecular solar cells particularly nanoscale alumina films, C_{60}, dye molecules and their derivatives. Hence the focus of this thesis was firstly to study the charge transfer dynamics due to oxide passivation layers which form recombination barriers in DSCs and secondly to further study the core-hole decay of a charge transfer and core hole decay process which lead to a constant kinetic energy features on RPES images of C_{60} on Au and Ag(111).

Chapter 4 used a self terminating ultra thin alumina layer on AlNi(110) to study the charge transfer from N3 through this oxide and into the underlying metallic substrate. After electrospraying N3 onto the surface it was observed that the molecule adopted a range of bonding geometries on the surface, which was caused by one and two deprotonations of each of the N3 molecule's carboxylic acid groups during adsorption to the surface. A charge transfer time

of 6.0 ± 2.5 fs was found from the dye molecule through the ultra thin alumina and into the metallic substrate. This compares to upper limits of 4.4 fs for N3 on Au(111),[47] 12 fs on TiO_2,[48] and 3 fs for bi-isonicotinic acid on TiO_2.[30]

Chapter 5's original aim was to study the atomic layer deposition growth of alumina on titania through ALD with TMA and H_2O. The initial growth rate of 0.7 nm per ALD cycle was approximately six times higher than later and previously reported growth rate. Since this also lead to a non-homogenous alumina thickness on titania the opportunity was taken to study the charge transfer through different thicknesses of oxide, which was considered to be more interesting than the original aim. After 20 cycles of ALD the surface was categorised into thin (2.8 ± 0.2 nm), medium (3.4 ± 0.2 nm) and thick (4.0 ± 0.2 nm) alumina layers. A monolayer of the N3 ligand, bi-iso, was evaporated onto the surface and the charge transfer times from bi-iso and into the underlying titania substrate were found to increase with alumina thickness which were 25 ± 4 fs, 33 ± 6 fs and 50 ± 9 fs for the thin, medium and thick respectively.

Chapter 6 shifted focus slightly from true DSCs to a molecule used in other organic solar devices namely C_{60}. The primary aim of this chapter was to expand on the previous work of our group, by developing our understand of the superauger / superspectator features that were seen in the RPES data of C_{60} on Au(111) by studying it on three further metallic (111) surfaces. While on Pt and Cu surfaces no constant kinetic energy features were observed, the RPES spectra of C_{60} on Ag(111) showed four distinct features as a result of molecule surface interaction. It was proposed that the presence of superspectator/Auger features is dependant on the amount of charge transfer into the molecule during bonding to the surface. As a group we have already built on this research using the C_{60} based, such as PCBM, which are directly used in solar cell devices as bulk hetrojunctions,[119] however since I am not the primary author on this work it has not been included in this thesis.

Future research which could build on this thesis, I would suggest extending the work in Chapter 4 and 5 by building thinner oxides layers on TiO_2 with fewer repetitions of ALD and repeating the charge transfer from bi-iso and N3. The samples made could also then be connected to form a complete solar

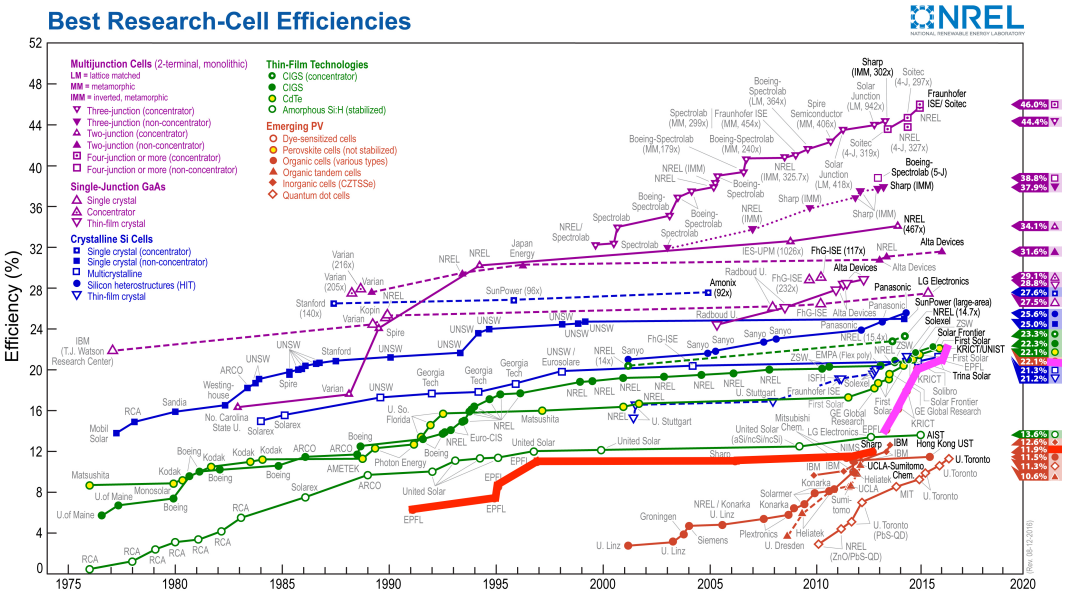

Figure 6.1: Comparison of best efficiencies achieved in lab based photovoltaic devices. Adapted from[8]. DSCs in bold red, perovskites bold pink.

cell and the properties tested to obtain the optimal oxide thickness on a DSC devices to tie this fundamental work more directly to lab based solar cells.

Since the breakthrough paper in 2012[120] perovskite solar cells have been stealing the limelight as an emergent solar technology. Since then the efficiency of lab based perovskite solar cells has risen dramatically from 10.9% to 22.1% far out striping the progress of DSCs, see Fig.6.1. There are still problems to resolve with perovskites if they are to overtake silicon solar cells. These are their durability to weather as they are susceptible to water, air and light and the ability to produce them in large quantities. However their promise of increased efficiency, low production cost and environmentally friendly engineering methods makes this development from DSCs a promising field for future research, which our future synchrotron based charge transfer studies could contribute to.

List of Figures

1.1 Relative increase in global net electricity generation, CO_2 emissions and population from 1980 to 2013.[1, 2] 2
1.2 Break down of world electricity production by fuel type from 1980-2013.[1, 2] 2
1.3 Breakdown of global non-hydroelectric renewable energy production from 1980-2012.[1, 2] 3
1.4 The coloured transparent dye sensitized solar cells on the west face of the SwissTech Convention Center, opened in 2014 (image labeled for reuse). 4
1.5 The typical DSC layout is shown in centre, the enlargement at the top shows the active region with the dye molecule, while below show a schematic for the energy transfers involved, incoming light (1), followed by electron excitation (2), transfer to substrate (3), to conductive glass (4), work in the circuit (5), recombination with electrolyte (6), from electrolyte to dye (7), exciton recombination (8) and recombination between the semiconductor and the dye cation (9). 6

2.1 Schematic of the most important parts of a modern synchrotron, diagram edited from.[19] 11

2.2 Above indicates how radiation propagates radially from an electron travelling at non relativistic velocities, compared to the highly intense, tangentially propagated narrow beam of radiation which is emitted from an electrons travelling at relativistic velocities. Below for the perspective of an observer an electron travelling towards them emits highly blue shifted radiation, while the off axis observer see a far less pronounced doppler shift, diagram edited from.[19]. 12
2.3 An undulator seen prior to its installation at the MAX-IV laboratory. 14
2.4 Schematic of and undulator/wiggler(above), how the radiation cones from each wiggle do not overlap and therefore intensity is added in a wiggler, while for an undulator has gentler excursion and the radiation cones do overlap, diagram edited from.[19] . . 14
2.5 Above, photograph of the I311 beam line, end station is omitted. Below schematic for the same beam line at max-lab, focusing pre-mirror (M1), rotatable plane mirror (M2), an in plane grating (G), a spherical focusing mirror (M3), aperture or slit (S1) beofre mirror that focus onto sample (M4 &5). 17
2.6 Photograph of the I311 end station, large area in the centre covered in foil is the prep chamber on top and analysis chamber below. The beam line can be seen entering from the left, which directs the beam into the analysis chamber. The righthand side shows the UHV pumps and gas line. 18
2.7 Schematic of electrospray deposition system, showing the thin capillary emitting molecular beam in atmosphere and travelling left to right, subsequent apertures through differentially pumped chambers of increasingly high vacuum before final incidence onto sample in UHV.[22] 21

2.8 Schematic of the ALD process, showing the subsequent deposition of precursors A and B, with by product C to create a thin film on the substrate. The surface does not become fully passivated in stage 1, in stage two the precursor B is applied and the structure of the film is seen at 2, 3 indicates impurities that remain. Below indicates structure of the film after multiple sequential exposures of precursors A and B. 23
2.9 Schematic diagram of a hemispherical electron analyser. 24
2.10 Excitation of a core level electron to a bound state XAS, followed by relaxation of the core-hole via Auger emission or fluorescence. 28
2.11 C 1s XAS example C_{60} monolayer on Ag(111) a) raw data from hemispherical analyser b) the integral of this data with respect to photon energy. 29
2.12 Data processing, original data from Ag C 1s XAS, grey. From this the carbon dip, black, is removed to produce red. 30
2.13 General concept of XPS, removal of core level electron through X-ray illumination with energy level diagram. 32
2.14 Example of an XPS overview taken on a clean TiO_2 surface, at two excitation energies, to show the fixed position of XPS peaks and excitation energy dependant position of Auger peaks. 33
2.15 C1s XPS of; left Ethyl-trifluoroacetate from ref [27] and right N3 on ultra thin alumina, taken from Fig.3.2, both Figures illustrate the different chemical environments identifiable for one element in a molecule. see text from more detailed description. . 34
2.16 Example of density of states plot for C_{60} on Cu, taken from Fig.5.8 35
2.17 The Ti $2p_{1/2}$ on the left is half the size of the Ti $2p_{3/2}$ on the right, for further explanation of this figure see Sec.4.3.2 36
2.18 Core-hole decay mechanisms for resonant photoemission, see text for further explanation. 37

2.19 RPES spectra for a multilayer or isolated molecules of C_{60} (above), indicating the positions of the unoccupied states (horizontal features) and RPES spectra for monolayer of C_{60} on Cu(111) showing vertical features that are due to the highest occupied states of the Cu(111) substrate, taken from Fig.5.2(a) and Fig.5.8(a). 39

3.1 Schematic of N3 molecule on ultra-thin aluminium oxide layer. O - Red, H - White, C - Grey, N - Blue, S - Yellow, Al - Purple. The underlying AlNi(110) substrate is omitted. 46

3.2 C 1s plot fit for (a) multilayer data and (b) monolayer, with different peaks for each of the different bonding environments of carbon. The ratios of the peaks fit with expected result for the intact molecule. Peak positions are the same across all coverages with the exception of the carboxylic acid peak, which is involved in intermolecular bonding in monolayer and multilayer coverages. hν=340 eV. 50

3.3 O 1s Plots normalised to the surface peak, black is background data of the clean surface with identical peak position and shape in the clean surface and monolayer, striped peaks are from the molecule with identical peak position and shape in the multilayer and monolayer. The ratio of the peaks in the monolayer suggest a combination of single and double de-protonation is involved when the molecule bonds to the surface. hν=600 eV. . 51

3.4 S 2p XPS showing the spin-orbit split S $2p\frac{1}{2}$ (left) and S $2p\frac{3}{2}$ (right) contributions, exhibiting a single chemical state for the sulphur atoms in the molecule with no binding energy shift at different coverage. Spectra were measured with hν = 225 eV and normalised to the height of the main peak. 53

3.5 N 1s XPS measured for multilayer and monolayer of N3, indicating no change in chemical environment between different coverage. The larger peak is due to nitrogen in the bi-isonicotinic acid ligands, while the smaller peak is due to the thiocyanate ligands, with a 2:1 intensity ratio. Spectra were measured with hν = 500 eV and normalised to the height of the main peak. . . 54

3.6 Valence band plots at varying coverages, a) clean substrate (black). Higher lines represent increasing coverage. b) partial monolayer (blue), calculated at 0.3ML c) monolayer (green) 0.85ML d) is a thick film or multilayer (red) 9ML. All taken at hν=50 eV. 55

3.7 Electron excitation and subsequent core-hole induced decay processes: (a) x-ray absorption, resonant core-level excitation into unoccupied bound states; (b) participator decay; (c) spectator decay; and (d) x-ray absorption in the presence of charge transfer from molecular orbital into states near the fermi level of the metal substrate. For the substrate solid colour black white and grey represents occupied states, unoccupied states and band gap respectively. 56

3.8 Density of States plot constructed from N 1s XAS and VB data, (a) multilayer and (b) monolayer coverage with the underlying substrate in black indicating a clear overlap between the unoccupied states of the molecule with the conduction edge of the AlNi(110) substrate. 57

3.9 N 1s RPES multilayer (a) which is the sum of six individual RPES images, four of which are from,[22, 48] the monolayer (b) is also the sum from six individual RPES spectra. All images were normalised to the beam intensity. The integration window (0-9eV) for the core-hole-clock calculation is also indicated. . . . 58

3.10 N 1s RPES and N 1s XAS spectra for the N3 multilayer (a) and monolayer (b). The multilayer data are integrations from 0 eV to 9 eV over all datasets. Also shown are the 6× magnification of the LUMO+2 and LUMO+3 regions after background removal. 60

4.1 Schematic diagram of Bi-isonicotinic acid molecule, (4,4'-dicarboxy-2,2'-bipyridine). 65
4.2 Rate of alumina growth over 21 cycles of ALD, green line indicates initial growth rate and constant growth rate similar to that previously seen in the literature after 8 cycles. 69
4.3 Suppression of the TiO_2 (a) and valence band (b) with subsequent cycles of ALD, taken at 600 eV and 50 eV respectively. . . 70
4.4 Shift in the Al $2p$ XPS peak from 74.2 to 74.7 eV during the alumina growth, b) sample of the Gaussian fits. Solid line are the data taken after TMA while dashed line of the same colour is after the subsequent H_2O dose. 72
4.5 O $1s$ XPS a) during alumina growth, b) fits indicate two clear species, Ti-O and Al-O at 530.1 eV and 531.2 eV respectively. . . 73
4.6 Shift in the C $1s$ XPS peaks during the Al oxide growth, showing the first (purple), four (green), twentieth (pink), completed TMA dosing and after twenty completed rounds and annealed to 500K for 20 mins (black), the corresponding subsequent H_2O dose is also shown (blue). Red line indicate shift on the main peak after TMA dosing, while blue line shows the persistent position of the peak after H_2O dosing. 74
4.7 O $1s$ of alumina on titania substrate shown in black, isolated bi-isonicotinic acid two peak O $1s$ in blue, and monolayer bi-isonicotinic acid on alumina on titania shown in red. 76
4.8 C $1s$ of alumina on titania substrate shown in black, isolated bi-isonicotinic acid two peak O $1s$ in blue, and monolayer bi-isonicotinic acid on alumina on titania shown in red. 77
4.9 Density of states plots of bi-isonicotinic acid isolated from the surface two peak in (blue), monolayer bi-isonicotinic acid on alumina on titania shown (red) and the alumina on titania surface (black). 78
4.10 bi-isonicotinic acid on alumina on titania , XPS isolated bi-isonicotinic acidtwo peak in (blue), monolayer bi-isonicotinic acid on alumina on titania shown (red). 79

4.11 Aluminium oxide thickness a) the suppression of TiO_2 due to b) increased alumina coverage. Thick alumina (blue), intermediate (green) and thin (red). 80
4.12 RPES data of molecules isolated from the surface in the multilayer and monolayer on three categorised thicknesses of alumina. 81
4.13 C 1s XAS and RPES data obtained by integrating of the indicated regions of Fig.4.12 in order to perform Core-hole-clock analysis. 84

5.1 Schematic illustration of the key electron excitation and subsequent core-hole decay processes observed for a molecule adsorbed on a metallic surface and relevant charge transfer interactions. (a) XAS excitation of a core-level electron (orange) into an unoccupied molecular orbital, in this case the LUMO; (b) participator decay; (c) spectator decay; and (d) charge transfer of the photoexcited electron to the substrate conduction band followed by Auger decay (black and grey shaded areas represent occupied and unoccupied states of the surface respectively), (e) charge transfer of an electron (green) from the substrate valence band into the LUMO of the molecule, followed by ultra-fast charge transfer of the originally photoexcited electron into the substrate conduction band and subsequent super-Auger decay involving the electron (green) transferred from the surface, and (f) charge transfer of two electrons (green) from the substrate valence band into the LUMO of the molecule, followed by super-Auger decay involving the electrons (green) transferred from the surface (ultra-fast charge transfer of the originally excited electron assumed to take place but omitted for clarity). 87

5.2 a) RPES for a C_{60} multilayer obtained by measuring the valence photoemission whilst incrementally increasing the photon energy over the C 1s absorption edge, and b) a density of states plot for multilayer of C_{60} obtained by placing the C 1s XAS on a common binding energy scale with the valence band photoemission ($h\nu = 60\,eV$). 90

5.3 (a) C 1s RPES plot for monolayer C_{60} adsorbed on the Au(111) surface, exhibiting three diagonal constant high kinetic energy lines, (b) density of states plot for the C_{60}/Au(111) monolayer prepared in the same way as in Fig. 5.2b. 94

5.4 C 1s XAS and RPES traces for a) isolated molecules, and b) a monolayer of C_{60} on Au(111) obtained by integrating Auger (XAS) and participator (RPES) regions of Fig. 5.2a and Fig. 5.3a, respectively. 95

5.5 C 1s RPES plot for a C_{60} monolayer adsorbed on a Ag(111) surface, constructed from three separate datasets to show the full extent of the constant high kinetic energy Auger-like features as the photon energy is increased above the LUMO resonances and above the ionisation threshold. 98

5.6 Density of states plot for the C_{60} monolayer adsorbed on the Ag(111) surface. 99

5.7 C 1s XAS and RPES traces for the C_{60} monolayer adsorbed on the Ag(111) surface. 99

5.8 a) RPES and b) density of states plot for the C_{60}/Cu(111) monolayer. 102

5.9 a) RPES and b) density of states plot for the C_{60}/Pt(111) monolayer. 104

5.10 Integrated intensity over the super-Auger features as a function of constant kinetic energy in the photon energy region from 300 to 305 eV photon energy in Fig.5.5 for the C_{60}/Ag(111) monolayer. The spectrum has been converted to a binding energy scale by extrapolating back to the binding energy positions at the LUMO resonance. 105

6.1 Comparison of best efficiencies achieved in lab based photovoltaic devices. Adapted from[8]. DSCs in bold red, perovskites bold pink. 115

Bibliography

[1] US energy information Administration. International Energy Statistics https://www.eia.gov/cfapps/ipdbproject/iedindex3.cfm.

[2] The International Energy Agency IEA. *Key World Energy Statistics 2015*. Key World Energy Statistics. OECD Publishing, oct 2015.

[3] Survation on behalf of The Mail On Sunday. http://survation.com/wp-content/uploads/2014/04/MailEnergyFinal.pdf. Energy Poll, 2013.

[4] REN 21 Steering Committee. Renewables 2013 GLOBAL STATUS REPORT. Technical report, REN21, 2013.

[5] BP. BP Statistical Review of World Energy June 2013. http://www.bp.com/content/dam/bp/pdf/statistical-review/statistical_review_of_world_energy_2013.pdf. Technical Report June, BP, 2013.

[6] Christian a. Gueymard. The sun's total and spectral irradiance for solar energy applications and solar radiation models. *Solar Energy*, 76(4):423–453, apr 2004.

[7] William W.S. Charters. Solar energy: Current status and future prospects. *Energy Policy*, 19(8):738–741, oct 1991.

[8] G. Wilson and D. Mooney. http://www.nrel.gov/ncpv/images/efficiency_chart.jpg, 2016.

[9] M. C. Scharber and N. S. Sariciftci. Efficiency of bulk-heterojunction organic solar cells. *Progress in Polymer Science*, 38(12):1929–1940, 2013.

[10] M O'Regan, B, Gratzel. A low-cost, high-efficiency solar cell based on dye-sensitized colloidal TiO2 films. *nature*, 353:737–740, 1991.

[11] The ECO experts. Which Solar Panels Are Most Efficient http://www.theecoexperts.co.uk/which-solar-panels-are-most-efficient.

[12] A Stierle. Surface core level shift observed on NiAl(110). *Surface Science*, 529(3):L263–L268, apr 2003.

[13] Aswani Yella, Hsuan-Wei Lee, Hoi Nok Tsao, Chenyi Yi, Aravind Kumar Chandiran, Md Khaja Nazeeruddin, Eric Wei-Guang Diau, Chen-Yu Yeh, Shaik M Zakeeruddin, and Michael Grätzel. Porphyrin-sensitized solar cells with cobalt (II/III)-based redox electrolyte exceed 12 percent efficiency. *Science (New York, N.Y.)*, 334(6056):629–34, nov 2011.

[14] Simon Mathew, Aswani Yella, Peng Gao, Robin Humphry-Baker, Basile F. E. Curchod, Negar Ashari-Astani, Ivano Tavernelli, Ursula Rothlisberger, Md. Khaja Nazeeruddin, and Michael Grätzel. Dye-sensitized solar cells with 13% efficiency achieved through the molecular engineering of porphyrin sensitizers. *Nature Chemistry*, 6(3):242–247, 2014.

[15] Tae Eui Kang, Han-Hee Cho, Chul-Hee Cho, Ki-Hyun Kim, Hyunbum Kang, Myounghee Lee, Sunae Lee, Bongsoo Kim, Chan Im, and Bumjoon J Kim. Photoinduced charge transfer in donor-acceptor (DA) copolymer: fullerene bis-adduct polymer solar cells. *ACS applied materials & interfaces*, 5(3):861–8, feb 2013.

[16] Tohru Shiga and Tomoyoshi Motohiro. Photosensitization of nanoporous TiO2 film with porphyrin-linked fullerene. *Thin Solid Films*, 516(6):1204–1208, 2008.

[17] J Ben Taylor, Louise C Mayor, Janine C Swarbrick, James N O'Shea, Cristina Isvoranu, and Joachim Schnadt. Adsorption and charge transfer dynamics of bi-isonicotinic acid on Au(111). *The Journal of chemical physics*, 127(13):134707, oct 2007.

[18] Andrew J Britton, Anna Rienzo, James N O'Shea, and Karina Schulte. Charge transfer between the Au(111) surface and adsorbed C(60): Resonant photoemission and new core-hole decay channels. *The Journal of chemical physics*, 133(9):094705, sep 2010.

[19] P Willmott. *An Introduction to Synchrotron Radiation Techniques and Applications*. Wiley, 2011.

[20] R. Nyholm and J.N. Andersen. Beamline I311 at MAX-LAB: a VUV/soft X-ray undulator beamline for high resolution electron spectroscopy. *Nuclear Instruments and Methods in Physics Research Section A*, 467-468:520–524, jul 2001.

[21] James N O'Shea, John B Taylor, Janine C Swarbrick, Graziano Magnano, Louise C Mayor, and Karina Schulte. Electrospray deposition of carbon nanotubes in vacuum. *Nanotechnology*, 18(3):035707, jan 2007.

[22] Louise C Mayor, J Ben Taylor, Graziano Magnano, Anna Rienzo, Christopher J Satterley, James N O'Shea, and Joachim Schnadt. Photoemission, resonant photoemission, and x-ray absorption of a Ru(II) complex adsorbed on rutile TiO2(110) prepared by in situ electrospray deposition. *The Journal of chemical physics*, 129(11):114701, sep 2008.

[23] Louise C Mayor, Alex Saywell, Graziano Magnano, Christopher J Satterley, Joachim Schnadt, and James N O'Shea. Adsorption of a Ru(II) dye complex on the Au(111) surface: photoemission and scanning tunneling microscopy. *The Journal of chemical physics*, 130(16):164704, apr 2009.

[24] H. Hertz. Ueber einen Einfluss des ultravioletten Lichtes auf die electrische Entladung [On an effect of ultra-violet light upon the electrical discharge]. *Annalen der Physik und Chemie*, 267(8):983–1000, 1887.

[25] Joachim Stohr. *NEXAFS Spectroscopy*. Springer, 1996.

[26] PA Brühwiler, O Karis, and N Mårtensson. Charge-transfer dynamics studied using resonant core spectroscopies. *Reviews of Modern Physics*, 74(July):703–740, jul 2002.

[27] U Gelius, PF Heden, and J Hedman. Molecular Spectroscopy by Means of ESCA III. Carbon compounds. *Physica scripta*, 2:70–80, 1970.

[28] DA Shirley. High-Resolution X-Ray Photoemission Spectrum of the Valence Bands of Gold. *Physical Review B*, 5(12):4709–4714, jun 1972.

[29] J. Schnadt, J. O'Shea, L. Patthey, J. Krempaský, N. Mårtensson, and P. Brühwiler. Alignment of valence photoemission, x-ray absorption, and substrate density of states for an adsorbate on a semiconductor surface. *Physical Review B*, 67(23):235420, jun 2003.

[30] Joachim Schnadt, Paul A Brühwiler, Luc Patthey, James N O'Shea, Sven Södergren, Michael Odelius, Rajeev Ahuja, Olof Karis, Margit Bässler, Petter Persson, Hans Siegbahn, S Lunell, and Nils Mårtensson. Experimental evidence for sub-3-fs charge transfer from an aromatic adsorbate to a semiconductor. *Nature*, 418(6898):620–3, aug 2002.

[31] A. F. Carley and M. W. Roberts. An X-Ray Photoelectron Spectroscopic Study of the Interaction of Oxygen and Nitric Oxide with Aluminium. *Proceedings of the Royal Society A: Mathematical, Physical and Engineering Sciences*, 363(1714):403–424, nov 1978.

[32] S. Tanuma, C. J. Powell, and D. R. Penn. Calculation of electron inelastic mean free paths (IMFPs) VII. Reliability of the TPP-2M IMFP predictive equation. *Surface and Interface Analysis*, 35(3):268–275, mar 2003.

[33] M.A. Green. Recent developments in photovoltaics. *Solar Energy*, 76:3–8, jan 2004.

[34] T.M. Razykov, C.S. Ferekides, D. Morel, E. Stefanakos, H.S. Ullal, and H.M. Upadhyaya. Solar photovoltaic electricity: Current status and future prospects. *Solar Energy*, 85(8):1580–1608, aug 2011.

[35] G. Dingemans and W. M. M. Kessels. Status and prospects of Al2O3-based surface passivation schemes for silicon solar cells. *Jour-*

nal of Vacuum Science & Technology A: Vacuum, Surfaces, and Films, 30(4):040802, jul 2012.

[36] Alexander R. Pascoe, Laure Bourgeois, Noel W. Duffy, Wanchun Xiang, and Yi-Bing Cheng. Surface State Recombination and Passivation in Nanocrystalline TiO 2 Dye-Sensitized Solar Cells. *The Journal of Physical Chemistry C*, 117(47):25118–25126, nov 2013.

[37] Jae-Yup Kim, Soon Hyung Kang, Hyun Sik Kim, and Yung-Eun Sung. Preparation of highly ordered mesoporous Al2O3/TiO2 and its application in dye-sensitized solar cells. *Langmuir : the ACS journal of surfaces and colloids*, 26(4):2864–2870, feb 2010.

[38] Katherine E Roelofs, Thomas P Brennan, Juan C Dominguez, Colin D Bailie, George Y Margulis, Eric T Hoke, Michael D Mcgehee, and Stacey F Bent. Effect of Al2O3 Recombination Barrier Layers Deposited by Atomic Layer Deposition in Solid-State CdS Quantum Dot-Sensitized Solar Cells. *The Journal of Physical Chemistry C*, 117:5584–5592, 2013.

[39] Chin Yong Neo and Jianyong Ouyang. Precise modification of the interface between titanium dioxide and electrolyte of dye-sensitized solar cells with oxides deposited by thermal evaporation of metals and subsequent oxidation. *Journal of Power Sources*, 196(23):10538–10542, dec 2011.

[40] Ville Makinen, Karoliina Honkala, and Hannu Hakkinen. Atomic Layer Deposition of Aluminum Oxide on TiO 2 and Its Impact on N3 Dye Adsorption from First Principles. *The Journal of Physical Chemistry C*, 115(18):9250–9259, may 2011.

[41] Michael Grätzel. Conversion of sunlight to electric power by nanocrystalline dye-sensitized solar cells. *Journal of Photochemistry and Photobiology A: Chemistry*, 164(1-3):3–14, jun 2004.

[42] Ulrike Diebold, Shao-Chun Li, and Michael Schmid. Oxide surface science. *Annual review of physical chemistry*, 61:129–148, jan 2010.

[43] J. Trost, H. Brune, J. Wintterlin, R. J. Behm, and G. Ertl. Interaction of oxygen with Al(111) at elevated temperatures. *The Journal of Chemical Physics*, 108(4):1740, jan 1998.

[44] Georg Kresse, Michael Schmid, Evelyn Napetschnig, Maxim Shishkin, Lukas Köhler, and Peter Varga. Structure of the ultrathin aluminum oxide film on NiAl(110). *Science (New York, N.Y.)*, 308(5727):1440–1442, jun 2005.

[45] N. M. Martin, J. Knudsen, S. Blomberg, J. Gustafson, J. N. Andersen, E. Lundgren, H. Härelind Ingelsten, P.-a. Carlsson, M. Skoglundh, A. Stierle, and G. Kresse. High-resolution core-level spectroscopy study of the ultrathin aluminum oxide film on NiAl(110). *Physical Review B*, 83(12):125417, mar 2011.

[46] S Andersson, PA Brühwiler, and A Sandell. Metaloxide interaction for metal clusters on a metal-supported thin alumina film. *Surface science*, 442, aug 1999.

[47] Andrew J Britton, Matthew Weston, J Ben Taylor, Anna Rienzo, Louise C Mayor, and James N O'Shea. Charge transfer interactions of a Ru(II) dye complex and related ligand molecules adsorbed on Au(111). *The Journal of chemical physics*, 135(16):164702, oct 2011.

[48] Matthew Weston, Andrew J Britton, and James N O'Shea. Charge transfer dynamics of model charge transfer centers of a multicenter water splitting dye complex on rutile TiO2(110). *The Journal of chemical physics*, 134(5):054705, feb 2011.

[49] J.B. Taylor, L.C. Mayor, J.C. Swarbrick, J.N. O'Shea, and J. Schnadt. Charge-Transfer Dynamics at Model Metal-Organic Solar Cell Surfaces. *Journal of Physical Chemistry C*, 111(44):16646–16655, nov 2007.

[50] RM Jaeger, H Kuhlenbeck, and HJ Freund. Formation of a well-ordered aluminium oxide overlayer by oxidation of NiAl(110). *Surface science*, 259:235–252, jul 1991.

[51] L. Heinke, L. Lichtenstein, G. H. Simon, T. König, M. Heyde, and H.-J. Freund. Structure and electronic properties of step edges in the aluminum oxide film on NiAl(110). *Physical Review B*, 82(7):075430, aug 2010.

[52] M. Schmid, M. Shishkin, G. Kresse, E. Napetschnig, P. Varga, M. Kulawik, N. Nilius, H.-P. Rust, and H.-J. Freund. Oxygen-Deficient Line Defects in an Ultrathin Aluminum Oxide Film. *Physical Review Letters*, 97(4):046101, jul 2006.

[53] Christopher S Kley, Christian Dette, Gordon Rinke, Christopher E Patrick, Jan Cechal, Soon Jung Jung, Markus Baur, Michael Dürr, Stephan Rauschenbach, Feliciano Giustino, Sebastian Stepanow, and Klaus Kern. Atomic-scale observation of multiconformational binding and energy level alignment of ruthenium-based photosensitizers on TiO2 anatase. *Nano letters*, 14(2):563–569, feb 2014.

[54] JF Kielkopf. New approximation to the Voigt function with applications to spectral-line profile analysis. *JOSA*, 63(8):987–995, aug 1973.

[55] Lars Ojamäe, Christian Aulin, Henrik Pedersen, and Per-Olov Käll. IR and quantum-chemical studies of carboxylic acid and glycine adsorption on rutile TiO2 nanoparticles. *Journal of colloid and interface science*, 296(1):71–78, apr 2006.

[56] J. Schnadt, J. Schiessling, and P.a. Brühwiler. Comparison of the size of excitonic effects in molecular π systems as measured by core and valence spectroscopies. *Chemical Physics*, 312(1-3):39–45, jun 2005.

[57] B Kempgens, A Kivimäki, M Neeb, H M Köppe, A M Bradshaw, and J Feldhaus. A high-resolution N 1s photoionization study of the molecule in the near-threshold region. *Journal of Physics B: Atomic, Molecular and Optical Physics*, 29(22):5389–5402, nov 1996.

[58] Ching Lin, Feng-Yu Tsai, Min-Hsueh Lee, Chia-Hua Lee, Ta-Chang Tien, Lih-Ping Wang, and Song-Yeu Tsai. Enhanced performance of dye-sensitized solar cells by an Al2O3 charge-recombination barrier formed

by low-temperature atomic layer deposition. *Journal of Materials Chemistry*, 19(19):2999, 2009.

[59] Thomas W Hamann, Omar K Farha, and Joseph T Hupp. Outer-Sphere Redox Couples as Shuttles in Dye-Sensitized Solar Cells . Performance Enhancement Based on Photoelectrode Modification via Atomic Layer Deposition Outer-Sphere Redox Couples as Shuttles in Dye-Sensitized Solar Cells . Performance Enhancement. pages 19756–19764, 2008.

[60] V. Ganapathy, B. Karunagaran, and Shi-Woo Rhee. Improved performance of dye-sensitized solar cells with TiO2/alumina coreshell formation using atomic layer deposition. *Journal of Power Sources*, 195(15):5138–5143, 2010.

[61] S J Han Wu HW Tai, QD Zhang, J Xu, S Zhou, CH Yang, Y Hu, H Chen, BL Zhao, XZ. Improvement in dye-sensitized solar cells employing TiO2 electrodes coated with Al2O3 by reactive direct current magnetron sputtering. *Journal of Power Sources*, 182(1):123, 2008.

[62] Liisa J. Antila, Mikko J. Heikkila, Viivi Aumanen, Marianna Kemell, Pasi Myllyperkio, Markku Leskela, and Jouko E. I. Korppi-Tommola. Suppression of Forward Electron Injection from Ru(dcbpy) 2 (NCS) 2 to Nanocrystalline TiO 2 Film As a Result of an Interfacial Al 2 O 3 Barrier Layer Prepared with Atomic Layer Deposition. *The Journal of Physical Chemistry Letters*, 1(2):536–539, jan 2010.

[63] Jianchang Guo, Chunxing She, and Tianquan Lian. Effect of insulating oxide overlayers on electron injection dynamics in dye-sensitized nanocrystalline thin films. *The Journal of Physical Chemistry C*, 111:8979–8987, 2007.

[64] Riikka L. Puurunen. Surface chemistry of atomic layer deposition: A case study for the trimethylaluminum/water process. *Journal of Applied Physics*, 97(12):121301, 2005.

[65] Steven M George. Atomic layer deposition: an overview. *Chemical reviews*, 110(1):111–31, jan 2010.

[66] Thomas P Brennan, Jonathan R Bakke, I-Kang Ding, Brian E Hardin, William H Nguyen, Rajib Mondal, Colin D Bailie, George Y Margulis, Eric T Hoke, Alan Sellinger, Michael D McGehee, and Stacey F Bent. The importance of dye chemistry and TiCl4 surface treatment in the behavior of Al2O3 recombination barrier layers deposited by atomic layer deposition in solid-state dye-sensitized solar cells. *Physical chemistry chemical physics : PCCP*, 14(35):12130–40, sep 2012.

[67] Xianfeng Gao, Dongsheng Guan, Jingwan Huo, Junhong Chen, and Chris Yuan. Free standing TiO2 nanotube array electrodes with an ultra-thin Al2O3 barrier layer and TiCl4 surface modification for highly efficient dye sensitized solar cells. *Nanoscale*, 5(21):10438, 2013.

[68] Ta-Chang Tien, Fu-Ming Pan, Lih-Ping Wang, Chia-Hua Lee, Yung-Liang Tung, Song-Yeu Tsai, Ching Lin, Feng-Yu Tsai, and Su-Jen Chen. Interfacial energy levels and related properties of atomic-layer-deposited Al2O3 films on nanoporous TiO2 electrodes of dye-sensitized solar cells. *Nanotechnology*, 20(30):305201, jul 2009.

[69] Lj Antila and Mj Heikkila. ALD grown aluminum oxide submonolayers in dye-sensitized solar cells: the effect on interfacial electron transfer and performance. *The Journal of ...*, pages 16720–16729, 2011.

[70] Andrew J Gibson, Robert H Temperton, Karsten Handrup, Matthew Weston, Louise C Mayor, and James N O'Shea. Charge transfer from an adsorbed ruthenium-based photosensitizer through an ultra-thin aluminium oxide layer and into a metallic substrate. *The Journal of chemical physics*, 140(23):234708, jun 2014.

[71] James N. O'Shea, J. Ben Taylor, Louise C. Mayor, Janine C. Swarbrick, and Joachim Schnadt. Molecular damage in bi-isonicotinic acid adsorbed on rutile TiO2(110). *Surface Science*, 602(9):1693–1698, may 2008.

[72] Charlotte Mayor. *The Adsorption and Charge-Transfer Dynamics of Model Dye-Sensitised Solar Cell Surfaces*. PhD thesis, University of Nottingham, 2009.

[73] A. C. Dillon, A. W. Ott, J. D. Way, and S. M. George. Surface chemistry of Al2O3 deposition using Al(CH3)3 and H2O in a binary reaction sequence. *Surface Science*, 322(1-3):230–242, 1995.

[74] A.W. Ott, J.W. Klaus, J.M. Johnson, and S.M. George. Al3O3 thin film growth on Si(100) using binary reaction sequence chemistry. *Thin Solid Films*, 292(1-2):135–144, 1997.

[75] Hiroshi Kumagai, Masahiko Matsumoto, Yoshiyuki Kawamura, Koichi Toyoda, and Minoru Obara. Fabrication of Multilayers with Growth Controlled by Sequential Surface Chemical Reactions. *Japanese Journal of Applied Physics*, 33(Part 1, No. 12B):7086–7089, dec 1994.

[76] Taewook Nam, Jae-Min Kim, Min-Kyu Kim, Hyungjun Kim, and Woo-Hee Kim. Low-temperature Atomic Layer Deposition of TiO_2, Al_2O_3, and ZnO Thin Films. *Journal of the Korean Physical Society*, 59(21):452, 2011.

[77] M. D. Groner, F. H. Fabreguette, J. W. Elam, and S. M. George. Low-Temperature Al2O3 Atomic Layer Deposition. *Chemistry of Materials*, 16(4):639–645, 2004.

[78] Ronald Kuse, Manisha Kundu, Tetsuji Yasuda, Noriyuki Miyata, and Akira Toriumi. Effect of precursor concentration in atomic layer deposition of Al[sub 2]O[sub 3]. *Journal of Applied Physics*, 94(10):6411, 2003.

[79] Raija Matero, Antti Rahtu, Mikko Ritala, Markku Leskelä, and Timo Sajavaara. Effect of water dose on the atomic layer deposition rate of oxide thin films. *Thin Solid Films*, 368(1):1–7, jun 2000.

[80] J Schnadt, J Schiessling, J.N O'Shea, S.M Gray, L Patthey, M.K.-J Johansson, M Shi, J Krempaský, J Åhlund, P.G Karlsson, P Persson, N Mårtensson, and P.a Brühwiler. Structural study of adsorption of isonicotinic acid and related molecules on rutile TiO2(110) I: XAS and STM. *Surface Science*, 540(1):39–54, aug 2003.

[81] J Biener, M Bäumer, Jiong Wang, and RJ Madix. Electronic structure and growth of vanadium on TiO2(110). *Surface science*, 450:12–26, 2000.

[82] Tanvi Vats, Shailesh N. Sharma, Mahesh Kumar, M. Kar, Kiran Jain, V.N. Singh, B.R. Mehta, and a.K. Narula. Comparison of photostability, optical and structural properties of TiO2/conjugated polymer hybrid composites prepared via different methods. *Thin Solid Films*, 519(3):1100–1105, nov 2010.

[83] C. J. Powell and A. Jablonski. Evaluation of electron inelastic mean free paths for selected elements and compounds. *Surface and Interface Analysis*, 29(August 1999):108–114, 2000.

[84] Jörg Haeberle, Karsten Henkel, Hassan Gargouri, Franziska Naumann, Bernd Gruska, Michael Arens, Massimo Tallarida, and Dieter Schmeißer. Ellipsometry and XPS comparative studies of thermal and plasma enhanced atomic layer deposited Al 2 O 3 -films. *Beilstein Journal of Nanotechnology*, 4(1):732–742, nov 2013.

[85] Anders Strålin and Thomas Hjertberg. Influence of surface composition on initial hydration of aluminium in boiling water. *Applied Surface Science*, 74(3):263–275, mar 1994.

[86] J Riga Gobillon, C Tenret-Noël, J J Pireaux, R Caudano, J J Verbist, and Y. Electronic Structure of Rutile Oxides TiO 2 , RuO 2 and IrO 2 Studied by X-ray Photoelectron Spectroscopy. *Physica Scripta*, 16(5-6):351, 1977.

[87] J F Moulder and J Chastain. *Handbook of X-ray Photoelectron Spectroscopy: A Reference Book of Standard Spectra for Identification and Interpretation of XPS Data*. Physical Electronics Division, Perkin-Elmer Corporation, 1992.

[88] Marc De Graef. *Advances in Surface Science*. Academic Press.

[89] Mark J. Jackman, Andrew G. Thomas, and Chris Muryn. Photoelectron spectroscopy study of stoichiometric and reduced anatase

TiO<inf>2</inf>(101) surfaces: The effect of subsurface defects on water adsorption at near-ambient pressures. *Journal of Physical Chemistry C*, 119(24):13682–13690, 2015.

[90] Rajesh Pandiyan, Nazar Delegan, Ahmad Dirany, Patrick Drogui, and My Ali El Khakani. Probing the Electronic Surface Properties and Bandgap Narrowing of in situ N, W, and (W,N) Doped Magnetron-Sputtered TiO2 Films Intended for Electro-Photocatalytic Applications. *Journal of Physical Chemistry C*, 120(1):631–638, 2016.

[91] C. Soto, R. Wu, D. W. Bennett, and W. T. Tysoe. Infrared Spectroscopy of Trimethylaluminum and Dimethylaluminum chloride adsorbed on Alumina. *Chemistry of Materials*, 6(21):1705–1711, 1994.

[92] L. Patthey, H. Rensmo, P. Persson, K. Westermark, L. Vayssieres, A. Stashans, A. Petersson, P. A. Bruhwiler, H. Siegbahn, S. Lunell, and N. Martensson. Adsorption of bi-isonicotinic acid on rutile TiO[sub 2](110). *The Journal of Chemical Physics*, 110(12):5913, 1999.

[93] Petter Persson, Sten Lunell, Paul a. Bruhwiler, Joachim Schnadt, Sven Sodergren, James N. O'Shea, Olof Karis, Hans Siegbahn, Nils Martensson, Margit Bassler, and Luc Patthey. N 1s x-ray absorption study of the bonding interaction of bi-isonicotinic acid adsorbed on rutile TiO[sub 2](110). *The Journal of Chemical Physics*, 112(9):3945, 2000.

[94] D O Scanlon, C W Dunnill, J Buckeridge, S A Shevlin, A J Logsdail, S M Woodley, C R A Catlow, M J Powell, R G Palgrave, I P Parkin, G W Watson, T W Keal, P Sherwood, A Walsh, and A A Sokol. Band alignment of rutile and anatase TiO2. *Nature Materials*, 12(9):798–801, 2013.

[95] Christophe Nicolas and Catalin Miron. Lifetime broadening of core-excited and -ionized states. *Journal of Electron Spectroscopy and Related Phenomena*, 185(8-9):267–272, sep 2012.

[96] Andrew Britton, Matthew Weston, and James O'Shea. Charge Transfer from an Aromatic Adsorbate to a Semiconductor TiO_{2} Surface

Probed on the Femtosecond Time Scale with Resonant Inelastic X-Ray Scattering. *Physical Review Letters*, 109(1):017401, jul 2012.

[97] Hiroshi Imahori, Makoto Kimura, Kohei Hosomizu, and Shunichi Fukuzumi. Porphyrin and fullerene-based photovoltaic devices. *Journal of Photochemistry and Photobiology A: Chemistry*, 166(1-3):57–62, aug 2004.

[98] Christoph J Brabec, Srinivas Gowrisanker, Jonathan J M Halls, Darin Laird, Shijun Jia, and Shawn P Williams. Polymer-fullerene bulk-heterojunction solar cells. *Advanced materials (Deerfield Beach, Fla.)*, 22(34):3839–56, sep 2010.

[99] Nadia Camaioni and Riccardo Po. Pushing the Envelope of the Intrinsic Limitation of Organic Solar Cells. *The Journal of Physical Chemistry Letters*, 4(11):1821–1828, jun 2013.

[100] Olgun Adak, Gregor Kladnik, Gregor Bavde, Albano Cossaro, Alberto Morgante, Dean Cvetko and Latha Venkataraman. Ultrafast Bidirectional Charge Transport and Electron Decoherence at Molecule/Surface Interfaces: A Comparison of Gold, Graphene, and Graphene Nanoribbon Surfaces. *Nano letters*, 15(12):8316–8321, 2015.

[101] BW Hoogenboom, R Hesper, LH Tjeng, and GA Sawatzky. Charge transfer and doping-dependent hybridization of C_ {60} on noble metals. *Physical Review B*, 57(19):939–942, 1998.

[102] L.H Tjeng, R Hesper, A.C.L Heessels, A Heeres, H.T Jonkman, and G.A Sawatzky. Development of the electronic structure in a K-doped C60 monolayer on a Ag(111) surface. *Solid State Communications*, 103(1):31–35, jul 1997.

[103] Hong-Nian Li, Xiao-Xiong Wang, Shao-Long He, Kurash Ibrahim, Hai-Jie Qian, Run Su, Jun Zhong, M.I. Abbas, and Cai-Hao Hong. Electronic state of C60 monolayer on Ag(111) before and after Yb intercalation. *Surface Science*, 586(1-3):65–73, jul 2005.

[104] Nathan Swami, Hong He, and Bruce E Koel. Polymerization and decomposition of C 60 on Pt(111) surfaces. *Physical Review B*, 59(12):8283–8291, 1999.

[105] KD Tsuei, JY Yuh, CT Tzeng, and RY Chu. Photoemission and photoabsorption study of C 60 adsorption on Cu (111) surfaces. *Physical Review B*, 56(23):412–420, 1997.

[106] Woei Wu Pai, H. T. Jeng, C.-M. Cheng, C.-H. Lin, Xudong Xiao, Aidi Zhao, Xieqiu Zhang, Geng Xu, X. Q. Shi, M. a. Van Hove, C.-S. Hsue, and K.-D. Tsuei. Optimal Electron Doping of a C_{60} Monolayer on Cu(111) via Interface Reconstruction. *Physical Review Letters*, 104(3):036103, jan 2010.

[107] CT Tzeng, WS Lo, JY Yuh, RY Chu, and KD Tsuei. Photoemission, near-edge x-ray-absorption spectroscopy, and low-energy electron-diffraction study of C60 on Au(111) surface. *Physical Review B*, 61(3):2263–2272, 2000.

[108] Tomihiro Hashizume, K Motai, X. Wang, H Shinohara, Y Saito, Y Maruyama, K. Ohno, Y. Kawazoe, Y Nishina, H. Pickering, Y Kuk, and T Sakurai. Intramolecular structures of C60 molecules adsorbed on the Cu(111)-(11) surface. *Physical Review Letters*, 71(18):2959–2962, nov 1993.

[109] T. Ohno, Y. Chen, S. Harvey, G. Kroll, J. Weaver, R. Haufler, and R. Smalley. C60 bonding and energy-level alignment on metal and semiconductor surfaces. *Physical Review B*, 44(24):13747–13755, dec 1991.

[110] A. Maxwell, P. Brühwiler, A. Nilsson, N. Mårtensson, and P Rudolf. Photoemission, autoionization, and x-ray-absorption spectroscopy of ultrathin-film C60 on Au(110). *Physical Review B*, 49(15):10717–10725, apr 1994.

[111] Christopher J Satterley, Luís M a Perdigão, Alex Saywell, Graziano Magnano, Anna Rienzo, Louise C Mayor, Vinod R Dhanak, Peter H Beton,

and James N O'Shea. Electrospray deposition of fullerenes in ultra-high vacuum: in situ scanning tunneling microscopy and photoemission spectroscopy. *Nanotechnology*, 18(45):455304, nov 2007.

[112] J. J. Yeh. *Atomic Calculation of Photoionization Cross-Sections and Asymmetry Parameters*. Routledge, 1993.

[113] J J Yeh and I Lindau. Atomic subshell photoionization cross sections and asymmetry parameters: $1 < Z < 103$. *Atomic Data and Nuclear Data Tables*, 32(1):1–155, 1985.

[114] Matthew Weston, Thomas J Reade, Andrew J Britton, Karsten Handrup, Neil R Champness, and James N O'Shea. A single centre water splitting dye complex adsorbed on rutile TiO2(110): photoemission, x-ray absorption, and optical spectroscopy. *The Journal of chemical physics*, 135(11):114703, oct 2011.

[115] Joseph Lanzafame, Dwayne Miller, Muenter Annabel, and Bruce A. Parkinson. Ultrafast charge transfer dynamics at tin disulfide surfaces. *Chemical Physics*, 92:2820, 1992.

[116] J. M. Lanzafame, S. Palese, D. Wang, R. J. D. Miller, and a. a. Muenter. Ultrafast Nonlinear Optical Studies of Surface Reaction Dynamics: Mapping the Electron Trajectory. *The Journal of Physical Chemistry*, 98(43):11020–11033, oct 1994.

[117] R. C. Haddon, L. E. Brus, and Krishnan Raghavachari. Electronic structure and bonding in icosahedral C60. *Chemical Physics Letters*, 125(5-6):459–464, apr 1986.

[118] Hong He, Nathan Swami, and BE Koel. Control of the growth of ordered C 60 films by chemical modification of Pt (111) surfaces. *Thin Solid Films*, 348:30–37, 1999.

[119] A Pivrikas and NS Sariciftci. A Review of Charge Transport and Recombination in Polymer/Fullerene Organic Solar Cells. *Progress in ...*, 15:677–696, 2007.

[120] Michael M Lee, Joël Teuscher, Tsutomu Miyasaka, Takurou N Murakami, and Henry J Snaith. Efficient hybrid solar cells based on meso-superstructured organometal halide perovskites. *Science (New York, N.Y.)*, 338(6107):643–7, nov 2012.